Reviews of Geophysics

AMERICAN GEOPHYSICAL UNION

VOLUME 33 NUMBER 1 FEBRUARY 1995

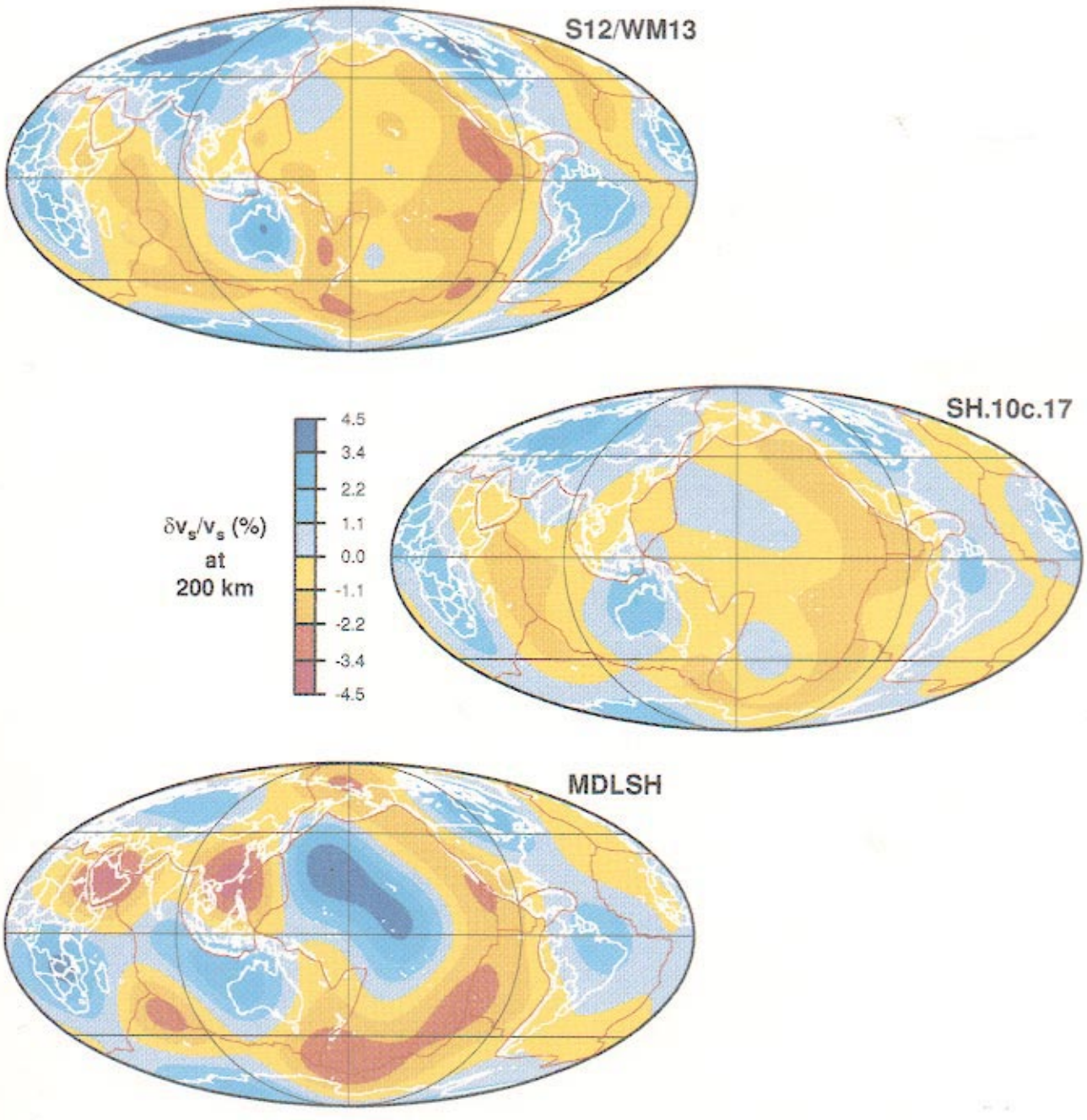

Reviews of Geophysics VOLUME 33 NUMBER 1 FEBRUARY 1995
REGEEP

THE COVER PHOTOGRAPH

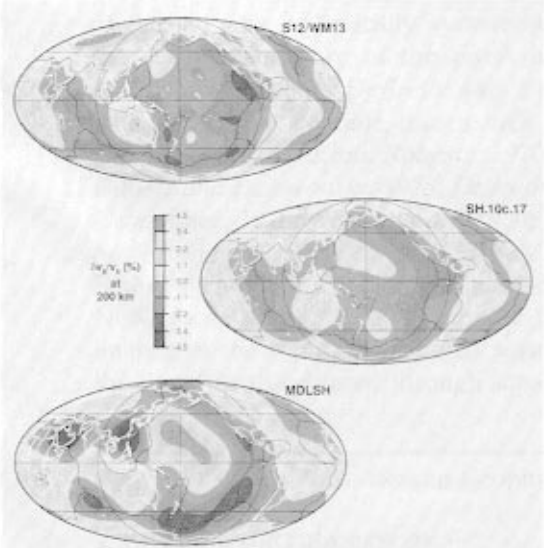

Long-wavelength relative seismic shear velocity variations are shown at a depth of 200 km beneath the Earth's surface from three mantle models (S12/Wm13 of Su et. al., 1993; SH.10c.17 of Masters et al., 1992; MDLSH of Tanimoto, 1990a). The amplitudes of the shear velocity variations are represented as a percentage of the spherical component of shear velocity taken from the model PREM (Dziewonski and Anderson, 1981). Lateral shear velocity variations at this depth in these models are highly correlated with known tectonic features, such as stable continental regions, orogenic belts, oceanic ridges, and old oceanic basins. However, discrepancies among the amplitudes of the variations and the details of the models are apparent in this generation of models.

THREE-DIMENSIONAL SEISMIC MODELS OF THE EARTH'S MANTLE

Michael H. Ritzwoller and Eugene M. Lavely
Department of Physics and Cooperative Institute for Research in the Environmental Sciences
University of Colorado, Boulder

Abstract. Accurate models of the distribution of elastic heterogeneity in the Earth's mantle are important in many areas of geophysics. The purpose of this paper is to characterize and compare quantitatively a set of recent three-dimensional models of the elastic structure of the Earth, to assess their similarities and differences, and to analyze their fit to one class of data in order to highlight fruitful directions for future research. The aspherical models considered are the following: M84C (Woodhouse and Dziewonski, 1984), LO2.56 (Dziewonski, 1984), MDLSH (Tanimoto, 1990a), SH.10c.17 (Masters et al., 1992), and S12_WM13 (Su et al., 1994). Through much of the discussion, M84C and LO2.56 are combined into a single whole mantle model, M84C + LO2.56. The fit of each model to previously tabulated even degree normal mode structure coefficients taken from Smith and Masters (1989a) and Ritzwoller et al. (1988) for multiplets along the normal mode fundamental and first, second, and fifth overtone branches is also presented. Rather than concentrating on detailed comparisons of specific features of the models, analyses of these models are general and statistical in nature. In particular, we focus on a comparison of the amplitude and the radial and geographical distribution of heterogeneity in each model and how variations in each affect the fit to the normal mode observations. In general, the results of the comparisons between the models are encouraging, especially with respect to the geographical distribution of heterogeneity and in the fit to the normal mode data sensitive to the upper mantle and lowermost lower mantle. There remain, however, significant discrepancies in amplitude and in the radial distribution of heterogeneity, especially near the top of the upper mantle and near the top of the lower mantle. The confident use of these models to constrain compositional and dynamical information about the mantle will await the resolution of these discrepancies. The factors that may be responsible for the differences in the models and/or for the misfit between the observed and predicted normal mode data are divided into two types: intrinsic (or procedural) and extrinsic (or structural). We discuss only three extrinsic factors at length here, including errors in the reference crustal models, unmodeled topography on discontinuities in the interior of the mantle, and errors in the assumed relationships between shear (v_s) and compressional (v_p) heterogeneity.

1. INTRODUCTION

A wide array of geophysical, geochemical, and astronomical studies depend on an accurate understanding of the magnitude and distribution of the elastic properties and density in the Earth's interior. Models of the average, spherically symmetric component of the seismic structure of the Earth have existed for more than 50 years [*Jeffreys and Bullen*, 1940] and with time have become increasingly accurate [e.g., *Herrin*, 1968; *Hales and Roberts*, 1970; *Randall*, 1971; *Gilbert and Dziewonski*, 1975; *Dziewonski et al.*, 1975; *Urhammer*, 1978; *Gogna et al.*, 1980; *Dziewonski and Anderson*, 1981; *Masters and Gilbert*, 1983; *Toy*, 1989; *Widmer et al.*, 1992; *Kennett and Engdahl*, 1993]. Now, more than a decade after the first global scale images of the three-dimensional seismic structure of the deep Earth emerged through separate analyses of body wave [*Dziewonski et al.*, 1977] and normal mode data [*Masters et al.*, 1982], it would seem appropriate to assess the nature, consistency, and fidelity of the new three-dimensional (3-D) seismic models to help guide future endeavors to improve the images of the Earth's deep interior.

1.1. Seismic Models and Their Importance

A seismic model is a portrait of the seismological structure of at least part of the Earth. To a seismologist, "structure" means information about the impact that a region would have on an elastic wave that might propagate through that region. Seismological models are not models of chemistry, nor are they dynamical, although chemical variations or strong convective fields would have an effect on seismological parameters. Rather, seismic models, as they currently exist, are static representations of seismic parameters and in

Reviews of Geophysics, 33, 1 / *February 1995*
pages 1–66
8755-1209/95/94RG-03020$15.00
Paper number 94RG03020

and of themselves do not address the cause or causes of the variations in the parameters that constitute the model. These issues are addressed by seismologists and other geophysicists after the model has been constructed.

Seismic parameters can be broken into two main categories: elastic and anelastic. By "elastic" it is meant that energy is not lost during passage of a seismic wave through a region. Consequently, "anelastic" models possess information about seismic attenuation, and elastic models do not. We will concentrate on recent elastic models. Such models themselves can be divided further into isotropic and anisotropic, and we will focus on the former class, or models whose defining characteristic is that the model parameters at a point are independent of the direction of travel of a wave. Elastic, isotropic models can be analyzed further into spherically symmetric and aspherical images of the Earth. The purpose of this paper is to compare and assess recently constructed, long-wavelength, aspherical, elastic, isotropic models of the Earth's mantle. This is a highly restrictive subclass of all possible seismic models, but it is one for which substantial progress has been achieved recently and is deserving of review. Such models can be represented by two parameters whose values change from place to place, usually either compressional (v_p) and shear (v_s) velocity or bulk (κ) and shear (μ) modulus.

Aspherical images of the Earth's internal structure are represented as perturbations to a reference model, which is usually ellipsoidal. Each of the three-dimensional seismological models considered here uses the spherical seismic preliminary reference Earth model (PREM) of *Dziewonski and Anderson* [1981] modified by an ellipticity correction as the reference to which all aspherical perturbations are added. The values in PREM of the seismic velocities and density across the mantle and crust are shown in Figure 1.

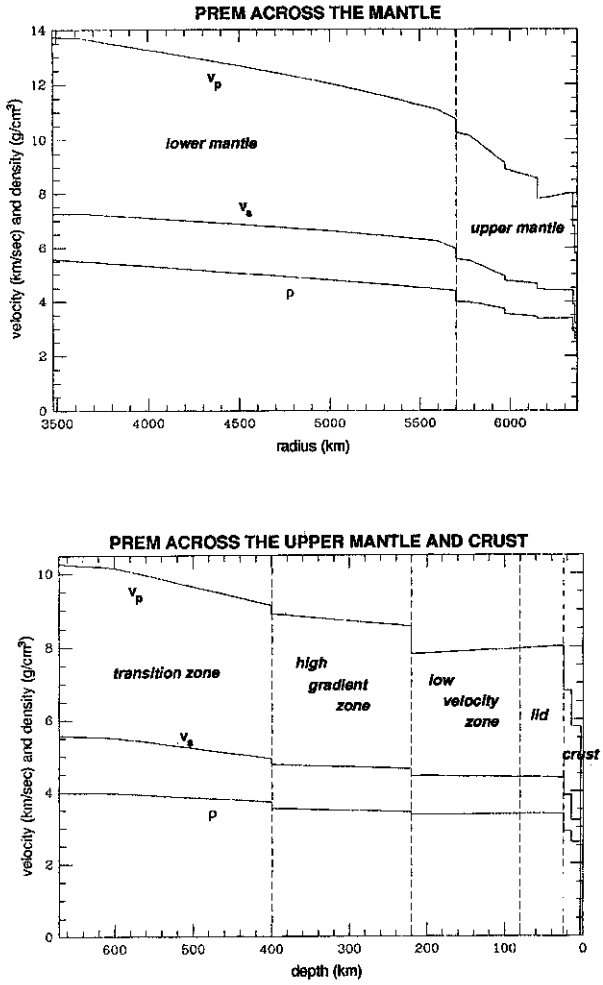

Figure 1. Elastic parameters and density within the crust and mantle, from the preliminary Earth reference model (PREM). (PREM is transversely isotropic between the Moho and the 220-km discontinuity. We plot the vertical component of v_s and v_p in this region.)

The mantle part of PREM is composed of eight spherical shells, extending from the core-mantle boundary (CMB) at a radius of approximately 3480 km to the base of the Earth's crust at a depth of 25 km. The boundary forming the base of the crust is called the Mohorovičić (Moho) discontinuity. These shells compose the lower mantle and upper mantle. The lower mantle is broken into three shells: D'' (3480- to 3630-km radius), the bulk of the lower mantle (3630- to 5600-km radius), and the uppermost lower mantle (5600- to 5701-km radius). The upper mantle is divided into five shells, the boundaries of which are usually referred to by their depth rather than by their radius. The 670-km and 400-km boundaries are separated by the Transition Zone, the high-gradient zone separates the 400-km from the 220-km boundaries, the low-velocity zone lies between the 220-km and 80-km boundaries, and the lid forms the volume between 80-km depth and the base of the crust. An extra boundary at 600 km is also included for mathematical reasons. The outermost 25 km of PREM comprises the crustal and oceanic models. The crustal part of PREM is broken into two shells: the Moho to the Conrad discontinuity (15-km depth) and the Conrad to the solid-ocean boundary (3-km depth). The region between the solid-ocean boundary and the free surface is filled with an oceanic model.

If a seismic model's properties jump discontinuously across a boundary, then the boundary is said to be a first-order discontinuity. If material properties only change slope at the boundary, then the discontinuity is said to be of second order. There are only three first-order discontinuities among the boundaries in the interior of the mantle: at 670-km, 400-km, and 220-km depth. The boundaries surrounding the mantle (CMB and Moho) are also first-order discontinuities. All first-order discontinuities on internal boundaries, like the Earth's free surface, can support topography. Therefore topographic undulations can exist on the

CMB, 670-km, 400-km, 220-km, and Moho boundaries.

Seismic models must be represented mathematically. An elliptical isotropic, elastic model, $m_0(r, \theta)$, such as PREM can be represented by a set of three functions of radius; either compressional velocity v_p, shear velocity v_s, and density ρ or bulk modulus κ, shear modulus μ, and density. A 3-D model possesses aspherical perturbations to this reference model. We refer to these perturbations as $\delta m(r, \theta, \phi)$, where r, θ, and ϕ stand for radius, colatitude, and longitude, respectively. The notation $\delta m(r, \theta, \phi)$ may represent $\delta v_s(r, \theta, \phi)$, $\delta v_p(r, \theta, \phi)$, $\delta\kappa(r, \theta, \phi)$, $\delta\mu(r, \theta, \phi)$, or $\delta\rho(r, \theta, \phi)$, or commonly may be the vector quantity comprising the triplets $(\delta v_s, \delta v_p, \delta\rho)$ or $(\delta\kappa, \delta\mu, \delta\rho)$. The full 3-D model is then $m(r, \theta, \phi) = m_0(r, \theta) + \delta m(r, \theta, \phi)$. In any event, the model $\delta m(r, \theta, \phi)$ is frequently generically called aspherical volumetric structure. Aspherical undulations or topography on internal boundaries and the free surface can also exist and are referred to as $h_d(\theta, \phi)$, where h has units of kilometers and the subscript d indicates a given boundary.

The global-scale 3-D seismic models considered here possess spherically symmetric attenuative or anelastic structures, and all aspherical perturbations are purely elastic and isotropic. Such volumetric structures, as well as topographic undulations on internal boundaries, can be represented in a number of ways. We reparameterize all models in terms of fully normalized complex spherical harmonics:

$$\delta m(r, \theta, \phi) = \sum_{s,t} \delta m_s^t(r) Y_s^t(\theta, \phi), \quad (1)$$

$$h_d(\theta, \phi) = \sum_{s,t} h_{ds}^t Y_s^t(\theta, \phi). \quad (2)$$

The spherical harmonic indices are referred to as the degree s and order t of aspherical structure.

Global 3-D seismic models are important for three main reasons: (1) they are concentrated summaries of huge volumes of seismic data, (2) they can be used to provide data corrections to constrain other types of structures and source parameters, and (3) they can be interpreted to provide information about the composition and dynamics of the Earth. In this latter regard, they hold promise for application in a large number of areas, ranging from applied to pure geophysics. On the applied end, 3-D Earth models are required for accurate earthquake location and source characterization. This is of relevance to earthquake hazard assessment and also to nuclear nonproliferation studies that require very accurate location and yield estimates of potential nuclear tests.

On the pure end of the scale, it has been the long-standing hope that with the construction and continuing development of models of the 3-D seismic structure of the deep Earth, information would be provided which would be crucial to an understanding of the Earth's global dynamics. For example, in a current geodynamical program of research, tomographic images are regularly converted to density anomalies and, together with excess density in the slabs, are entered as body forces into the equations of motion for buoyantly driven viscous flows. These flow fields are then used to predict certain surface observables, such as the geoid, plate motions, and surface topography [e.g., *Hager*, 1984; *Hager et al.*, 1985; *Hager and Clayton*, 1989; *Hager and Richards*, 1989; *Forte and Peltier*, 1991; *Dehant and Wahr*, 1991; *Forte et al.*, 1993]. The calibration of the convection models and the application of constraints on geodynamics are strongly dependent on the amplitude as well as the geographical distribution of heterogeneity in the input 3-D seismic models. *Olson et al.* [1990] recently described the state of the synthesis of 3-D seismic tomographic models with results from mantle geochemistry and mantle convection modeling, and *Montagner* [1994] discussed what has been learned about mantle convection from the seismic models.

Three-dimensional elastic seismic models are also beginning to see application in geodesy, geomagnetism, and the study of the Earth's rheology, and as a basis for the construction of global anelastic and anisotropic seismic models.

1.2. Seismic Data

The seismological waveform data used to construct the majority of the 3-D seismic models discussed here have come from several sources around the world. Figure 2 displays the approximate state of broadband digital seismic networks in early 1980 and late 1993. Over the last decade there has been a great improvement in global coverage, especially due to the opening up of China and the former Soviet Union to Western seismologists. It is safe to say that the full impact of the development of global digital seismic networks in these areas has not yet been felt.

Current digital seismic networks, which have been accumulating broadband seismic data openly available to seismic community, come under the umbrella of the Federation of Digital Seismographic Networks (FDSN), of which the U.S. representatives are the Incorporated Research Institutions for Seismology (IRIS) and the U.S. Geological Survey (USGS). The data that have historically received the greatest use in the construction of the 3-D seismic models discussed here are the Global Digital Seismographic Network (GDSN) data (operated by the USGS) and the International Deployment of Accelerometer (IDA) data (operated by the University of California, San Diego (UCSD)). These networks have been updated and largely subsumed under the IRIS Global Seismographic Network (GSN). The quantity and quality of globally recorded broadband data are growing rapidly, and waveform data are now readily available to FDSN

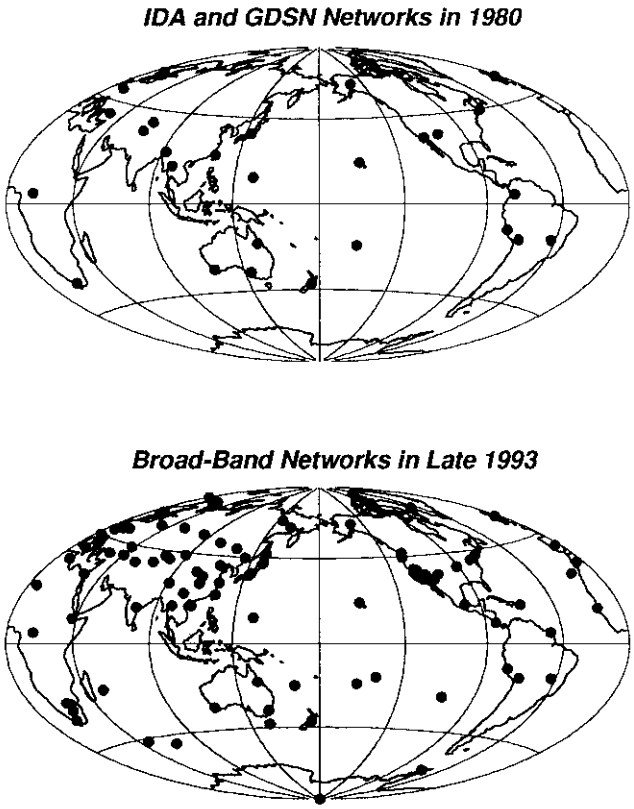

Figure 2. (Top) Long-period and broad-band seismic stations from the Global Digital Seismographic Network (GDSN) and the International Deployment of Accelerometers (IDA) operating in 1980. (Bottom) Broadband seismic stations operating in 1993. Networks displayed include the China Digital Seismograph Network (CDSN), Incorporated Research Institutions for Seismology (IRIS)/U.S. Geological Survey Global Seismograph Network (GSN), IRIS/IDA Network, Geoscope, and the Mediterranean Seismic Network (MEDNET). Coverage since 1980 has been greatly improved in Asia owing to the GSN, IRIS/IDA, and CDSN stations and in the Indian Ocean owing to Geoscope. The southern hemisphere, in particular Africa and South America, remains poorly covered, as does the Pacific Basin. Improvements in coverage in all areas continue.

member institutions through IRIS's Data Management Center at the University of Washington, the first FDSN data center. These data include a growing number of stations which are part of IRIS's GSN, the French Geoscope network, the Mediterranean Seismic Network (MEDNET) operated by the Italians, the Japanese POSEIDON network, the China Digital Seismograph Network, the German GEOFON network, and the Canadian National Seismic Network. Temporary networks are deployed regularly by the IRIS Program for Array Seismic Studies of the Continental Lithosphere (PASSCAL) and the Dutch Network of Autonomously Recording Seismographs (NARS) programs. An internationally funded Ocean Seismic Network (OSN) is being considered for potential future deployment. Compilations of seismic parametric data, including body wave travel times and earthquake source parameters, are produced by a number of organizations, notably including the International Seismographic Centre (ISC) in England and the National Earthquake Information Service, which is part of the USGS.

Seismic data are divided into three major types: body waves, surface waves, and normal modes. In this paper we do not differentiate between surface waves and normal modes. Normal mode and surface wave notation and terminology are discussed in Appendix A. Seismic body wave nomenclature is somewhat complicated, and we review only a very limited aspect of it here. As is well known, compressional and shear waves are denoted by P and S, respectively. Each surface bounce is denoted by an additional letter or letters. For example, an S wave that bounces off the free surface is denoted SS; if it bounces off the CMB, it is denoted ScS. The leg of a wave that propagates into the outer core is denoted with a K, so that a P wave that propagates through the outer core is called PKP. If the P wave pierces the inner core, it is called $PKIKP$. The phases S and SS or S and ScS follow similar paths near the earthquake and the receiver and are frequently referred to as phase pairs, and the differential travel time between each member of the set is commonly used; e.g., SS-S, PP-P, ScS-S, and so forth. The relative arrival times of these phase pairs are called differential travel times. Figure 3 displays paths of a subset of these phases.

1.3. Studies Leading to the 3-D Mantle Models

Studies subsequent to the ground-breaking work of *Dziewonski et al.* [1977] and *Masters et al.* [1982]

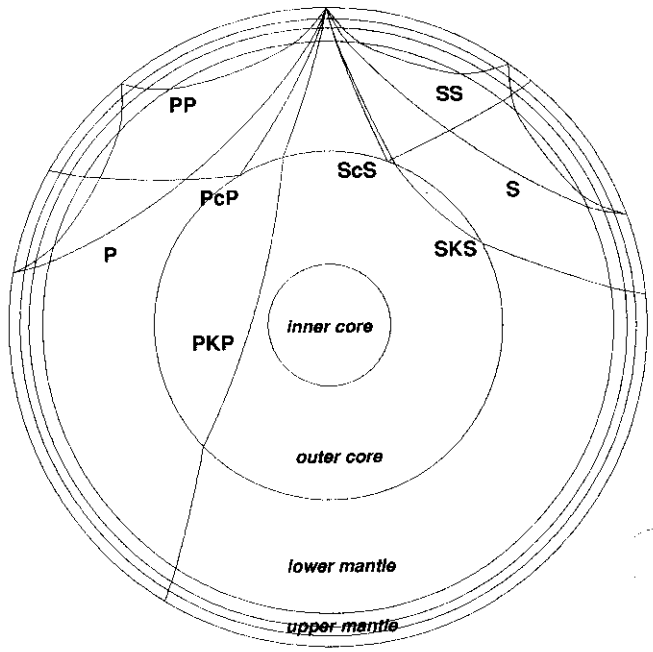

Figure 3. Body wave nomenclature.

which have played a significant role in improving the earliest pictures of the Earth's three-dimensional structure can be broadly classified according to the data upon which they are based. The kinds of data employed include (1) large collections of *P*, *PKP*, and *PKIKP* travel times [e.g., *Clayton and Comer*, 1983; *Dziewonski*, 1984; *Creager and Jordan*, 1986; *Morelli et al.*, 1986; *Morelli and Dziewonski*, 1987; *Spakman et al.*, 1988; *Gudmunsson et al.*, 1990; *Doornbos and Hilton*, 1989; *Inoue et al.*, 1990; *Pulliam et al.*, 1993; *Vasco et al.*, 1993; *Stark and Hengartner*, 1993; *Rodgers and Wahr*, 1993], (2) measurements of the locations of spectral peaks of surface wave modes interpreted asymptotically and measurements of phase and group velocity of surface waves [e.g., *Nakanishi and Anderson*, 1982, 1983, 1984; *Leveque and Cara*, 1983, 1985; *Nataf et al.*, 1984, 1986; *Tanimoto and Anderson*, 1984, 1985; *Davis*, 1987; *Smith and Masters*, 1989a; *Roult et al.*, 1990; *Montagner and Tanimoto*, 1990, 1991], (3) complete waveforms of mantle waves used as data in a least squares inversion [*Woodhouse and Dziewonski*, 1984; *Snieder*, 1988; *Tanimoto*, 1990a], (4) waveforms of long-period body waves [*Woodhouse and Dziewonski*, 1989; *Tanimoto*, 1990a; *Hara et al.*, 1993; *Su et al.*, 1994], (5) complete spectra of split multiplets in the free oscillation spectrum [*Ritzwoller et al.*, 1986, 1988; *Woodhouse et al.*, 1986; *Giardini et al.*, 1987, 1988; *Li et al.*, 1991a, b; *Widmer and Masters*, 1992], (6) differential and absolute *S* wave travel time measurements [e.g., *Woodward and Masters*, 1991a, b; *Su et al.*, 1992], (7) measurements of surface wave amplitude anomalies to constrain elastic and anelastic structures in the upper mantle [*Woodhouse and Wong*, 1986; *Wong*, 1989; *Romanowicz*, 1990; *Durek et al.*, 1993], (8) phase conversions, reflections, and reverberations [e.g., *Revenaugh and Jordan*, 1989, 1991a, b; *Shearer*, 1991a, b, 1993; *Neele and Snieder*, 1992; *Shearer and Masters*, 1992; *Vidale and Benz*, 1992; *Wicks and Richards*, 1993], and (9) quasi-Love and quasi-Rayleigh wave observations [e.g., *Park and Yu*, 1992; *Yu and Park*, 1993]. Recent reviews of various aspects of 3-D seismic imaging are given by *Masters and Ritzwoller* [1988], *Dziewonski and Woodhouse* [1987], *Masters* [1989], *Romanowicz* [1991], *Dziewonski and Woodward* [1992], and *Montagner* [1994].

Studies of class 1 have illuminated lower mantle *P* velocity structure and those of classes 2 and 3 have led to models of upper mantle *S* velocity. The addition of classes 4, 5, and 6 has enabled the placement of constraints on lower mantle *S* velocity structure. Studies of class 7 have yielded the first global images of anelasticity in the upper mantle, and studies of class 8 have resulted in the first global models of topography on the mantle's internal boundaries. Earlier topographic models of the boundaries surrounding the mantle have come from studies of types 1 and 5. Studies of classes 2 and 9 have yielded new information about anisotropy below the lithosphere.

Now, several global-scale aspherical elastic models of the mantle have been constructed, including M84A and M84C [*Woodhouse and Dziewonski*, 1984], LO2.56 [*Dziewonski*, 1984], MDLSH [*Tanimoto*, 1990a], SH.10c.17 [*Masters et al.*, 1992], and S12_WM13 [*Su et al.*, 1994]. The characterization of each of these models is deferred to section 2.1.

1.4. A Qualitative Picture of 3-D Mantle Structure

A coherent qualitative picture of the 3-D structure of the Earth has emerged from the 3-D models discussed here. (General discussions are given by *Silver et al.* [1988], *Jordan et al.* [1989], *Hager and Clayton* [1989], *Olson et al.* [1990], *Romanowicz* [1991], and *Su and Dziewonski* [1991].) Figure 4a presents contour maps of the aspherical perturbations in shear velocity relative to the velocity of the reference spherical model PREM for the models S12_WM13, SH.10c.17, M84C, and MDLSH at a depth of 50 km. Figures 4b to 4h are similar to Figure 4a, but the models are plotted at depths of 200, 400, 650, 750, 1500, 2200, and 2800 km, respectively. General description of the models can be found in Table 1. The correlations of the latter three models with S12_WM13 at these depths are listed in Table 2.

An inspection of these figures reveals that in the upper mantle, large-scale structure conforms to the expectations of plate tectonics: low velocities underlie the mid-oceanic ridge system, and high velocities underlie continental shields and platforms. High-velocity material in the upper mantle, presumably associated with cold downwelling regions, appears to merge continuously into the lower mantle. Low-velocity material, which is typically interpreted as high-temperature upwelling regions, does not appear to grade as continuously from the upper to the lower mantles. The Transition Zone marks the region where low-velocity material may undergo this discontinuity. Within this emerging qualitative picture, the Transition Zone remains well named, since its 3-D structure appears to have elements in common with both the upper mantle and the lower mantle. Its strong degree 2 pattern of heterogeneity corresponds with the locus of subduction in the upper mantle, but its low-velocity regions do not appear to be associated either with the upper mantle low velocities beneath oceanic ridges or with the lower mantle low velocities beneath the African continent and the south central Pacific region.

In the lower mantle, the magnitude of heterogeneity is smaller than in the upper mantle and appears to be dominated by a radially continuous ring of high-velocity material that when projected onto the surface is nearly a great circle around the Pacific. This ring corresponds to the projection into the lower mantle of the subducted slabs from the upper mantle and separates two diffuse columns of low-velocity material that do not appear to be located beneath the mid-oceanic ridges, but rather are correlated with high surface topography, geoid highs, and volcanic hotspots. The

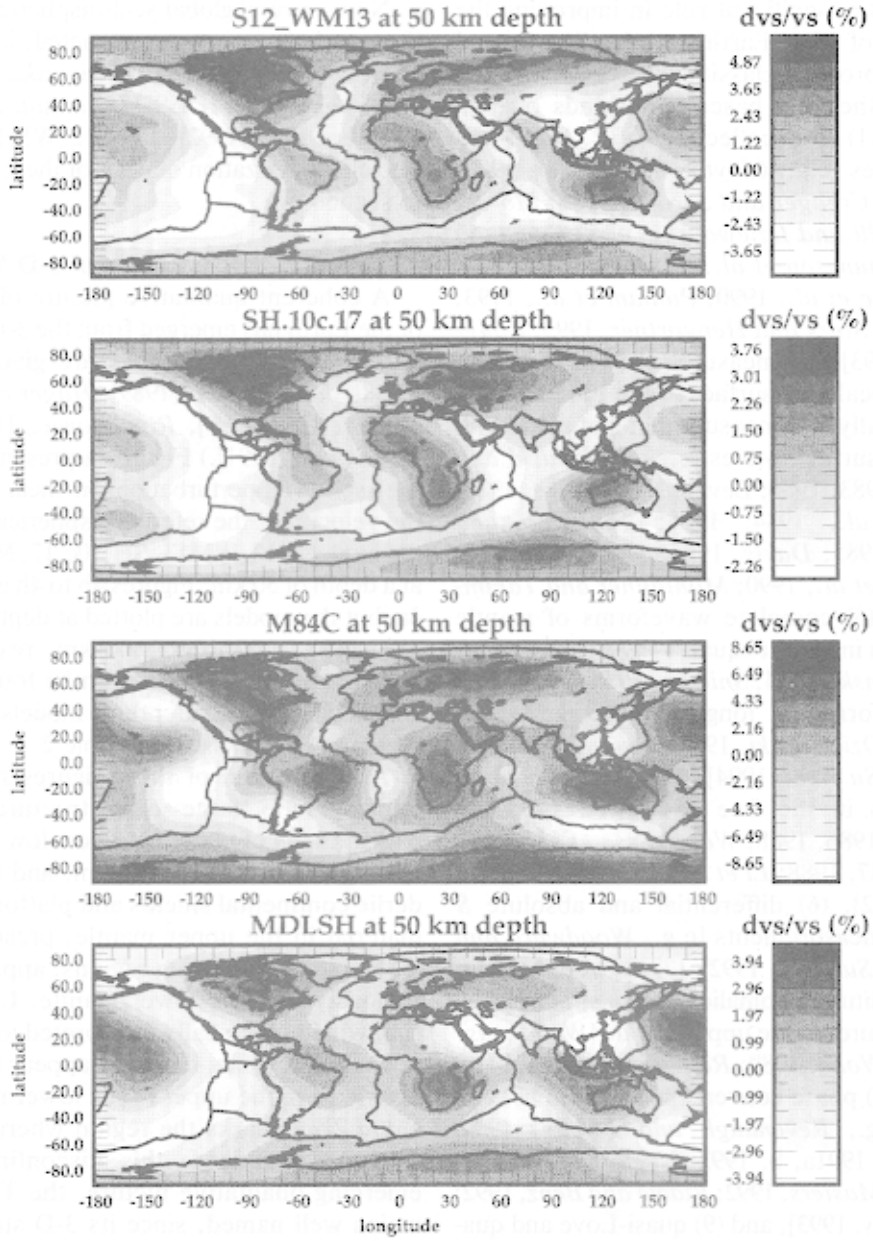

Figure 4a. Contour maps of the volumetric models S12_WM13, SH.10c.17, M84C + LO2.56, and MDLSH at 50-km depth. Each model is represented as a perturbation in shear wave velocity at each point relative to the spherically symmetric average from PREM: $\delta v_s(r, \theta, \phi)/v_s(r)$ in percent. The geographical correlations of SH.10c.17, M84C + LO2.56, and MDLSH with S12_WM13 at this depth and those for Figures 4b to 4h are listed in Table 2.

D'' region appears to be considerably more heterogeneous than the rest of the lower mantle, having more of the characteristics of the upper mantle. As a boundary layer between the mantle and core, the D'' layer is likely to be the inverse image of the crust-lithosphere system, a region characterized by chemical heterogeneity and differentiation as well as by high heat conduction.

1.5. The Nature of This Paper

If the three-dimensional seismic models are to fulfill the promise of producing information relevant to a wide range of geophysical problems, such as providing deep and abiding insight into mantle dynamics, agreement among them should be better than merely qualitative. The purpose of this paper is to compare and characterize quantitatively a set of tomographic models (including M84A and M84C, LO2.56, MDLSH, SH.10c.17, and S12_WM13), to assess their similarities and differences, and to analyze their fit to one class of data: the normal mode structure coefficients which are specific radial integrals of aspherical elastic structure. Previous discussions of the fit of some of

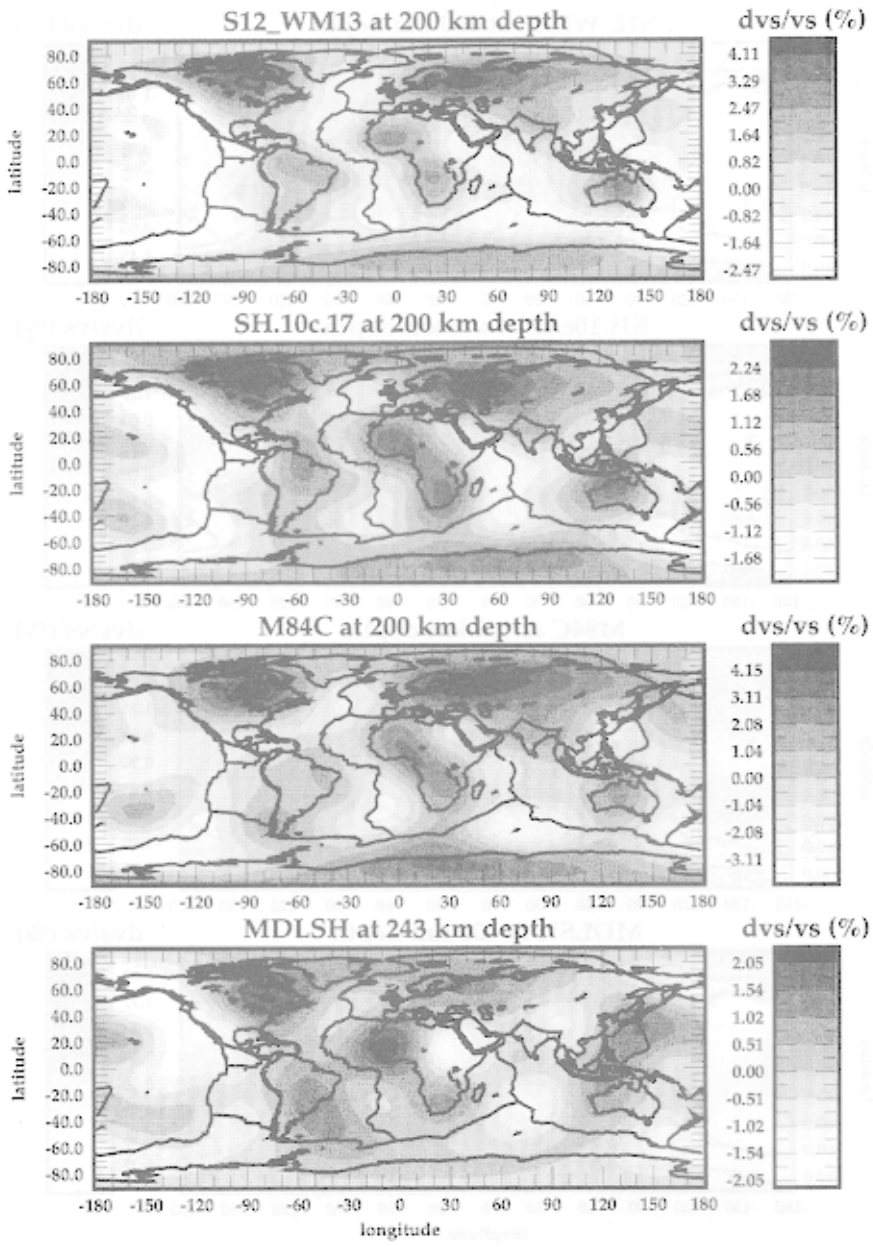

Figure 4b. Same as Figure 4a, but at 200-km depth.

these models to normal mode structure coefficients are given by *Ritzwoller et al.* [1988], *Smith and Masters* [1989a], and *Woodward and Masters* [1991a]. Comparisons of certain aspects of a subset of the models considered here are given by *Romanowicz* [1991], *Su and Dziewonski* [1991], *Garnero and Helmberger* [1993], and *Jordan et al.* [1993].

In the following, we will concentrate on comparing general features of the models, such as the root-mean-square (rms) amplitude and the radial and geographical distribution of structure, rather than on comparing specific features that compose the models. Also, we will focus on comparing certain radial integrals of the models by discussing the normal mode structure (or interaction) coefficients and splitting functions (defined by equations (7) and (9), respectively) predicted by each model. Other studies have begun the laborious process of comparing the models feature by feature. For example, *Nishimura and Forsyth* [1989], *Forsyth* [1992], *Su et al.* [1992], *Zhang and Tanimoto* [1992], and *Zhang et al.* [1994] discuss and differ on the depth extent of the mid-oceanic ridges. *Montagner* [1994] discusses common features in some recent 3-D models in the hope of illuminating convection in the mantle.

In section 2 the characteristics of each of the mantle models considered in this paper are described, and in section 3 the nature and distribution of heterogeneity are discussed by comparing model statistics (rms amplitude, and radial and geographical correlation). An important aspect of this paper is the assessment of the

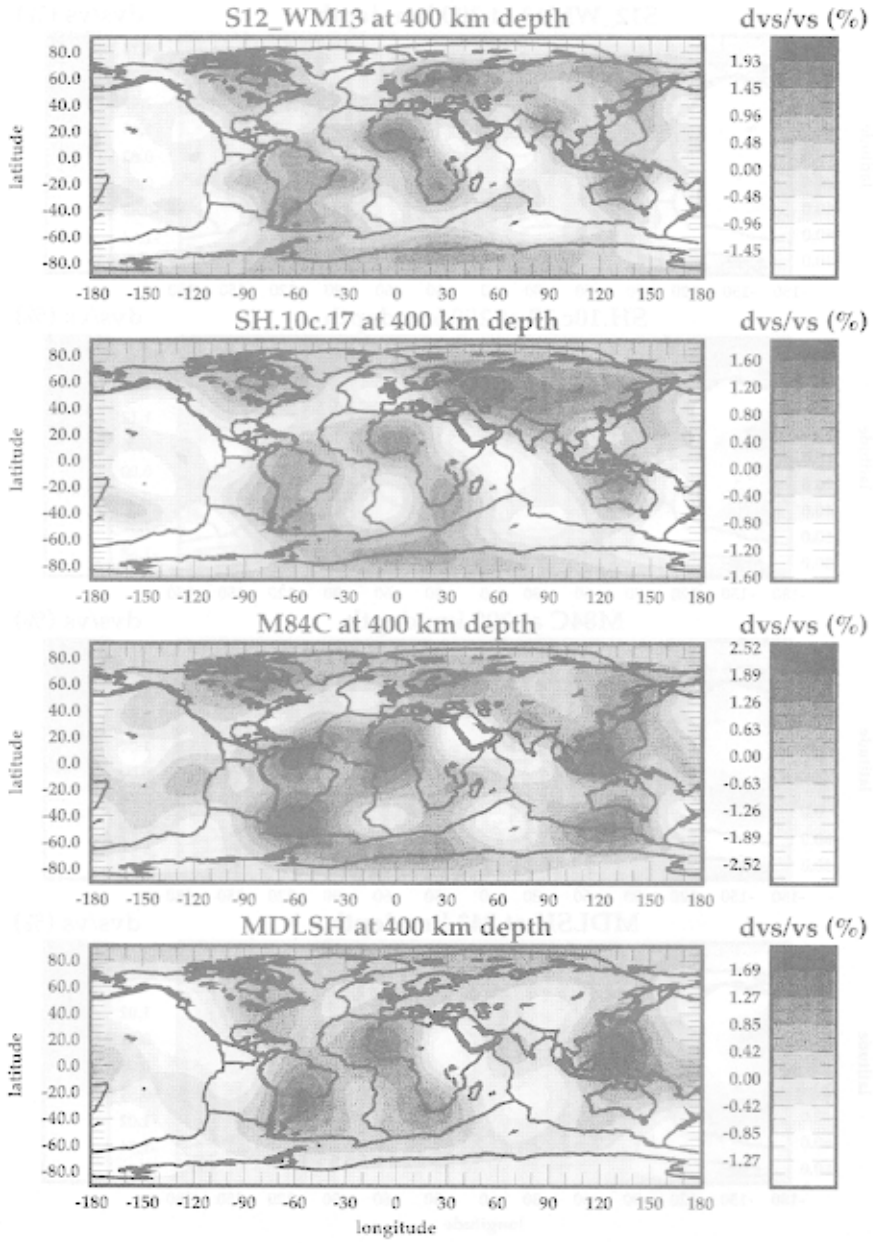

Figure 4c. Same as Figure 4a, but at 400-km depth.

fit of observed normal mode structure coefficients to those predicted from each of the models. In section 4 we describe the normal mode data with which the model predictions will be compared and discuss the corrections that must be applied to the data before comparisons can be made. In section 5 the misfit of the mantle models to the observed normal mode structure coefficients and splitting functions is assessed, and a summary of the conclusions, drawn from the observations in sections 3 and 5, is given in section 6. The discussions in sections 4 and 5 are quite technical, and the summary in section 6 is designed to help the reader who wishes to forgo some of the technical details. Discussion of some of the potential sources of the discrepancies between the models and of the misfit with normal mode data is included in section 7. A discussion of the potential for drawing geodynamical interpretations from radial correlation functions is contained in section 8. The paper concludes with a set of recommendations for the focus of future research in section 9. Appendices A and B comprise an overview of surface wave and normal mode notation, terminology, and data corrections.

2. THE MODELS

2.1. Description of the Models

In this section we characterize and compare the global mantle models M84C [*Woodhouse and*

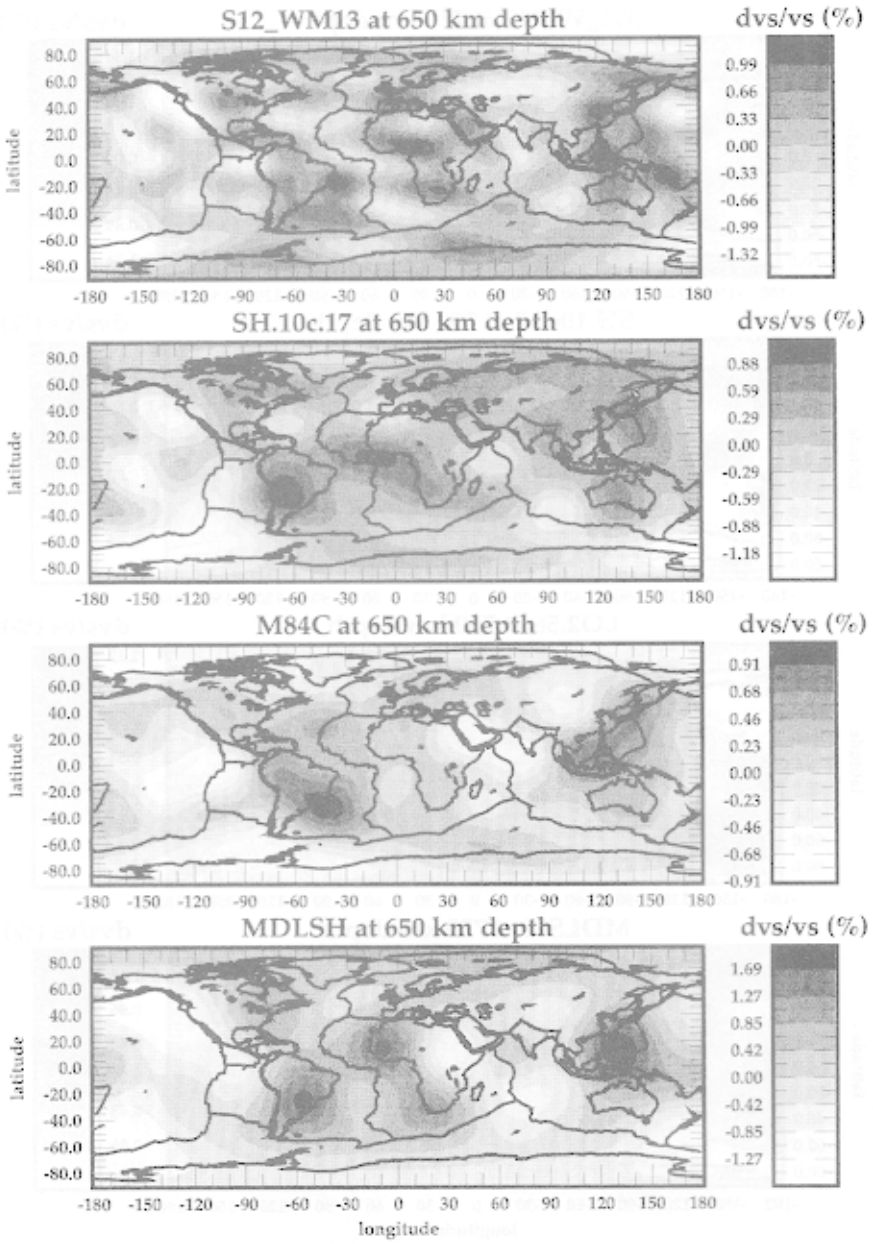

Figure 4d. Same as Figure 4a, but at 650-km depth.

Dziewonski, 1984], LO2.56 [*Dziewonski*, 1984], MDLSH [*Tanimoto*, 1990a], SH.10c.17 [*Masters et al.*, 1992], and S12_WM13 [*Su et al.*, 1994]. We will refer to each of these models by the names that seismologists usually use for them. These names are admittedly somewhat arcane, but it is worth retaining them here for consistency with the original studies.

There are other global mantle models that are deserving of review but which we do not explicitly discuss here. Notable examples are the models of *Nataf et al.* [1986], *Inoue et al.* [1990], *Montagner and Tanimoto* [1991], *Pulliam et al.* [1993], and *Zhang and Tanimoto* [1993]. The reason is simple: each of these models covers only part of the mantle, and to compare predicted and observed normal mode structure coefficients, we would like whole mantle models and have limited ourselves to such models. Nevertheless, we would like to apologize to the listed authors.

Taken together, the models we consider here are based on data types that span three orders of magnitude in frequency (1 Hz to 1 mHz), including, for example, short-period P wave travel time residuals (LO2.56), normal mode splitting functions (SH.10c.17), differential travel times of intermediate body wave phase pairs (SH.10c.17, S12_WM13), and complete waveforms of long-period surface waves (M84C, S12_WM13, MDLSH) and body waves (S12_WM13, MDLSH). None of these models accounts for the dispersion effects caused by lateral variations in intrinsic attenuation, although they do correct for phys-

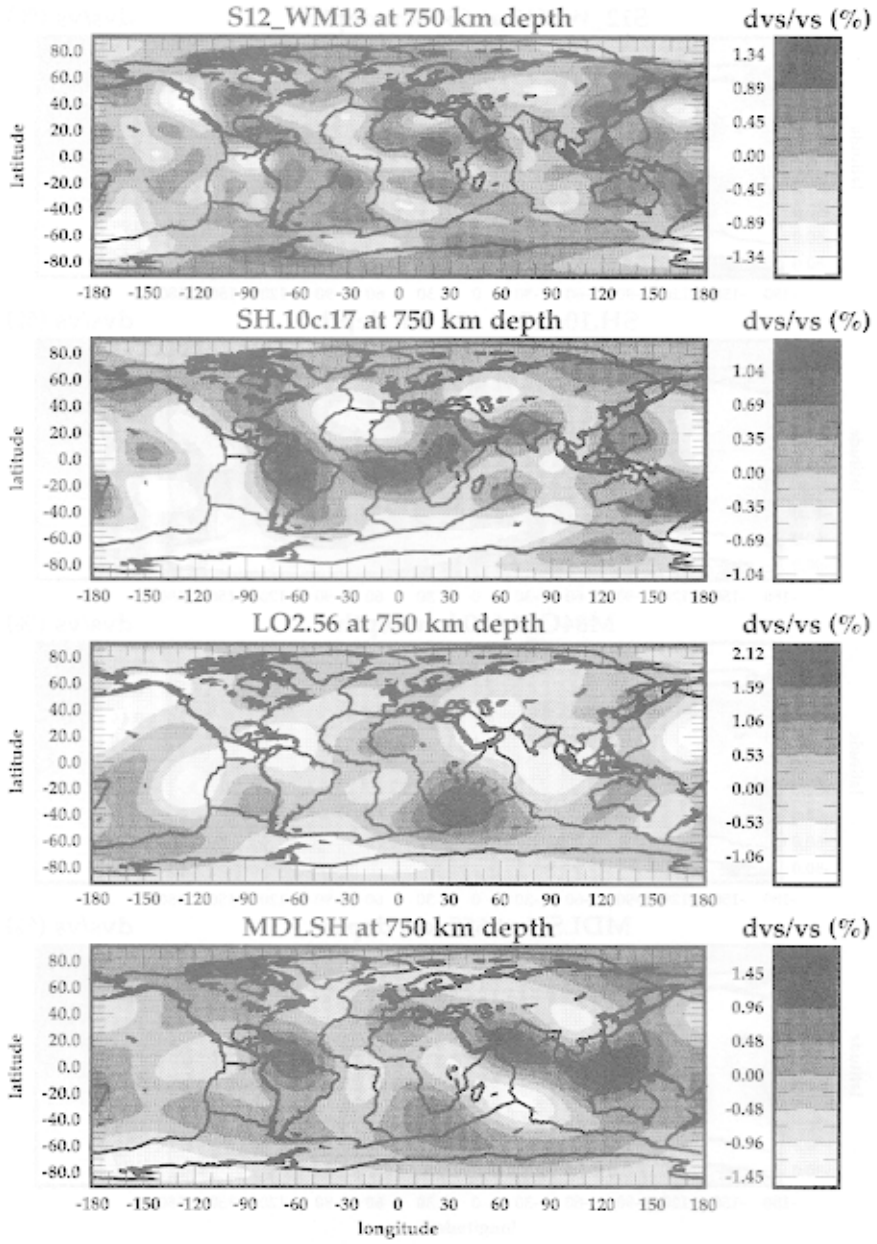

Figure 4e. Same as Figure 4a, but at 750-km depth.

ical dispersion caused by spherically symmetric attenuation. With the exception of LO2.56, which is a δv_p model, the models all represent shear velocity perturbations, δv_s. Table 1 summarizes the models.

The earliest global-scale models, M84C and LO2.56, are upper and lower mantle models, respectively. M84C was constructed from long-period surface wave data, and LO2.56 was derived from *P* wave travel times compiled by the ISC. M84C fit surface wave phase perturbations based on an asymptotic normal mode theory developed for that purpose. When a whole mantle model is required, for example, in computing structure coefficients in sections 4 and 5, we merge M84C and LO2.56 and consider them to constitute a single whole mantle model, M84C + LO2.56. These models have been superseded by the whole mantle model S12_WM13, which was constructed from long-period differential *ScS-S* and *SS-S* travel times, absolute *S* and *SS* travel times, and long-period body (>45 s period) and mantle waveforms (3–7 mHz). The method of joint inversion of travel time and waveform data is described by *Dziewonski et al.* [1993].

The model SH.10c.17 incorporates the fitting of long-period absolute *S* wave travel times and some higher-order *S* multiples, differential *ScS-S* and *SS-S* travel times, and normal mode (Rayleigh, Love, and overtone) splitting functions with frequencies from less than 1 mHz to approximately 7 mHz. Only normal mode phase information was used to estimate the structure coefficients, and this limits the normal modes

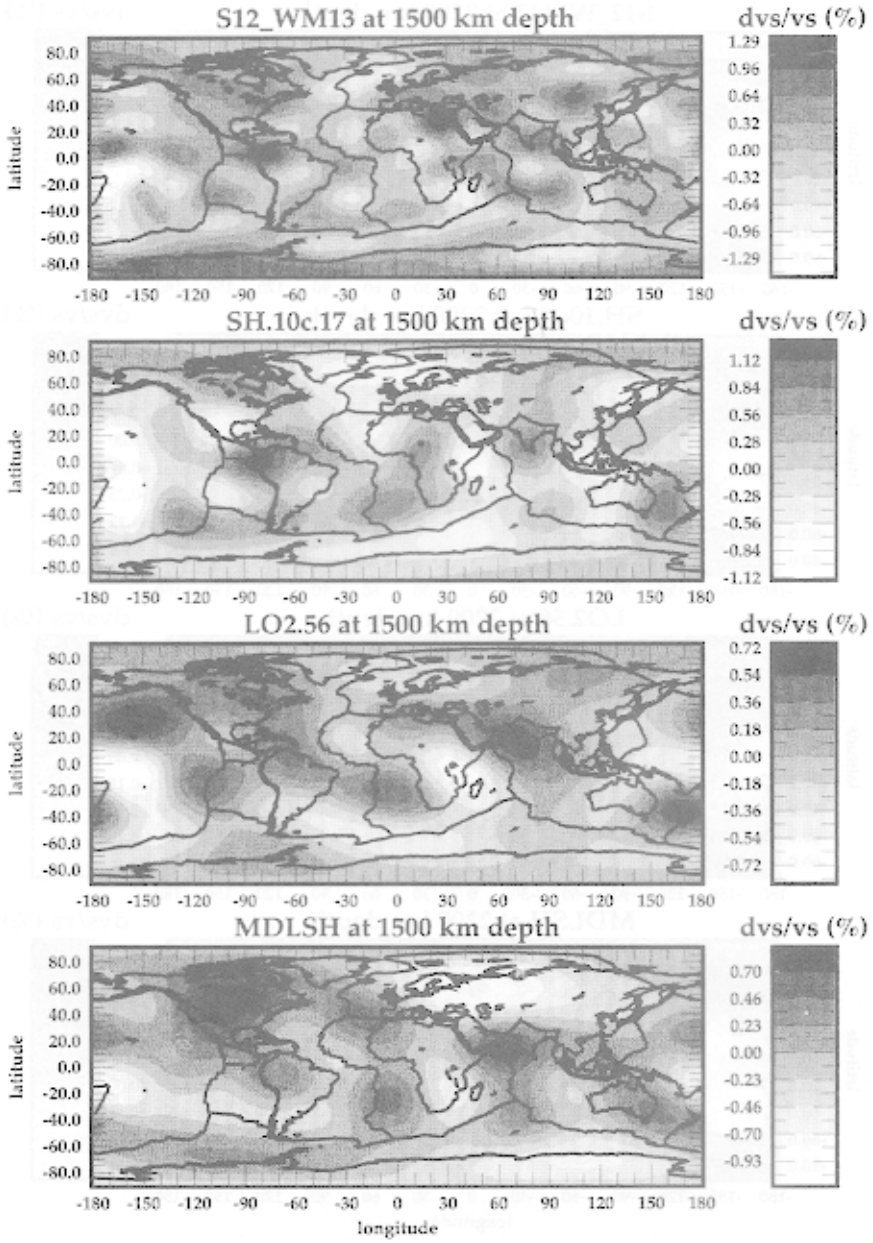

Figure 4f. Same as Figure 4a, but at 1500-km depth.

to constrain only the even degree part of SH.10c.17. The inversion method is similar to that described by *Woodward and Masters* [1991a]. This model is currently under further development through use of absolute and differential P times, and a v_p part of the model will soon become available (H. Bolton, personal communication, 1993). The models SH.10c.17 and S12_WM13 are not completely independent, since they share differential travel time measurements of the phase pairs *ScS-S* and *SS-S* and one researcher (R. Woodward).

The model MDLSH is based on long-period (40–100 s) SH waves and long-period Love waves (100–500 s) using a waveform-fitting method [*Tanimoto*, 1990a] similar to that developed for the M84 models [*Woodhouse and Dziewonski*, 1984]. This model differs from the other models in that no Rayleigh wave data were used in its construction.

Each of these models is purely volumetric; that is, there are no boundary perturbations to the major mantle discontinuities below the crust. LO2.56 is a degree 6 lower mantle model. M84A and M84C are degree 8 upper mantle models, and S12_WM13, SH.10c.17, and MDLSH are degree 12, degree 8, and degree 6 whole mantle models, respectively. SH.10c.17 and MDLSH are spherically layered models in which there is no variation with depth in each shell; they contain 11 and 12 spherical shells, respectively. The radial variation of the other models is parameterized by Legendre or Chebyshev polynomials.

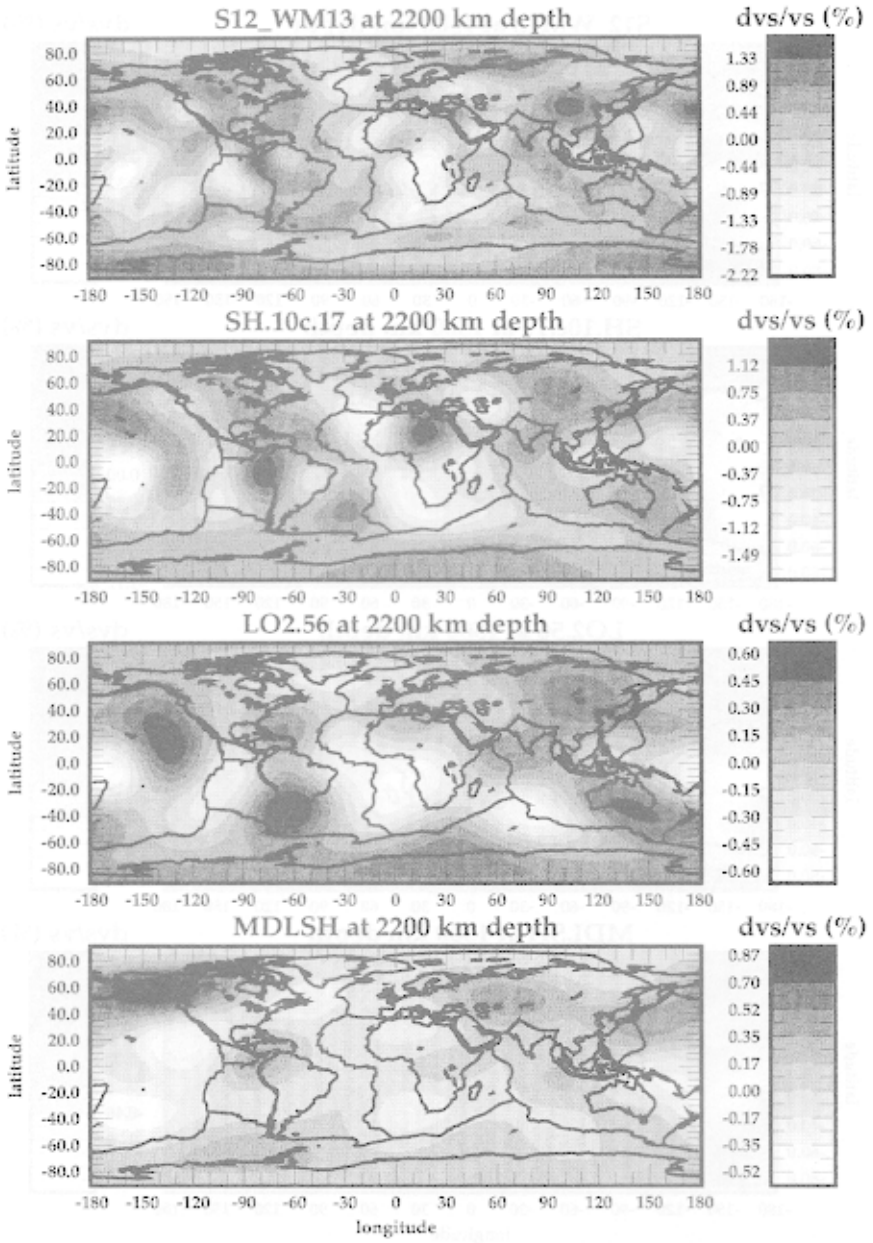

Figure 4g. Same as Figure 4a, but at 2200-km depth.

2.2. Scaling Relationships Between v_s, v_p, and ρ

The combination of travel time and surface/mantle wave data requires the resulting models to contain both v_s and v_p structures since the surface/mantle wave data are sensitive to both. However, the limited size and nature of the data sets employed make it difficult to estimate the independent parameters simultaneously ($(\delta v_s, \delta v_p$, and $\delta\rho)$ or $(\delta\mu, \delta\kappa$, and $\delta\rho)$). This has required, on inversion, a reduction in the number of independent model parameters, usually to a single function of radius, through the use of empirical scaling relationships among the elastic parameters and density. With the exception of LO2.56, the volumetric models considered here are fundamentally shear velocity models. For the models that result from joint body wave–surface wave inversions, perturbations in shear velocity (δv_s) were taken as proxy for the perturbations in density ($\delta\rho$) and compressional velocity (δv_p) through whole mantle linear scaling relationships. The compressional velocity and density models have been derived from the shear velocity models with the following linear scaling relationships:

$$\frac{\delta v_p}{v_p} = \left(\frac{dlnv_p}{dlnv_s}\right)\frac{\delta v_s}{v_s}, \qquad (3)$$

$$\frac{\delta\rho}{\rho} = \left(\frac{dln\rho}{dlnv_s}\right)\frac{\delta v_s}{v_s},$$

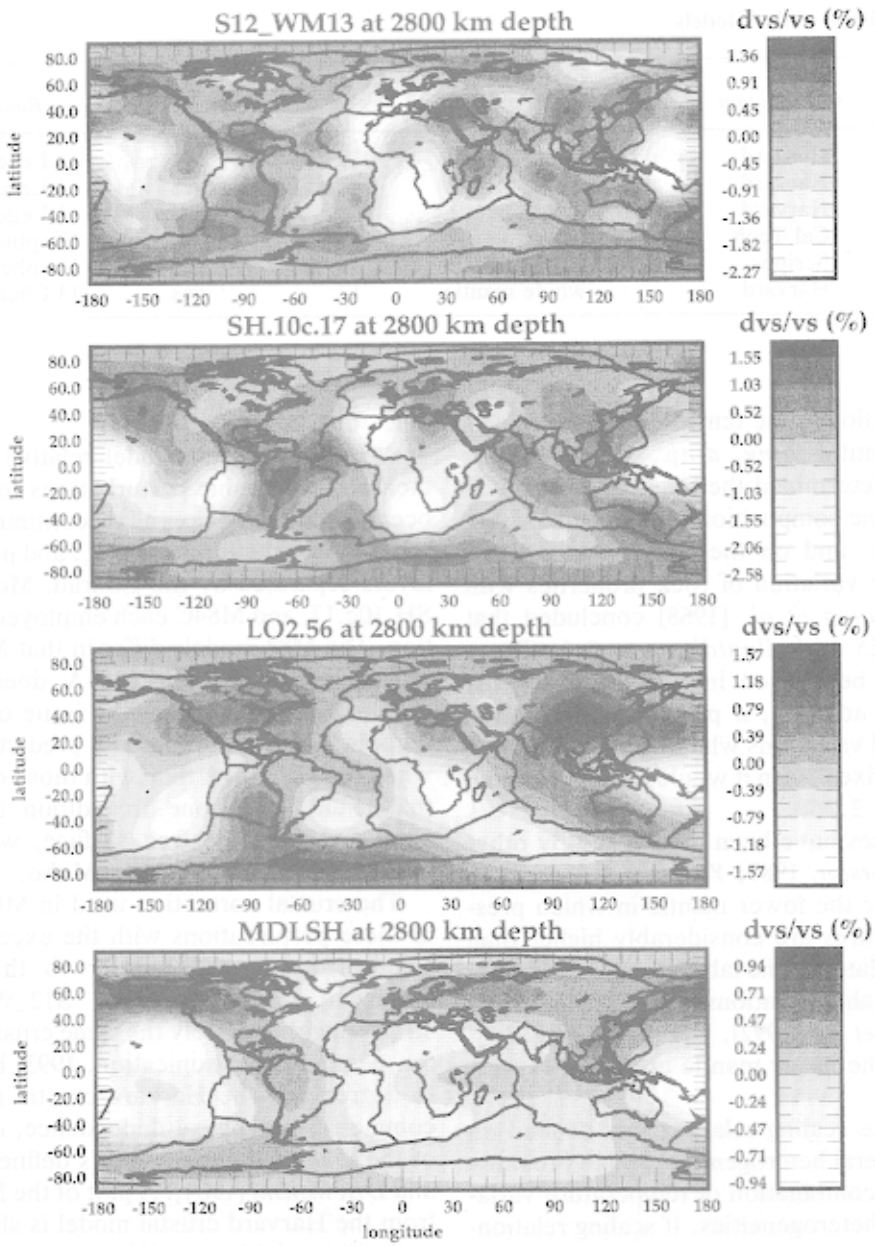

Figure 4h. Same as Figure 4a, but at 2800-km depth.

where the scaling coefficients are $d\ln v_p/d\ln v_s$ and $d\ln\rho/d\ln v_s$.

The use of scaling relationships is surrounded by considerable uncertainty; for discussions see *Ritzwoller et al.* [1988] and *Li et al.* [1991b]. The scaling relationships for the shear velocity models listed in Table 3 are those used in their construction, and are the scaling relationships that we adopt in the forward computations presented in this paper. Since LO2.56 is a P wave travel time model that employed neither S waves nor surface waves in its inversion, no scaling relationship was assumed in its construction. For LO2.56, we use $d\ln v_s/d\ln v_p = 2.0$ as advocated by *Li et al.* [1991b] for comparison with the δv_s models and in computing the structure coefficients in section 5. The M84 models are purely shear models; they possess no perturbations in compressional velocity or density. Since MDLSH was constructed using only S wave data, no scaling relationships were used in the construction of this model. Since *Tanimoto* [1990a] indicates that he followed procedures very similar to those used in deriving M84A and M84C, we assign to MDLSH the scaling values used in the construction of those models. As will be discussed in section 5.1c, this choice exacerbates the comparison of MDLSH with certain overtone structure coefficients which are dominantly sensitive to the compressional velocity variations in the lower mantle.

The substantiation for the use of linear scaling relationships results from the observation of the near

TABLE 1. Characteristics of the Models

Model	*Date*	*Organization*	*Type*	*Region*	*Maximum Degree, s*	*Input Crustal Model?*	*Radial Representation*
M84A	1984	Harvard	v_s	upper mantle	8	no	4 Legendre polynomials
M84C	1984	Harvard	v_s	upper mantle	8	yes	4 Legendre polynomials
LO2.56	1984	Harvard	v_p	lower mantle	6	no	5 Legendre polynomials
MDLSH	1990	Cal Tech	v_s	whole mantle	6	no	12 spherical layers
SH.10c.17	1992	Scripps	v_s	whole mantle	8	yes	11 spherical layers
S12/WM13	1993	Harvard	v_s	whole mantle	12	yes	13 Chebyshev polynomials

constancy of the ratios of the temperature derivatives of the relative quantities $dln\kappa$, $dln\mu$, $dlnv_s$, and $dln\ v_p$. *Chung* [1971] determined the temperature derivative of various olivine compositions and estimated that $dlnv_s/dlnv_p \sim 1.3$, and on the basis of laboratory experiments on the variation of rock properties with temperature, *Anderson et al.* [1968] concluded that $dlnv_s/dlnv_p \sim 1.25$ and $dln\rho/dlnv_s \sim 0.4$. These values have often been used in the studies of the Earth's mantle. In addition, if partial melt were the sole cause of lateral variations which affected μ alone, while κ and ρ were fixed, then it would be easy to show that $dlnv_s/dlnv_p \sim 2.25$.

All of these values have been questioned by other authors [e.g., *Anderson*, 1987; *Yeganeh-Haeri et al.*, 1989], especially for the lower mantle in which pressures and temperatures are considerably higher than the conditions simulated in the laboratory. In addition, the use of linear scaling relationships has been questioned by *Masters et al.* [1992], who argue that their new v_p models in the lower mantle are poorly correlated with v_s.

The values of the scaling relationships depend on the nature of the lateral heterogeneity, which probably derives from some combination of temperature variations and chemical heterogeneities. If scaling relationships are, indeed, well defined for the Earth, their estimation, in conjunction with experimental results on rock properties at mantle conditions, may illuminate the cause of large-scale mantle heterogeneities and discriminate between different mantle mineralogies.

TABLE 2. Correlation of Models With S12_WM13

Depth, km	*SH.10c.17*	*M84C + LO2.56*	*MDLSH*
50	0.85	0.74	0.68
200	0.92	0.92	0.44
400	0.69	0.64	0.54
650	0.57	0.48	0.67
750	0.45	0.04	0.38
1500	0.27	0.43	0.27
2200	0.74	0.69	0.50
2800	0.78	0.57	0.48

2.3. Crustal Corrections

A general crustal model relative to PREM would include topographic perturbations to the free-surface, ocean-solid layer, Conrad discontinuity, and Moho, as well as perturbations to v_p, v_s, and ρ in the two crustal layers separated by the Conrad. Models S12_WM13, SH.10c.17, and M84C each employed a crustal correction. The M84 models differ in that M84C possesses a crustal correction but M84A does not. *Tanimoto* [1990a] does not discuss the issue of the crustal correction, but since his model predictions agree better with those of M84A than with those of M84C, we infer that he did not use one. In addition, his model extends all the way to the free surface, whereas the other models are truncated at the Moho.

The crustal correction used in M84C contained all of these perturbations with the exception of the density perturbation. We refer to this model as the "Harvard" crustal model. S12_WM13 was constructed with precisely the same crustal correction (W. Su, personal communication, 1993) but was extended to degree 12. The Harvard crustal model assumes a common geographical dependence, $q(\theta, \phi)$, for each of the four boundaries, and is defined by *Woodhouse and Dziewonski* [1984]. A plot of the Moho topography from the Harvard crustal model is shown in Figure 5.

Smith and Masters [1989a], *Woodward and Masters* [1991a], *Widmer and Masters* [1992], and *Masters et al.* [1992] used a crustal model that parameterizes all of the aforementioned perturbations with the exception of topography on the Conrad discontinuity. This model, which we refer to as the "Scripps" crustal model, does not assume a common geographical pattern for each of the boundaries.

TABLE 3. Scaling Relationships

Model	$dlnv_p/dlnv_s$	$dln\rho/dlnv_s$
S12_WM13	0.8	0.4
SH.10c.17	0.8	0.4
LO2.56	0.5	0.4
M84C	0.0	0.0
M84A	0.0	0.0
MDLSH	0.0	0.0

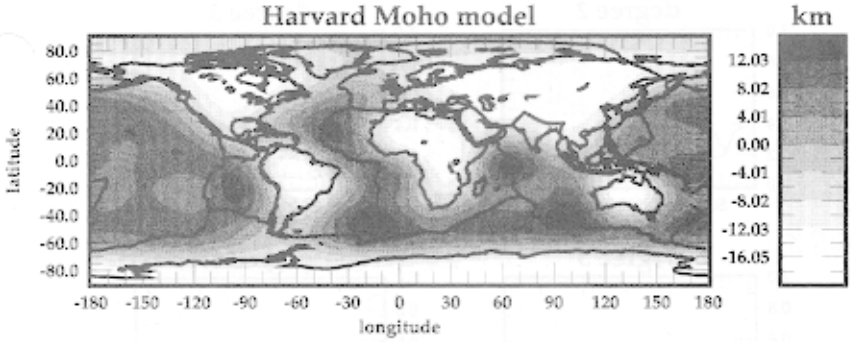

Figure 5. Topography (in kilometers) on the Moho, from the Harvard crustal model.

3. MODEL STATISTICS

Although it is somewhat illuminating to inspect visually the contour maps of the models at similar radii as in Figure 4, differences and similarities between the models appear more clearly by directly comparing the amplitudes of the models as well as computing their geographical correlations as a function of radius, both across models (geographical or cross correlation) and within a model (radial correlation or autocorrelation).

3.1. Root-Mean-Square Amplitudes

The amplitudes of the models are examined as a function of radius by computing the root-mean-square (rms) of the amplitude of the model relative to the amplitude of PREM, which is defined as follows:

$$\mathrm{rms}(r) = \frac{1}{m_0(r)} \left[\int |m(r, \theta, \phi)|^2 \, d\Omega(\theta, \phi) \right]^{1/2}$$

$$= \frac{1}{m_0(r)} \left[\sum_{s,t} |\delta m_s^t(r)|^2 \right]^{1/2}, \quad (4)$$

where the volumetric model $m(r, \theta, \phi)$ is defined in equation (1). Figures 6a and 6b show the rms of the models S12_WM13, M84C + LO2.56, SH.10c.17, and MDLSH for each degree of structure independently (in sequential panels) and also the total rms amplitude (bottom right-hand panel), all as a function of depth. The greatest rms amplitudes for all of the models are in the top several hundred kilometers of the mantle. As is well known [e.g., *Su and Dziewonski*, 1991], the amplitude of each of the models is enriched in long wavelengths, declines rapidly with depth in the upper mantle, reaches a minimum between 1000- and 1500-km depth, and then gradually increases to peak in the D'' layer for all degrees.

As Figure 6a shows, the models M84C + LO2.56 and S12_WM13 have similar rms values across most of the mantle, with the major exceptions being near the top of the mantle, where M84C has anomalously large amplitudes, and near the top of the lower mantle (670- to 800-km depth), where LO2.56 is poorly constrained. LO2.56 and S12_WM13 also differ somewhat in amplitude between 1500- and 2500-km depth. Comparison with Figure 6b indicates that the amplitudes of these models generally lie above those for SH.10c.17 in the upper mantle but below the values for SH.10c.17 at depths between 500 and 1200 km. The models S12_WM13 and SH.10c.17 are most similar in rms amplitude in the lower half of the lower mantle. As is discussed in section 7.1, about half of the difference in amplitude in the upper mantle between S12_WM13 and SH.10c.17 can be attributed to the differences between the Harvard and Scripps crustal models. The other half may be related to the fact that SH.10c.17 appears to spread heterogeneity across the upper mantle more evenly than S12_WM13, perhaps because of the slightly lower resolution of the basis functions of SH.10c.17 or because of different data weighting. The amplitude of MDLSH in the upper mantle is intermediate between SH.10c.17 and the Harvard models but is considerably lower in amplitude in the lowermost mantle than the other three models, especially near the base of the lower mantle.

The degree spectrum of heterogeneity for each model is shown in Figure 7. The amplitude of the heterogeneity is enriched at long wavelengths at all depths in the mantle. *Stewart* [1992] interpreted this as being caused by the dominance of low-degree convection patterns, which she argued are caused by the nonlinear coupling of convective modes through temperature dependent viscosity. *Jarvis and Peltier* [1986] argued that the radial dependence of the model rms can be used to constrain the location of boundary layers. Steep temperature gradients lead to localized peaks in the rms of temperature anomalies, which in turn are expressed as velocity perturbations. For example, the rms in Figure 7 peaks at degrees 4 to 5 in the upper mantle and corresponds to the dominant length scale of the tectonic plates. The localized peaks in rms at degree 2 near the base of both the upper and lower mantles may indicate the presence of a stratification boundary [*Peltier and Solheim*, 1992; *Jarvis and Peltier*, 1986]. Further evidence for the location of boundary layers is discussed in sections 3.3 and 8. (See also *Tanimoto* [1990c].) The lack of localized

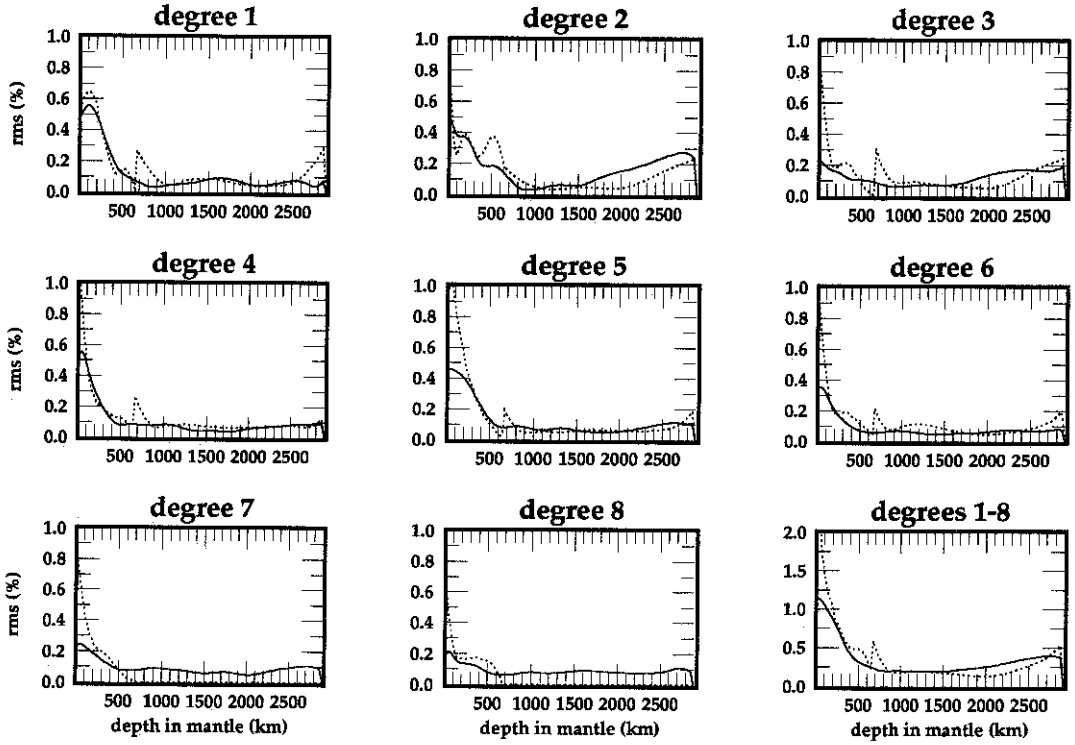

Figure 6a. The root-mean-square (rms) value (equation (4)) of the aspherical volumetric structure of the models S12_WM13 (solid line) and M84C + LO2.56 (dotted line) as a function of depth in the mantle. Units are percent perturbation relative to the spherical reference shear velocity at the given depth from PREM. Each panel corresponds to a single harmonic degree of structure, and the bottom right-hand panel is the total rms over all degrees. M84C saturates the scale in the total rms panel, obtaining a maximum at 2.5% rms at the top of the upper mantle. All plots begin at the Moho. (LO2.56 extends only to degree 6 in the lower mantle.)

peaks in the middle mantle is suggestive of chemically homogeneous, adiabatic convection.

3.2. Geographical or Cross Correlations

The cross-correlation function between two spherical harmonic models δm and $\delta \bar{m}$ over all degrees at a given radius r is given by

$$\rho_c(r) = \frac{\sum_{s,t} \delta m_s^t{}^*(r)\delta \bar{m}_s^t(r)}{\left[\sum_{s,t} |\delta m_s^t(r)|^2\right]^{1/2}\left[\sum_{s,t} |\delta \bar{m}_s^t(r)|^2\right]^{1/2}}. \quad (5)$$

This expression assumes that the models are parameterized with fully normalized complex spherical harmonics as in (1). The correlation coefficient is independent of the amplitudes of the models. The associated confidence levels for each degree correlation coefficient are computed using the formalism of *Eckhardt* [1984] and are shown in Figure 8.

Rather than display all possible permutations of correlations between the models considered here, we adopt S12_WM13 as a reference model and compute the correlation of this model with the models SH.10c.17, M84C + LO2.56, and MDLSH. The result is shown in Figure 9. The correlation for each harmonic degree between 1 and 8 is displayed in sequential panels, and the total correlation is shown in the bottom right-hand panel. The value of the correlation coefficient at each degree related to the 90% confidence level is marked in Figure 9 with an arrow on the right side of each panel. Arbitrary confidence levels can also be read from Figure 8.

The correlation between S12_WM13 and M84C in the upper mantle is high at all degrees but tends to decline as the 660-km discontinuity is approached from above, especially for the higher degrees. In the depth range between 660 km and 1300 km, the correlation between S12_WM13 and LO2.56 falls to negative values. This is consistent with the differences between these two models in rms and suggests that the top 500–700 km of the lower mantle is poorly resolved in LO2.56. Thus a decade after models M84C and LO2.56 were first produced, the region of greatest change in the Harvard models appears to be the top of the lower mantle.

The correlations of S12_WM13 with SH.10c.17 and with M84C + LO2.56 over individual degrees and the combined contribution from degrees 1–8 are generally very similar, except near the top of the lower mantle.

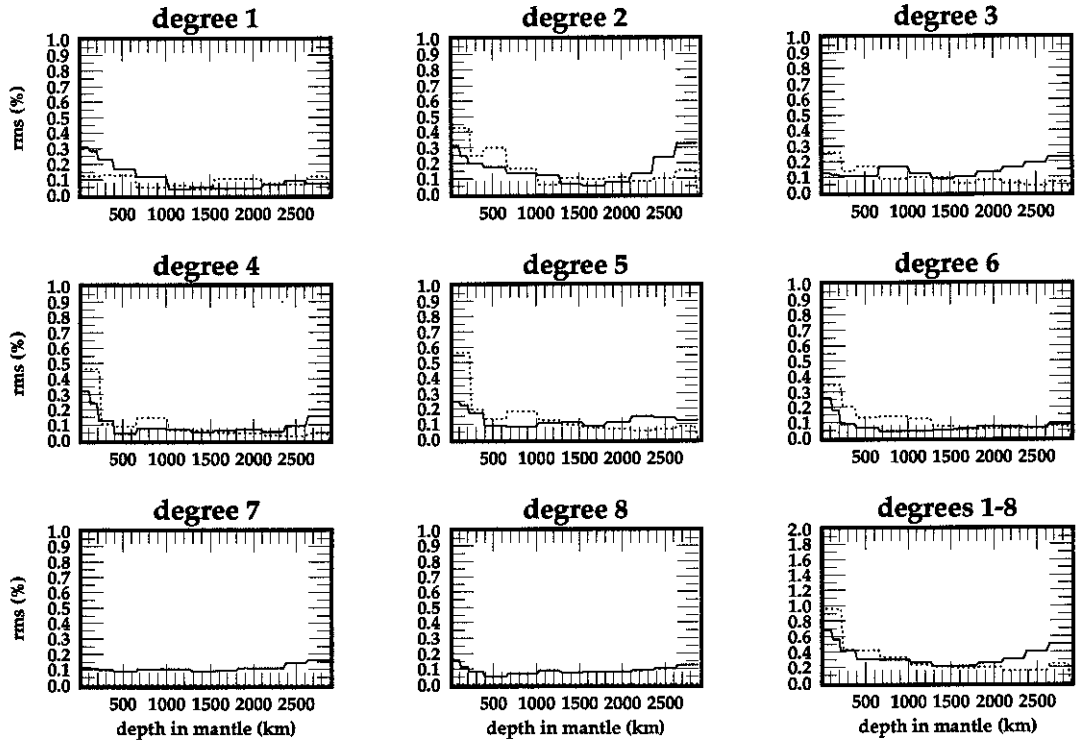

Figure 6b. Same as Figure 6a, but for models SH.10c.17 (solid line) and MDLSH (dotted line). The scales are the same as in Figure 6a to aid comparison. (MDLSH extends only to degree 6.)

The correlation between S12_WM13 and SH.10c.17 is greatest in the upper mantle and bottom one third of the lower mantle. The correlation between S12_WM13 and MDLSH is poor in the upper mantle above the Transition Zone compared with the other two models, is lowest in the top two thirds of the lower mantle (consistent with the other models) and has a weaker correlation in the bottom one third of the lower mantle relative to the other models.

Aspects of the distribution of heterogeneity of MDLSH in the upper mantle differ from the other models; for example, MDLSH has a negative correlation relative to S12_WM13 at degree 2 in the low-velocity zone. In contrast with the rms of MDLSH, which is significantly lower than the other models in the lowermost mantle, the correlation between MDLSH and the other models is lowest in the upper mantle above the Transition Zone. Thus MDLSH appears different in two major respects from the other models: the top 400 km of MDLSH appears to be geographically different than the other models, and its amplitude is significantly different in the lowermost mantle.

3.3. Radial Correlations or Autocorrelations

The radial or vertical coherence of aspherical Earth models can be characterized with the radial correlation function $R(r, r')$, which defines the geographical correlation of aspherical structure on the spherical surfaces r and r'. The variation in this function with radius identifies the characteristic scales of radial change within a model. (In contrast, the geographical or cross correlations discussed in section 3.2 represent variations between models.) The use of this function to characterize global 3-D seismic Earth models was used previously by *Tanimoto* [1990c] and by *Jordan et al.* [1993].

An expression for $R(r, r')$ for models parameterized in terms of spherical harmonics can be obtained from the geographical correlation function, $\rho_c(r)$, by the transformation $\delta\bar{m}_s^t(r) \rightarrow \delta m_s^t(r')$ applied in equation (5). $R(r, r')$ defines a two-dimensional function whose value is unity on the diagonal ($r = r'$), and whose decay away from the diagonal characterizes the rate of decorrelation of structures on spherical surfaces as their radii separate. It is common to assign a radial correlation length, l_c, on the basis of $R(r, r')$. This assignment is somewhat arbitrary. *Jordan et al.* [1993] suggest that l_c is usefully defined by the solution of the implicit equation $R(r - l_c/2^{1/2}, r + l_c/2^{1/2}) = x$, for $x = 0.75$. For the sake of comparison with their work, we will also use this definition in the plots of correlation length presented here.

Figure 10 displays the radial correlation functions of the models S12_WM13, SH.10c.17, M84C + LO2.56, and MDLSH. The original parameterization of each model has been retained; i.e., the discrete shell models (SH.10c.17 and MDLSH) were not fitted to smooth functions of radius. This explains the checkerboard appearance of $R(r, r')$ for these models and explains

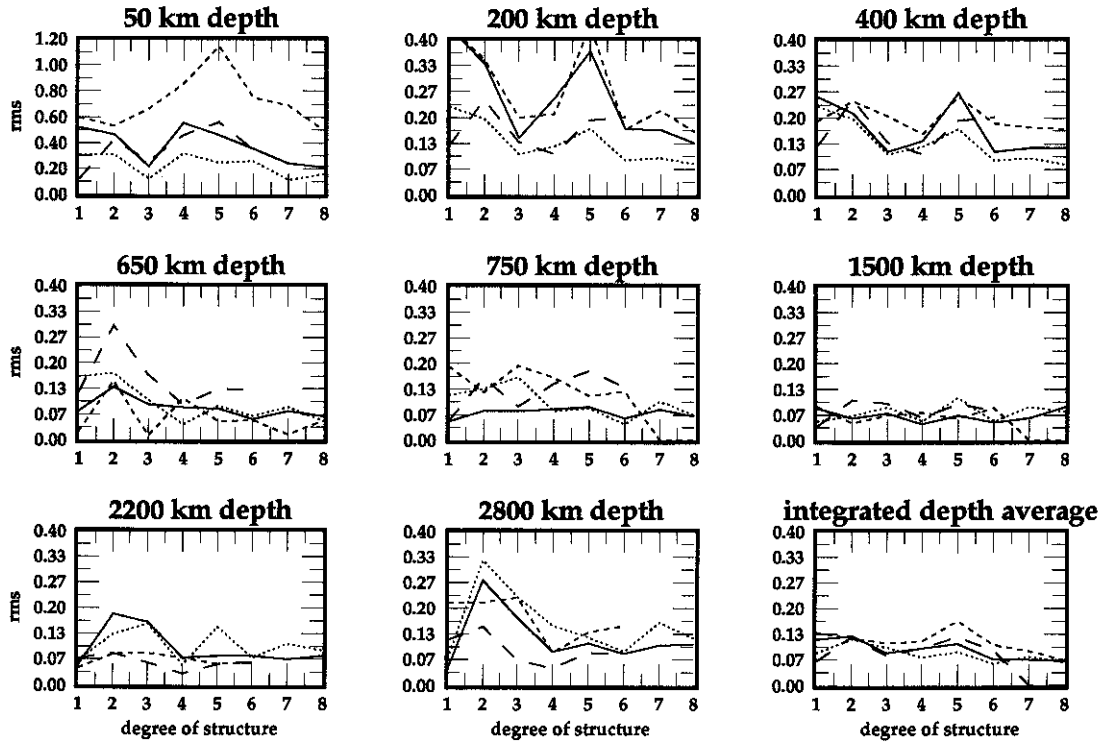

Figure 7. The root-mean-square (in percent relative to PREM) as a function of harmonic degree of structure at depths corresponding to those in Figures 4a to 4h for S12_WM13 (solid line), SH.10c.17 (dotted line), M84C + LO2.56 (short-dashed line), and MDLSH (long-dashed line). The bottom right-hand panel is the integrated value of the rms from the core-mantle boundary to the Moho.

as well the different appearance of $R(r, r')$ for SH.10c.17 in the *Jordan et al.* [1993] work. The vertical and horizontal lines indicate the radius of the 660-km boundary. By definition, the correlation value of the diagonal blocks of the discrete shell models is unity, and the diagonal lines in S12_WM13, M84C, and LO2.56 indicate that $R(r, r) = 1$. The central banded structures in Figure 10 reveal the characteristic correlation lengths as a function of radius.

There is, in general, an anticorrelation of structure in the Transition Zone with structure in the lower mantle. This negative correlation between upper mantle and lower mantle structures has been noted and discussed before [e.g., *Hager et al.*, 1985], in the context of predicting the Earth's gravity field.

The correlation length l_c for each of the models is plotted in Figure 11. It is greatest near the base of the lower mantle and, on average, decreases toward the

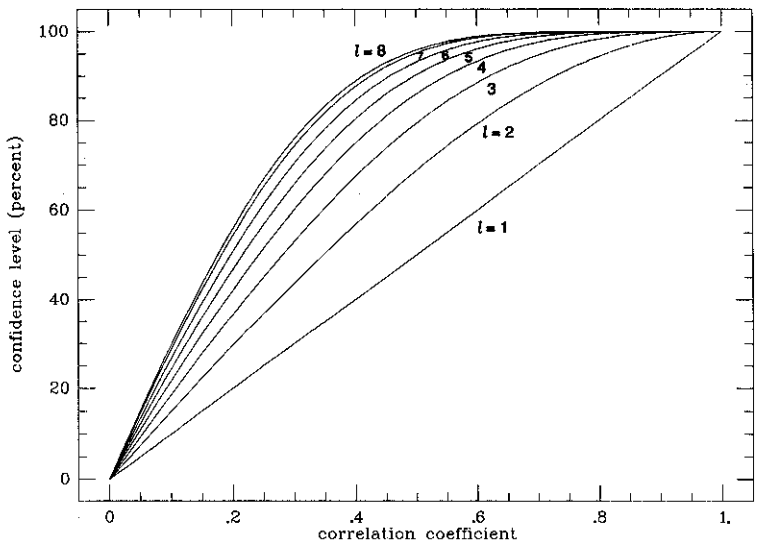

Figure 8. Relationships between the correlation coefficient computed between two spherical harmonic expansions for degrees $l = 1-8$ and the confidence level that the null hypothesis does not hold. For example, a correlation coefficient of 0.5 between the $l = 5$ parts of two spherical harmonic expansions results in a confidence level of correlation of approximately 90%.

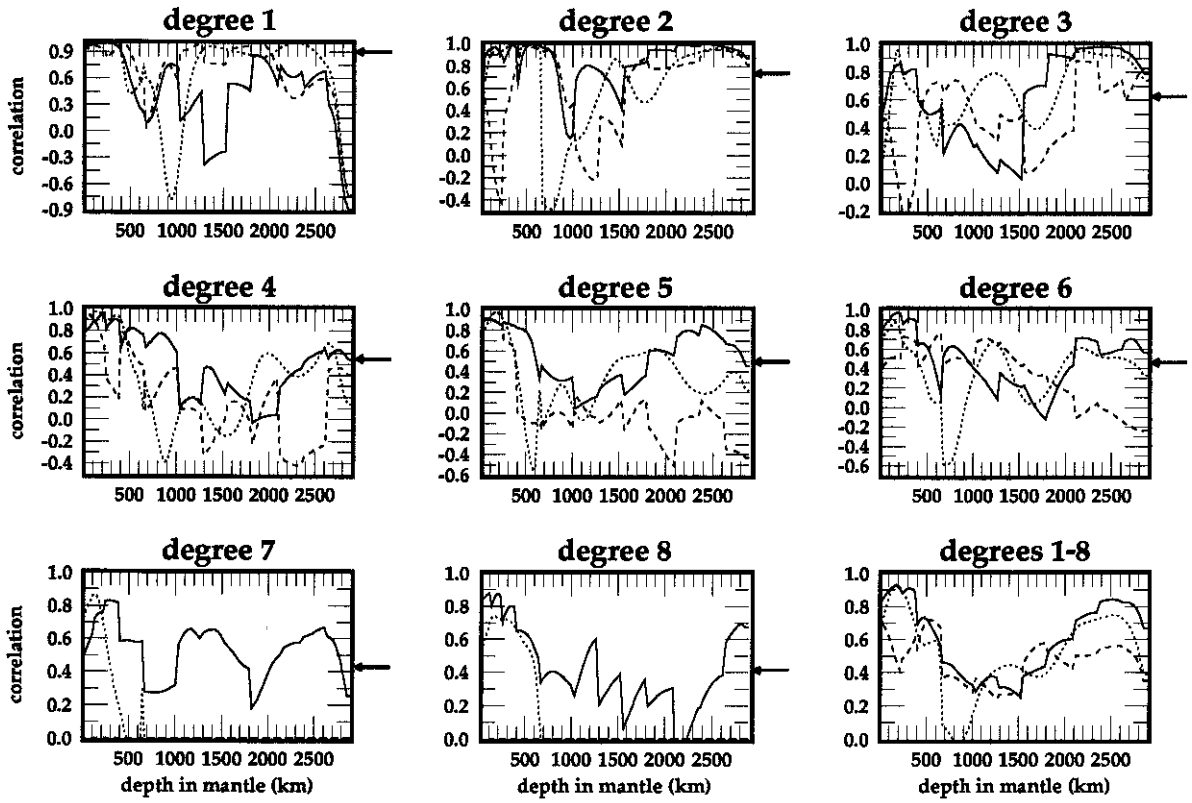

Figure 9. Geographical cross correlation (equation (5)) of S12_WM13 with the models SH.10c.17 (solid line), M84C + LO2.56 (dotted line), and MDLSH (dashed line) as a function of depth in the mantle. Each panel corresponds to a single harmonic degree of structure and the bottom right-hand panel is the total correlation over all degrees. The 90% confidence level for each of the degree correlations is indicated with an arrow on the right side of each panel. Arbitrary confidence levels can be read off of Figure 8. (LO2.56 and MDLSH extend only to degree 6.)

surface. The models S12_WM13, SH.10c.17, and LO2.56 have correlation lengths of approximately 400–750 km in the lowermost mantle, falling to 100–300 km in the upper mantle. The radial correlation length of MDLSH in the lowermost mantle is higher than the other models but falls to comparable values above the D'' layer.

There are depths at which l_c decreases sharply or the radial correlation function pinches in one or more of the models. The location and character of these local minima in l_c or a decorrelation across a boundary are potentially interesting, since *Jordan et al.* [1993] argue that the nature of chemical or phase changes in the mantle can be constrained by comparing the observed radial variation of correlation length with the predictions of numerical mantle convection models. They argue that convective models with phase or chemical discontinuities display a local minimum of l_c, a pinching of $R(r, r')$, or a poor correlation across a boundary in the neighborhood of the boundary (i.e., a relative decorrelation across the boundary) and, potentially, a change in the dominant length scales across the boundary. We merely point out here the variations of l_c and jumps in correlation observed in the computed radial correlation functions and defer a discussion of their potential dynamical implications to section 8.

The hybrid model M84C + LO2.56 is characterized by a discontinuity in $R(r, r')$ at 660-km depth as seen in Figure 10. This results from the fact that M84C and LO2.56 are models that were constructed from independent data sets. No constraints of smoothness across the 660-km boundary were applied in the inversion or were even effectively applied by the data. Rather, inverted structure beneath the boundary was constrained by P wave data alone (LO2.56), and structure above the boundary was constrained by surface wave data (M84C). The coherence of structure across the 660-km boundary is contained within Figure 10 but is illustrated more clearly in Figure 12. The solid and dotted lines in this figure represent, respectively, horizontal slices of the radial correlation functions 20-km below and 20-km above the 660-km discontinuity for each of the models; i.e., $R(r, r_{660} - 20)$ and $R(r, r_{660} + 20)$ for $r_{CMB} \leq r \leq r_{Moho}$. The correlation of structure across the 660-km boundary for SH.10c.17 and MDLSH is 0.70 and 0.54, respectively. Therefore MDLSH provides a hint of decorrelation across the

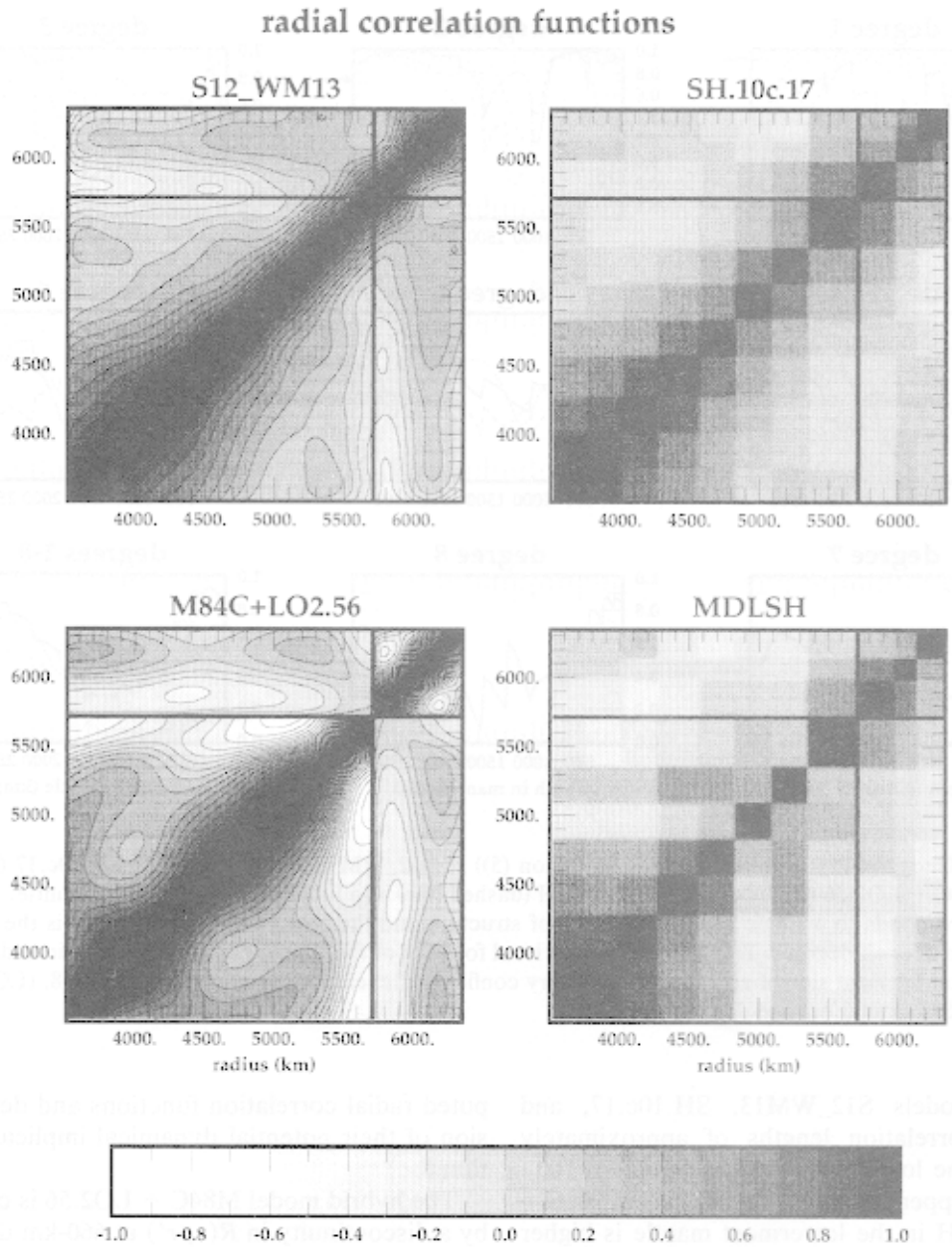

Figure 10. The radial correlation function $R(r, r')$ for the models S12_WM13, SH.10c.17, M84C + LO2.56, and MDLSH. $R(r, r')$ is the geographic correlation of structure on spherical surfaces at the radii r and r'. $R(r, r')$ is unity on the diagonal ($r = r'$), and its rate of decrease specifies the rate of decorrelation with increasing radial separation. The width of the bands about the diagonal specifies the characteristic vertical correlation length l_r of the models.

660-km boundary, but it is not very compelling. Perhaps more interestingly, SH.10c.17, LO2.56, and MDLSH appear to decorrelate more strongly at a depth of approximately 1000 km. The radial correlation between adjacent layers at depth 1022 km is only 0.59 for SH.10c.17 and 0.18 for MDLSH.

4. THE NORMAL MODE DATA AND CORRECTIONS

The aspherical models considered here are perturbations to mantle structure. To compare the predictions of these models with the observed normal mode data, it is necessary to add to the model predictions the effects of an assumed crustal model and Coriolis coupling, where appropriate. The crustal corrections can be surprisingly large, but the Coriolis correction is significant only for a limited range of multiplets along the fundamental branch. In section 4.1 the normal mode structure coefficients that constitute the normal mode data used in this study are defined. In section 4.2 we discuss how the structure coefficients are computed for the crustal models. As is discussed further in section 7.1, the differences between the Harvard and

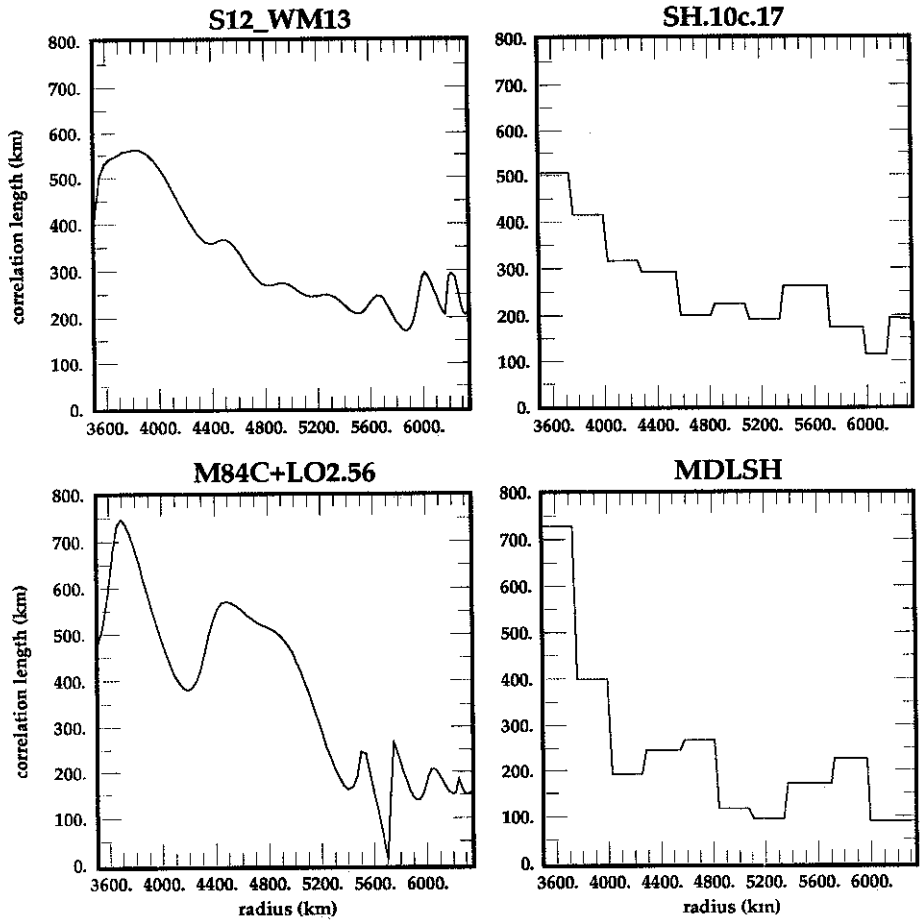

Figure 11. Correlation length as a function of radius in the mantle for each of the four mantle models.

Scripps crustal models can probably be considered to be a lower bound on the error of the crustal correction. In Appendix A, general normal mode notation and terminology are presented, and the correction to the structure coefficients for Coriolis coupling is described in Appendix B.

4.1. Normal Mode Structure Coefficients

The effect of both volumetric structure and boundary topography on normal modes is contained in the components $H^{m'm}_{k'k}$ of the splitting matrix $\mathbf{H}_{k'k}$ [*Woodhouse and Dahlen*, 1978]. Here $k = (n, l)$ is the multiplet identifier. Ignoring contributions from the Earth's rotation, ellipticity of figure, and the interaction between multiplets ($k = k'$), the splitting matrix can be written

$$H^{m'm}_{kk} = \sum_s \sum_{t=-s}^{s} \gamma^{m'm}_s {}_k c^t_s, \tag{6}$$

where $\gamma^{m'm}_s$ depends on Wigner 3-j symbols and t is constrained to the value $m' - m$ by the selection rules that govern $\gamma^{m'm}_s$. The normal mode structure (or interaction) coefficients are denoted by ${}_k c^t_s$ and are simply related to aspherical volumetric and boundary structures:

$${}_k c^t_s = \int_0^a {}_k K_s(r)\ \delta m^t_s(r)\ dr + \sum_d {}_k D_{ds} h^t_{ds}, \tag{7}$$

$${}_k c^t_s = {}_k \tilde{c}^t_s + {}_k \hat{c}^t_s, \tag{8}$$

where ${}_k \tilde{c}^t_s$ is the structure coefficient computed from volumetric structure alone and ${}_k \hat{c}^t_s$ is the structure coefficient computed from boundary structure alone. Here, $K_s(r)$ is the volumetric kernel and ${}_k D_{ds}$ is the boundary kernel for boundary d, both given by *Woodhouse and Dahlen* [1978], and $\delta m^t_s(r)$ and h^t_{ds} represent the spherical harmonic coefficients for the volumetric structure (e.g., δv_s, δv_p, $\delta\rho$) and boundary topography, respectively, given by equation (1). The fully normalized complex spherical harmonics $Y^t_s(\theta, \phi)$ are normalized according to the convention of *Edmonds* [1960]. Equation (7) is valid only for even order s structure coefficients. Odd order structure coefficients are defined in a similar way, but they are more complicated because they depend on multiplet-multiplet coupling. A full discussion of this is given by *Woodhouse* [1980].

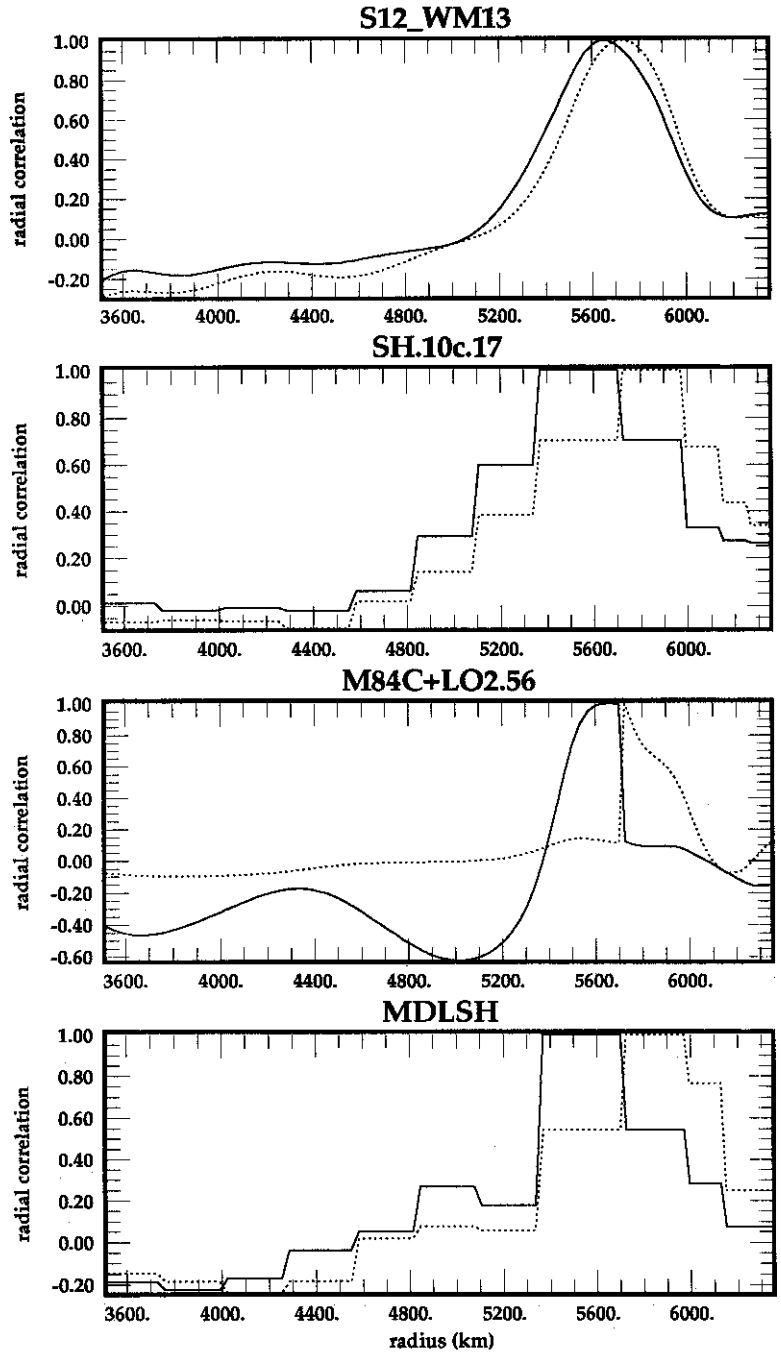

Figure 12. One dimensional projections of $R(r, r')$ for $r' = r_{660} - 20$ (solid line) and $r' = r_{660} + 20$ (dotted line), i.e., correlations of structure 20 km above and below the 660-km boundary with the structure spanning the rest of the mantle for the models S12_WM13, SH.10c.17, M84C + LO2.56, and MDLSH.

The structure coefficients for each multiplet form the splitting matrix and therefore determine the frequencies and shapes of the seismic oscillations. Their use as expansion coefficients in a spherical harmonic expansion results in splitting functions, which are defined as

$$F_k(\theta, \phi) = \sum_{s,t} {}_k c_s^t Y_s^t(\theta, \phi). \qquad (9)$$

Each splitting function is simply related to a phase velocity map [*Giardini et al.*, 1988]. This function represents the effect of aspherical structure on local frequency perturbations for a particular multiplet ${}_nS_l$. As we define them, splitting functions are each multiplied by the degenerate frequency of the multiplet with indices (n, l) and have units of microhertz. For even degree structures, the splitting functions shown in section 5.2 display even symmetry.

In this paper the fully normalized spherical harmonics described above are employed, as are the corresponding complex expansion coefficients c_s^t (where we often omit the multiplet subscript k for notational simplicity). Each scalar representation considered is real, and therefore the expansion coefficients satisfy the relation $c_s^{-t} = (-1)^t c_s^{t*}$, where the asterisk denotes the complex conjugate. Thus a degree s scalar

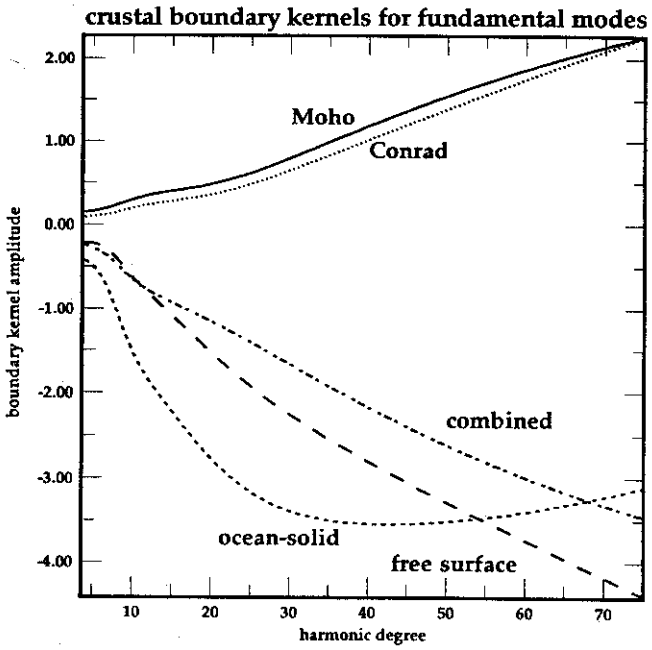

Figure 13. Amplitude of the fundamental mode boundary kernels ${}_kD_{d2}$ (equation (7)), plotted as a function of harmonic degree for the four crustal boundaries: the free surface, the ocean-solid boundary, the Conrad discontinuity, and the Moho. The line marked combined represents the combined effect of all four boundaries using the crustal model advocated by *Woodhouse and Dziewonski* [1984]. The kernels increase with increasing l as the modes compress near the surface. The combined effect is dominated by the Moho and is always negative owing to the sign of topography on the Moho (equation (10)).

field is fully specified by the azimuthal orders $0 \leq t \leq s$. The real and imaginary components of c_s^t are denoted by Re c_s^t and Im c_s^t, respectively.

Corrections to the structure coefficients due to Coriolis coupling between nearby spheroidal and toroidal multiplets are discussed in Appendix B.

4.2. Structure Coefficients of the Crustal Models

The relative influence of each of the crustal boundaries on the structure coefficients is given by the boundary kernels ${}_kD_{ds}$ found in (7) as a function of harmonic degree. Figure 13 is a plot of the degree 2 topographic kernels ${}_kD_{d2}$ for fundamental modes computed for the free surface, the ocean-solid interface, the Conrad discontinuity, and the Moho. The modulus of the kernels increases with l, since modal energy compresses near the surface at higher degrees. The relative contribution of the boundaries to the values of the structure coefficients is not based just on the size of the kernel but is also dependent on the peak-to-peak topographic amplitudes on each boundary, which is expected to be greatest on the Moho. Computations show that the volumetric contribution to the crustal correction is only a fraction of the contribution from the Moho. Therefore the combined crustal topographic contribution to the structure coefficient using the weighting based on the expected relative topography of each boundary, advocated by *Woodhouse and Dziewonski* [1984], is also shown in Figure 13. The combined topographic contribution for the Harvard crustal model can be written

$$ {}_k\hat{c}_s^t = [-0.78\,{}_kD_s^{(\text{Moho})} - 0.37\,{}_kD_s^{(\text{Conrad})} + 0.21\,{}_kD_s^{(\text{ocean-solid})} + 0.03\,{}_kD_s^{(\text{free surface})}]q_s^t, \quad (10) $$

where q_s^t is the (s, t) component of $q(\theta, \phi)$, the geographical continent-ocean pattern. The line marked "combined" in Figure 13 is the linear combination in brackets defined in (10) for $s = 2$ and has a sign opposite to the Moho kernel because of the negative sign multiplying the Moho kernel in (10). The topographic kernels for degrees $s > 2$ are very similar to those for $s = 2$.

The Harvard and the Scripps crustal models were carefully constructed, so we consider the difference in the computed crustal structure coefficients to be a realistic estimate of the errors in our knowledge of crustal structure. Discussion of the implications of the differences in the crustal models is delayed until section 7.1.

5. MODEL PREDICTIONS AND FIT TO NORMAL MODE DATA

In this section we compare the observed normal mode structure coefficients with those computed from each of the three dimensional models considered here. In section 5.1 we add to the computed volumetric structure coefficients for each model the crustal and Coriolis-coupling structure coefficients so that the observed and predicted normal mode structure coefficients can be compared directly. In section 5.2 the geographical splitting functions computed from each of the models are compared with the observed splitting functions.

This is the most technical section of the paper. The reader who wishes to skip some of the technical details should proceed to section 6 for a summary of the results through this section.

5.1. Comparison of Model Predictions With Normal Mode Structure Coefficients

The observed normal mode structure coefficients used in the following were obtained from several sources: those for low-degree fundamental and overtone modes are obtained from *Ritzwoller et al.* [1988] (ignoring the 10 anomalously split multiplets which are primarily sensitive to core structure), and those for the surface wave multiplets ${}_0S_8$–${}_0S_{52}$ are taken from *Smith and Masters* [1989a]. The multiplets ${}_0S_{11}$, ${}_0S_{18}$, and ${}_0S_{19}$ are excluded from this range owing to profound

TABLE 4. The χ^2 Measures of Misfit: Fundamental Mode Branch, $n = 0$, $s = 2$, $K = 46$ data points

Model	$\chi^2(c_2^0)$	$\chi^2(Re\ c_2^1)$	$\chi^2(Im\ c_2^1)$	$\chi^2(Re\ c_2^2)$	$\chi^2(Im\ c_2^2)$	$\Sigma\ \chi^2/5K^*$
S12_WM13	1709.0	97.8	129.7	193.4	496.7	11.4
SH.10c.17	381.6	98.4	61.2	124.2	212.4	3.8
M84C + LO2.56	1123.3	107.4	1225.1	302.0	1399.2	18.1
MDLSH	1621.3	1236.7	1035.4	1318.0	3097.1	36.12

*The quantity $\Sigma\ \chi^2$ denotes the χ^2 (equation (11)) for all $(2s + 1) * K$ observed structure coefficients on a given branch and fixed degree s, where K is the number of normal modes analyzed along the branch. The azimuthal orders included in the sum lie in the range $0 \leq t \leq s$.

Coriolis coupling. Both sets of coefficients provide constraints only on the even degree part of the spectrum of heterogeneity.

To interpret the misfit observed in Figures 14–16, it is useful to note that the fundamental mode structure coefficients become increasingly sensitive to structures near to the surface of the Earth as harmonic degree l of the multiplet is increased. Fundamental modes with $5 < l < 20$ are dominantly sensitive to the lower mantle, those with $20 < l < 35$ are dominantly sensitive to the top of the lower mantle and the Transition Zone, and those with $35 < l < 52$ possess predominant sensitivity to the upper mantle. The structure coefficients for multiplets along the first, second, and fifth overtone branches are sensitive mainly to lower mantle structures.

To quantify the misfit, the χ^2 statistic is introduced, which is defined as follows:

$$\chi^2(c_s^t) = \sum_{k=1}^{K} \left[\frac{{}_kc_s^t - {}_k\bar{c}_s^t}{{}_k\sigma_s^t} \right]^2, \qquad (11)$$

where ${}_kc_s^t$ is the observed structure coefficient, ${}_k\bar{c}_s^t$ is the predicted coefficient value of ${}_kc_s^t$ for a given model, ${}_k\sigma_s^t$ is the uncertainty estimated for ${}_kc_s^t$, and K is the number of coefficients. We define ${}_k\bar{c}_s^t$ as the sum of the mantle, crustal, and Coriolis structure coefficients. Tables 4–8 present χ^2 statistics for each of the models considered here, categorized by data type and degree of aspherical structure.

For each degree and order (s, t), an optimal fit would require that $\chi^2 \sim K$, in which case a model would neither underfit nor overfit the data, predicting structure coefficients, on average, approximately 1σ from the observed coefficients. Fits combined across the $2s + 1$ orders for a degree of structure should also be divided by the number of orders, as follows: $\chi^2/K(2s + 1)$. If this statistic were equal to, say, 1, 4, or 9, then the structure coefficients would be misfit on average by 1σ, 2σ, or 3σ. For example, as can be seen in Table 4, the χ^2 value for model S12_WM13 for the fundamental mode structure coefficient Re c_2^2 is 193. Since the number of fundamental modes used to compute this statistic is $K = 46$, $\chi^2/K = 4.2$, the average misfit of the Re c_2^2 structure coefficient along this branch is approximately 2.1σ. Across all $2s + 1 = 5$, degree $s = 2$ coefficients, $\chi^2/K(2s + 1) = 11.4$; i.e., the average misfit of the degree 2 structure coefficients along the fundamental mode branch is approximately 3.4σ. This poor fit is caused predominantly by the misfit in the c_2^0 coefficients which, on average, is at the 6σ level.

5.1.1. Fit to degree 2 fundamental mode structure coefficients. Figure 14a displays the observed degree 2 structure coefficients along the fundamental mode branch as well as the coefficients computed for the Harvard models S12_WM13 and M84C + LO2.56. The analogous plots for the models SH.10c.17 and MDLSH are shown in Figure 14b, and misfit statistics are compiled in Table 4, where it can be seen that the predicted degree 2 structure coefficients for SH.10c.17, S12_WM13, M84C + LO2.56, and MDLSH fit the observed coefficients along the fundamental mode branch, on average, at the 1.9σ, 3.4σ, 4.2σ, and 6σ levels, respectively.

With the exception of the c_2^0 coefficient, S12_WM13 fits the normal mode structure coefficients somewhat better than M84C + LO2.56. Both models fit the low-degree ($l < 10$) c_2^0 coefficients very well. Perhaps the most glaring fact revealed in Figure 14a is that both models badly misfit the c_2^0 coefficients in the zone of strong Coriolis coupling ($10 \leq l \leq 20$), presumably since neither model employed normal mode data with $l < 20$. These multiplets are dominantly sensitive to lower mantle structure. At higher degrees ($l \geq 20$) the fit of M84C + LO2.56 to the observed c_2^0 coefficients is much better than that of S12_WM13. Both S12_WM13 and M84C + LO2.56 fit aspects of the data poorly in the range $20 \leq l \leq 30$ in which multiplets are sensitive to structure in the top of the lower mantle and in the Transition Zone. Errors in LO2.56 near the top of the lower mantle, perhaps due to poor sampling in this region by P waves, probably account for this discrepancy for M84C + LO2.56. Some of this misfit may be attributable to topography on the 400- and 660-km boundaries. This is discussed further in section 7.3.

A comparison of Figures 14a and 14b and inspection of Table 4 demonstrates that SH.10c.17 offers the best fit to the structure coefficients. This is not surprising, since *Masters et al.* [1992] included the structure coefficient data set in the construction of this model. Of course, the higher-degree structure coefficients along

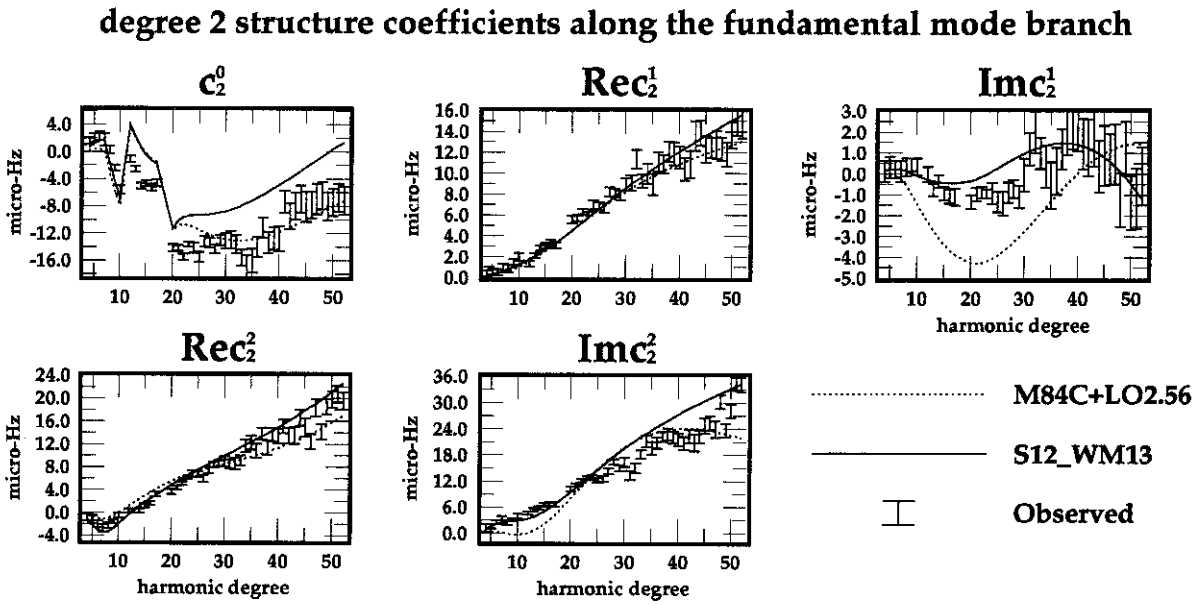

Figure 14a. Forty-six observed degree 2 structure coefficients (in units of microhertz) and estimated errors along the fundamental mode branch from *Smith and Masters* [1989] and those computed for the volumetric models S12_WM13 (solid line) and M84C + LO2.56 (dotted line). The predicted coefficients have been corrected to account for Coriolis coupling and to incorporate the effects of the Harvard crustal model. The degree 2 χ^2 measures of misfit are listed in Table 4.

the fundamental mode branch are Rayleigh-wave-equivalent modes, and since Rayleigh waves between and 7 mHz were used in constructing S12_WM13 and M84C, it is also not surprising that the predicted high-degree coefficients of these models agree well with the observations.

Figure 14b and Table 3 reveal that the fit of MDLSH to the observed degree 2 fundamental mode structure coefficients is much worse than that of the other models. Because the degree 2 misfit increases with harmonic degree, MDLSH is probably relatively more accurate in geographical distribution of heterogeneity in the lower mantle than in the upper mantle. MDLSH is only about one third larger than SH.10c.17 in rms amplitude above the Transition Zone, and the geographical correlation of MDLSH with SH.10c.17 above the Transition Zone is rather poor. Consequently, it is likely that the divergence of the predic-

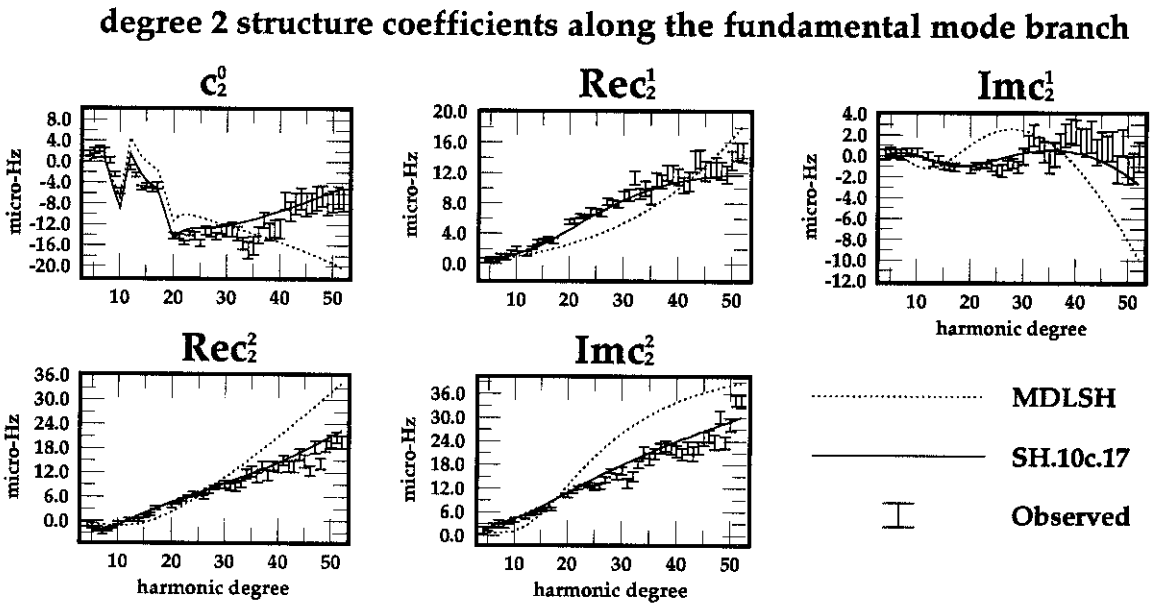

Figure 14b. Same as Figure 14a, but for the volumetric model SH.10c.17 (solid line) with the Scripps crustal correction and for the model MDLSH (dotted line).

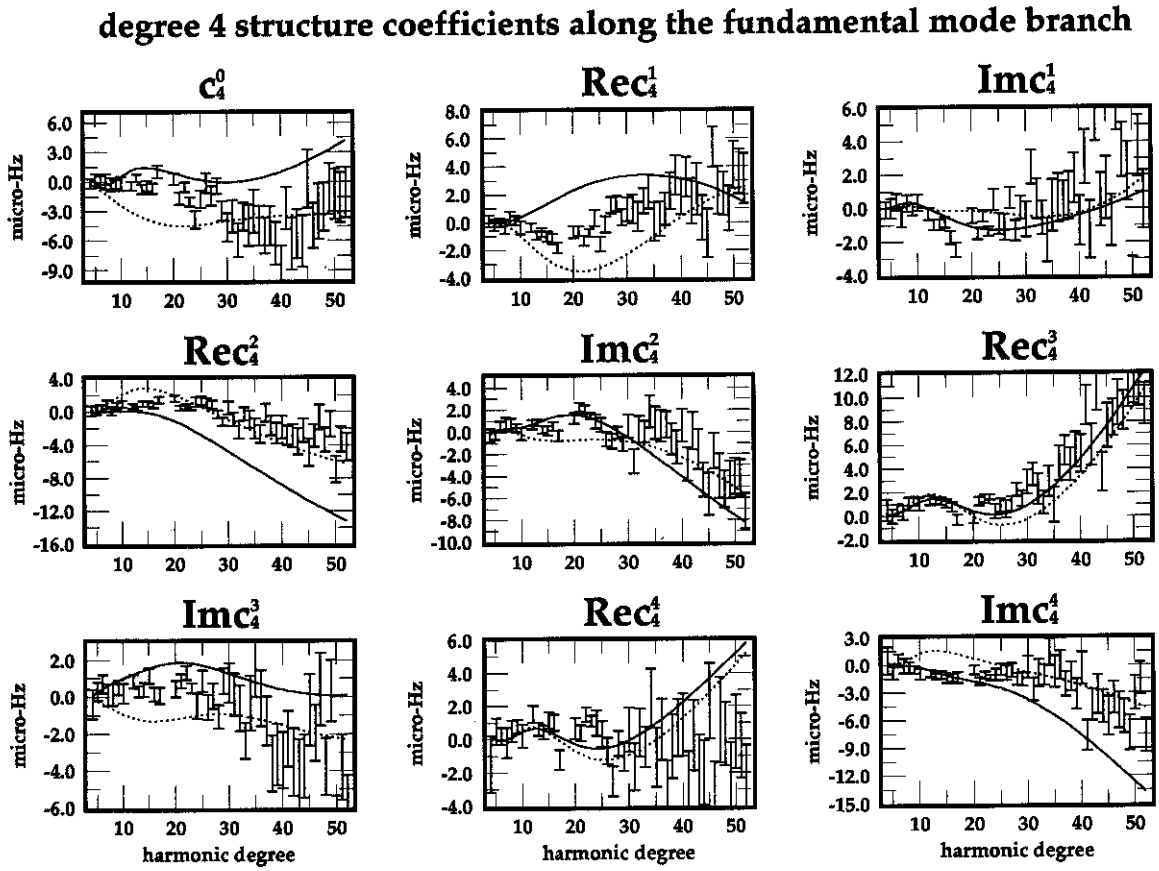

Figure 15a. Forty-six observed degree 4 structure coefficients (in units of microhertz) and estimated errors along the fundamental mode branch from *Smith and Masters* [1989] and those computed for the volumetric models S12_WM13 (solid line) and M84C + LO2.56 (dotted line). The predicted coefficients have been corrected using the Harvard crustal model. The degree 4 χ^2 measures of misfit are listed in Table 5.

tions of MDLSH from the data at high l is due mostly to differences in the distribution of heterogeneity, perhaps both geographically and in radius, rather than amplitude or scaling problems. This is probably because Rayleigh waves were not used in the construction of MDLSH.

5.1.2. Fit to higher-degree fundamental mode structure coefficients. Figure 15a displays the observed degree 4 structure coefficients along the fundamental mode branch as well as the coefficients computed for the Harvard models S12_WM13 and M84C + LO2.56, and Figure 15b shows the analogous plots for the models SH.10c.17 and MDLSH. The misfit statistics in Table 5 demonstrate that the predicted degree 4 structure coefficients for SH.10c.17, S12_WM13, M84C + LO2.56, and MDLSH fit the observed degree 4 coefficients along the fundamental mode branch, on average, at the 1.6σ, 3.0σ, 2.8σ, and 4.8σ levels, respectively.

S12_WM13 tends to fit the observed coefficients at low harmonic degrees l better than M84C + LO2.56, suggesting that the degree 4 lower mantle structure is better modeled by S12_WM13 than LO2.56. However, the structure coefficients of the higher-degree modes appear to be better modeled by M84C, except for the coefficients Im c_4^1, Im c_4^2, Re c_4^3, and Re c_4^4 which the two models fit nearly equally. Figure 15b displays the degree 4 fundamental mode structure coefficients computed using the models SH.10c.17 and MDLSH. SH.10c.17 fits the degree 4 coefficients very well, although there is some systematic misfit at high degrees for Re c_4^2 and Im c_4^4. MDLSH misfits the high l coefficients systematically with fits, again, degrading with harmonic degree, indicating inconsistency with the normal mode data sensitive to the upper mantle.

The geographical correlation of SH.10c.17 and S12_WM13 at degree 4 is high in the upper mantle, averaging ~0.9 above the Transition Zone, but the rms amplitude of SH.10c.17 at this degree of structure is systematically lower than that of S12_WM13. In all probability it is the amplitude rather than geographical distribution of heterogeneity that is the reason for the better fit of SH.10c.17 to the data than S12_WM13. This is also discussed further in section 7.3.

Misfit plots such as those in Figures 15a and 15b for structural degrees above 4 are not practical, but misfit statistics for degrees 6 and 8 relative to the fundamental mode structure coefficients are listed in Table 6.

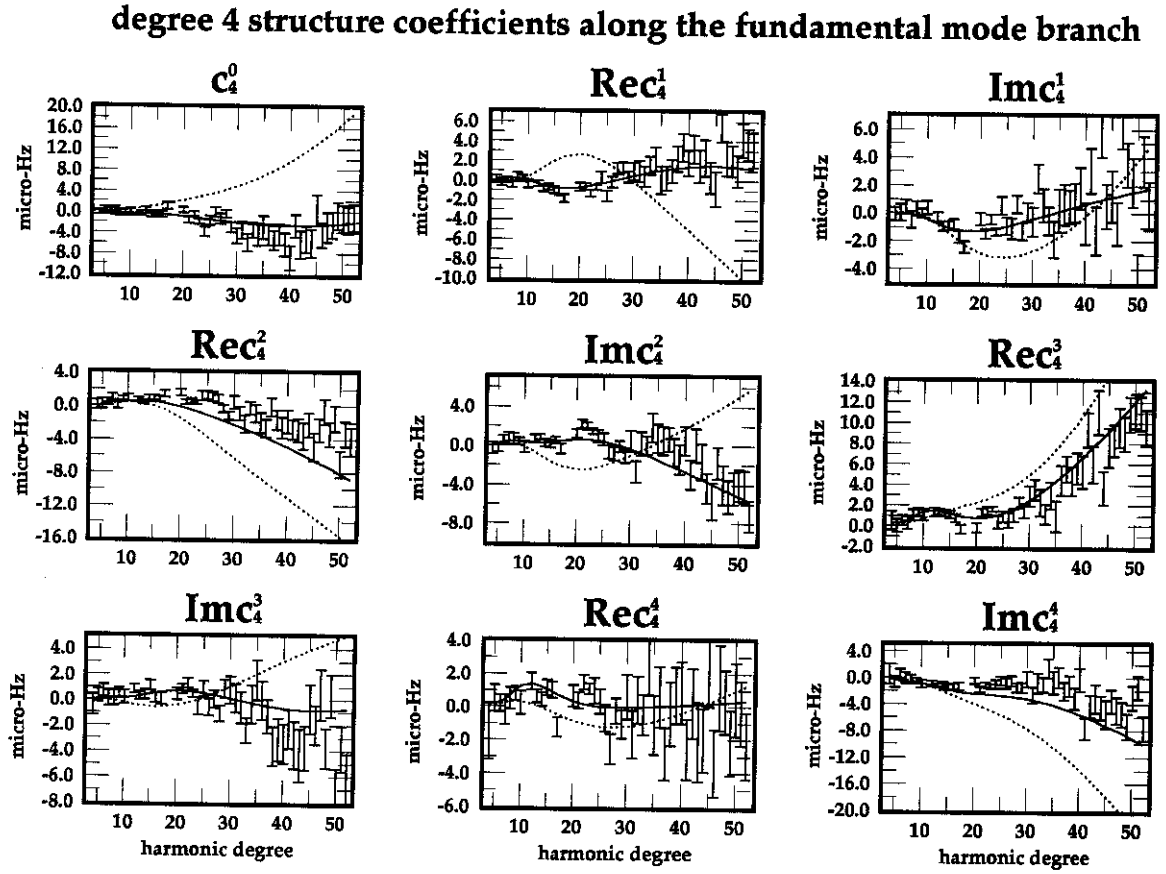

Figure 15b. Same as Figures 14b and 15a, but for degree 4 for the volumetric model SH.10c.17 (solid line) with the Scripps crustal correction and for the model MDLSH (dotted line).

These statistics demonstrate that the predicted degrees 6 and 8 structure coefficients for SH.10c.17, S12_WM13, M84C + LO2.56, and MDLSH fit the observed coefficients along the fundamental mode branch, on average, at the 1.4σ and 1.2σ, 2.3σ and 2.2σ, 2.5σ and 2.0σ, and 4.5σ levels, respectively. (Only a degree 6 average misfit is reported for MDLSH, since it does not possess a degree 8 component.) The reported fit to the degree 6 and 8 data is better than the relative fit at degrees 2 and 4, largely because the relative errors at degrees 6 and 8 are larger than those at degrees 2 and 4. At degrees 6 and 8, SH.10c.17 again fits the data better than the other models. S12_WM13 and M84C + LO2.56 fit the degree 6 and 8 coefficients overall at about the same level. The fine structure of misfit for each model differs, however. MDLSH fits the degree 6 coefficients much more poorly than the other models, consistent with the results at degrees 2 and 4.

5.1.3. Fit to overtone structure coefficients. The majority of the structure coefficients considered so far have been for surface wave multiplets which are dominantly sensitive to upper mantle structure. Consideration of multiplets along the first few overtone branches yields complementary information about the lower mantle. Figures 16a to 16c display the degree 2, nonanomalously split overtone structure coefficients estimated by *Ritzwoller et al.* [1988] and the coefficients predicted by the models S12_WM13, M84C + LO2.56, SH.10c.17, and MDLSH. The χ^2 measures of misfit are listed in Tables 7–9. At degree 4 the models SH.10c.17, S12_WM13, M84C + LO2.56, and

TABLE 5. The χ^2 Measures of Misfit: Fundamental Mode Branch, $n = 0$, $s = 4$, $K = 46$ data points

Model	$\chi^2(c_4^0)$	$\chi^2(Re\ c_4^1)$	$\chi^2(Im\ c_4^1)$	$\chi^2(Re\ c_4^2)$	$\chi^2(Im\ c_4^2)$	$\chi^2(Re\ c_4^3)$	$\chi^2(Im\ c_4^3)$	$\chi^2(Re\ c_4^4)$	$\chi^2(Im\ c_4^4)$	$\Sigma\ \chi^2/9K^*$
S12_WM13	314.8	948.9	133.2	1330.9	134.3	121.0	237.1	176.2	339.6	9.0
SH.10c.17	69.6	59.8	89.8	317.1	96.3	70.9	80.9	72.3	229.7	2.6
M84C + LO2.56	598.2	671.1	165.8	339.9	294.8	285.4	320.3	193.9	412.7	7.9
MDLSH	1486.1	1563.6	384.5	2222.7	1014.9	581.2	398.7	159.8	1974.7	23.6

*$\Sigma\ \chi^2$ is explained in the footnote to Table 4.

TABLE 6. The χ^2 Measures of Misfit: Fundamental Mode Branch; $n = 0$; $s = 6, 8$; $K = 46$ data points

Coefficient	*S12_WM13*	*SH.10c.17*	*M84C + LO2.56*	*MDLSH*
		Degree s = 6		
$\chi^2(c_6^0)$	176.1	78.8	460.4	132.8
$\chi^2(\text{Re } c_6^1)$	148.3	101.4	847.2	335.8
$\chi^2(\text{Im } c_6^1)$	141.7	73.0	218.3	129.9
$\chi^2(\text{Re } c_6^2)$	512.3	83.7	116.0	2282.7
$\chi^2(\text{Im } c_6^2)$	140.3	82.7	54.5	245.2
$\chi^2(\text{Re } c_6^3)$	61.7	51.1	170.5	300.7
$\chi^2(\text{Im } c_6^3)$	438.6	165.5	105.6	1107.2
$\chi^2(\text{Re } c_6^4)$	96.1	100.4	102.1	662.9
$\chi^2(\text{Im } c_6^4)$	107.8	49.2	81.1	619.7
$\chi^2(\text{Re } c_6^5)$	459.0	87.0	657.2	1508.6
$\chi^2(\text{Im } c_6^5)$	188.0	50.9	315.9	2352.8
$\chi^2(\text{Re } c_6^6)$	172.0	78.0	119.3	1247.0
$\chi^2(\text{Im } c_6^6)$	277.8	92.8	93.4	318.0
$\Sigma\ \chi^2/13K^*$	5.3	2.0	6.1	20.6
		Degree s = 8		
$\chi^2(c_8^0)$	235.0	74.3	92.8	N.A.
$\chi^2(\text{Re } c_8^1)$	170.4	51.7	72.7	N.A.
$\chi^2(\text{Im } c_8^1)$	140.9	52.4	63.7	N.A.
$\chi^2(\text{Re } c_8^2)$	308.2	96.6	317.0	N.A.
$\chi^2(\text{Im } c_8^2)$	139.6	65.5	70.3	N.A.
$\chi^2(\text{Re } c_8^3)$	301.6	53.7	192.0	N.A.
$\chi^2(\text{Im } c_8^3)$	117.0	74.2	117.0	N.A.
$\chi^2(\text{Re } c_8^4)$	158.7	79.2	76.7	N.A.
$\chi^2(\text{Im } c_8^4)$	55.7	62.5	263.9	N.A.
$\chi^2(\text{Re } c_8^5)$	72.6	39.3	230.7	N.A.
$\chi^2(\text{Im } c_8^5)$	291.4	44.3	120.2	N.A.
$\chi^2(\text{Re } c_8^6)$	292.7	63.9	469.8	N.A.
$\chi^2(\text{Im } c_8^6)$	119.3	48.4	128.2	N.A.
$\chi^2(\text{Re } c_8^7)$	505.1	84.8	120.3	N.A.
$\chi^2(\text{Im } c_8^7)$	166.2	39.2	346.6	N.A.
$\chi^2(\text{Re } c_8^8)$	112.63	44.4	78.0	N.A.
$\chi^2(\text{Im } c_8^8)$	87.2	56.2	72.1	N.A.
$\Sigma\ \chi^2/17K^*$	4.7	1.4	4.0	N.A.

N.A., not applicable.
*$\Sigma\ \chi^2$ is explained in the footnote to Table 4.

MDLSH agree relatively well with one another and with the data. This is due to large uncertainty estimates in the degree 4 coefficients, and we will discuss these coefficients no further.

For the first-overtone branch ($_1S$) shown in Figure 16a, the c_2^0 coefficients are fit the most poorly. The models S12_WM13 and SH.10c.17 fit the remaining coefficients approximately equally well. S12_WM13 fits the first-overtone structure coefficients remarkably well, especially considering that they were not used in the construction of the model. The $_1S$ multiplets are dominantly sensitive to δv_s variations in the lower mantle. The misfit of LO2.56 to the c_2^2 coefficients can be understood by the fact that it is fundamentally a v_p model, as is discussed further in section 7.2. The misfit of MDLSH is due to the fact that its amplitude is smaller in the lowermost mantle than the other models.

Figure 16b displays the second-overtone coefficients ($_2S$). With the exception of the c_2^0 coefficients, the coefficients are equally well fit by SH.10c.17 and S12_WM13. The predictions of MDLSH and M84C + LO2.56 are comparable, but their fit to the data is inferior to the fit by the other two models.

Figure 16c displays observed structure coefficients and model predictions for degree 2 coefficients along the fifth-overtone branch ($_5S$). These coefficients are fit best by M84C + LO2.56 and MDLSH. As is discussed in section 7.2, the fits to these coefficients are dominated by the choice of the scaling coefficient, $dlnv_s/dlnv_p$, and none of the models fits all the coefficients along this branch well. Since LO2.56 is a v_p model, its fit to these multiplets is largely decoupled from the choice of the scaling coefficient. SH.10c.17 and S12_WM13 use a scaling coefficient $dlnv_s/dlnv_p$ which is probably too small by about a factor of 1.5–2, and this results in their misfit to the structure coefficients for these multiplets. The superiority of the fit the $_5S$ coefficients by MDLSH over SH.10c.17 and S12_WM13 is really accidental. MDLSH is purely a δv_s model. The fact that there is no δv_p part means that for the $_5S$ multiplets the predicted structure coef-

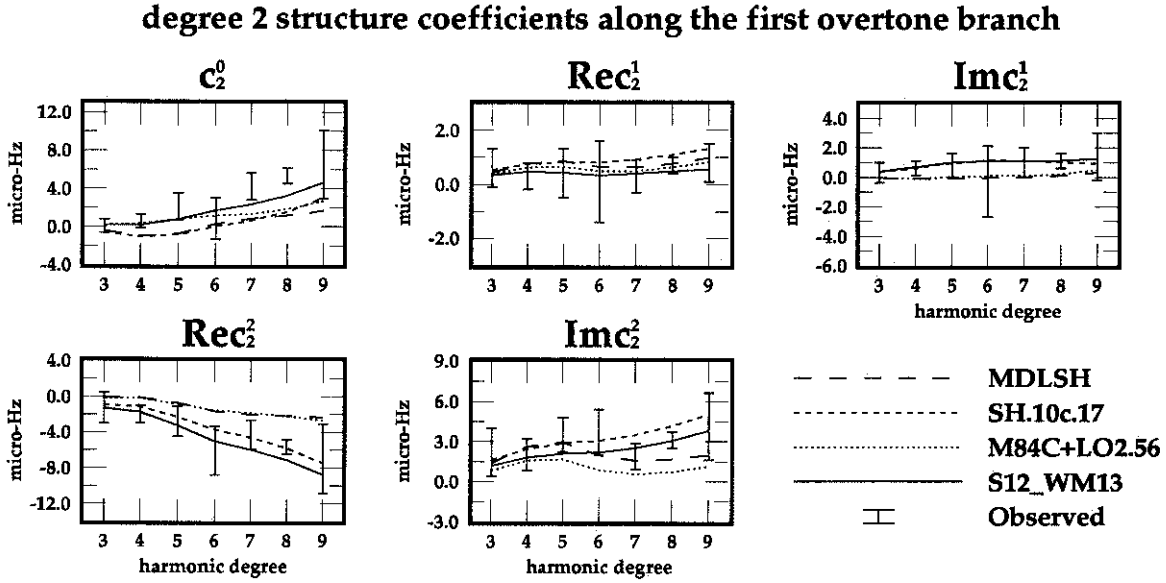

Figure 16a. Seven observed degree 2 structure coefficients (in units of microhertz) and estimated errors along the first-overtone branch from *Ritzwoller et al.* [1988] and those computed from the volumetric models S12_WM13 (solid line), SH.10c.17 (short-dashed line), M84C + LO2.56 (dotted line), and MDLSH (long-dashed line). The computed coefficients were corrected with the appropriate crustal model. The first-overtone, degree 2 χ^2 measures of misfit are listed in Table 7.

ficients are guaranteed to be extremely small and more in accord with the observations. The addition of a ~~n~~listic lower mantle v_p model to MDLSH would grade the fit of MDLSH to these coefficients.

5.2. Comparison of Model Predictions With Normal Mode Splitting Functions

Analysis of misfit to structure coefficients does not discriminate if the source of the misfit is due to an amplitude error in the model or to a geographical difference. A useful complementary way of representing the structure coefficients to yield this information is by plotting splitting functions, which are defined by equation (9). From equation (7), each structure coefficient ${}_kc_s^t$ is an integral measure of aspherical Earth structure at degree s and order t in which the radial kernels depend on the radial eigenfunction shapes of multiplet k and on the values of the scaling relationships in Table 3. Therefore the splitting function is a radial projection of aspherical structure onto the

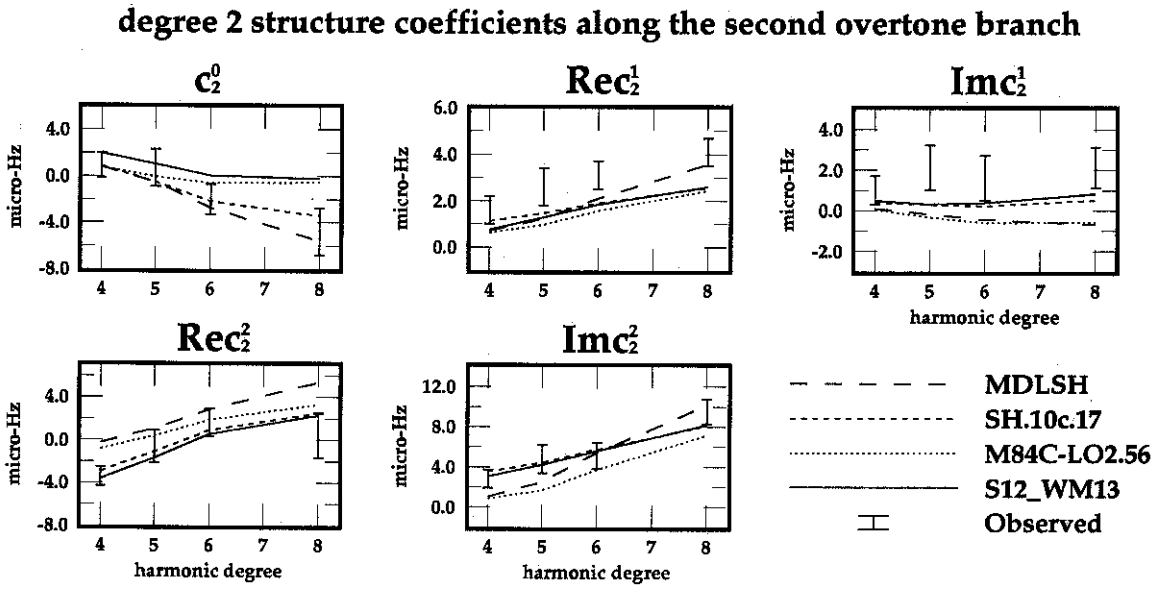

Figure 16b. Same as Figure 16a, but for the four observed degree 2 structure coefficients and estimated errors along the second-overtone branch. The second-overtone χ^2 measures of misfit are listed in Table 8.

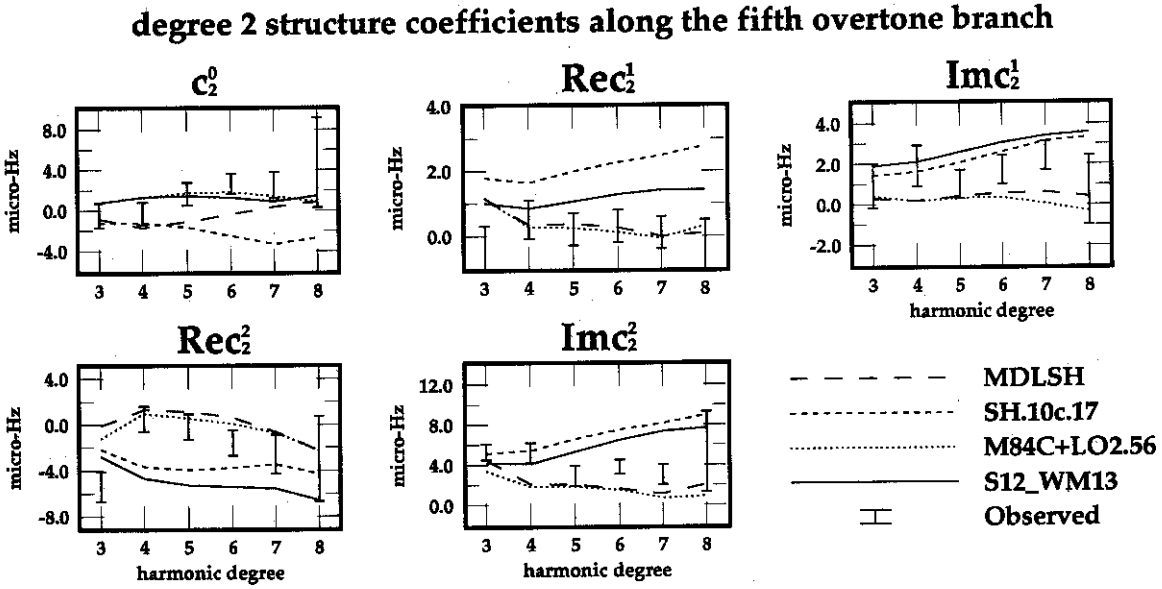

Figure 16c. Same as Figure 16a, but for the six observed degree 2 structure coefficients and estimated errors along the fifth-overtone branch. The fifth-overtone χ^2 measures of misfit are listed in Table 9.

Earth's surface, where the contribution of structure at each depth is weighted by the same integral kernel defined for the structure coefficient. The scaling relationships between v_s, v_p, and ρ affect the amplitude of the aspherical models much more strongly than their geographical pattern, so that comparison of splitting function patterns are mostly insensitive to the chosen values of the coefficients. Consequently, visual and statistical inspection of splitting functions potentially reveal geographical similarities and differences that are not revealed by the χ^2 misfit statistics discussed in section 5.1 and tabulated in Tables 4–10.

Figures 17a to 17d display the predicted splitting functions for each of the models S12_WM13, SH.10c.17, M84C + LO2.56, and MDLSH for the multiplets ${}_0S_8$, ${}_0S_{15}$, ${}_0S_{28}$, and ${}_0S_{50}$. These multiplets have their peak sensitivities in the lower mantle, top of the lower mantle, Transition Zone, and upper mantle, respectively. The appropriate crustal model and the effect of Coriolis coupling was included in the computation of these splitting functions in order to make them comparable to the splitting functions of the observed data, which are plotted in Figure 18. Only even degree components have been included, since odd order structure coefficients have not yet been estimated. In general, the predicted splitting functions for multiplets with harmonic degrees above $l = 20$ compare very favorably in geographical pattern with the observed splitting functions but can differ appreciably in peak-to-peak values of the associated frequency shift.

Figure 19a shows the degree correlation coefficients between the observed and each of the four model splitting functions. Correlations are observed to increase with the harmonic degree l of the multiplet and to decrease with degree of the structure. Clearly and not surprisingly, the degree 2 model structure coefficients are correlated much more highly with the observed structure coefficients than are the higher-degree coefficients due to their size and the strength of their effect on the data. The 90% confidence levels are exceeded by each of the models at degree 2 for all multiplets with $l \geq 15$. Only SH.10c.17, which was the only model that utilized low-frequency fundamental modes with $l < 20$ that were corrected for the effects of the Coriolis force, is uniformly correlated with the observed splitting functions at levels above 90% for all l. M84C + LO2.56 possesses the lowest correlations below $l = 20$ for degree $s = 2$, presumably due to errors in the upper part of the lower mantle in LO2.56.

TABLE 7. The χ^2 Measures of Misfit: First Overtone Branch; $n = 1$; $s = 2$; $3 \leq l \leq 9$; $K = 7$ data points

Model	$\chi^2(c_2^0)$	$\chi^2(Re\ c_2^1)$	$\chi^2(Im\ c_2^1)$	$\chi^2(Re\ c_2^2)$	$\chi^2(Im\ c_2^2)$	$\Sigma\ \chi^2/5K^*$
S12_WM13	10.0	0.9	0.5	4.9	2.7	0..
SH.10c.17	39.9	4.7	0.5	1.7	6.4	1..
M84C + LO2.56	25.0	0.8	7.7	30.3	24.5	2.5
MDLSH	43.5	1.9	9.0	31.0	8.1	2.7

*$\Sigma\ \chi^2$ is explained in the footnote to Table 4.

TABLE 8. The χ^2 Measures of Misfit: Second Overtone Branch; $n = 2$; $s = 2$; $l = (4, 5, 6, 8)$; $K = 4$ data points

Model	$\chi^2(c_2^0)$	$\chi^2(Re\ c_2^1)$	$\chi^2(Im\ c_2^1)$	$\chi^2(Re\ c_2^2)$	$\chi^2(Im\ c_2^2)$	$\Sigma\ \chi^2/5K^*$
S12_WM13	8.7	15.1	6.9	2.0	1.5	1.7
SH.10c.17	1.0	13.1	7.7	1.7	2.3	1.3
M84C + LO2.56	5.9	20.9	18.1	10.4	14.6	3.5
MDLSH	1.0	8.6	17.1	20.2	6.8	2.7

*$\Sigma\ \chi^2$ is explained in the footnote to Table 4.

However, the splitting functions for M84C + LO2.56 are on average correlated above the 90% level with the observed degree 2 splitting functions for $l \geq 20$, which are the multiplets sensitive predominantly to the upper mantle. The fit at degree $s = 4$ of this model is particularly impressive. Except for $s = 4$ structure, S12_WM13 splitting functions are correlated above 90% for all multiplets with $l \geq 15$. Splitting functions computed from MDLSH are in general lower than those for the other models, but they are still high in an absolute sense. Total correlations are displayed in Figure 19b. The splitting functions for SH.10c.17 are in best agreement with the data. The average correlations $\bar{\rho}_c$ of multiplets in the range $20 \leq l \leq 52$ in descending order are given by $\bar{\rho}_c \sim 0.93$ for SH.10c.17, $\bar{\rho}_c \sim 0.89$ for M84C + LO2.56, $\bar{\rho}_c \sim 0.85$ for S12_WM13, and $\bar{\rho}_c \sim 0.75$ for MDLSH.

The amplitudes of the splitting functions are displayed in Figures 20a and 20b as the ratio of the rms of the model splitting function over the rms of the observed splitting function. The rms ratios vary greatly between degrees, and in general the relationship between the model and data amplitudes is appreciably worse than the geographical relationship. The rms ratio for MDLSH grows with harmonic degree and is much larger than the other models owing to lack of a crustal correction. Since the fundamental model structure coefficients for the crustal correction are anticorrelated with mantle structure coefficients, the use of the crustal correction on average reduces the magnitude of the structure coefficients for all of the models but MDLSH.

The high values of $\bar{\rho}_c$ for all of the models for the high-degree multiplets reflect the geographical consistency of the volumetric structure of the models in the upper mantle. This, together with the amplitude discrepancies shown in Figures 20a and 20b, reveals that a significant fraction of the difference between the models is due to variations in their amplitudes and in the radial distribution of structure, rather than to the geographical differences.

6. SUMMARY OF MODEL COMPARISONS AND FITS TO THE NORMAL MODE DATA

For the reader who does not want to wade through all the technical details involved in the statistical comparison between the models and their fit to the normal mode structure coefficients contained in sections 3–5, we summarize some of the major results from those sections here. Discussion of the resolution of some of the observed discrepancies is deferred to section 7.

6.1. Geographical Correlation

The geographical correlations between the models are displayed in Figure 9. They are generally encouraging, and the 3-D models considered here apparently have constrained the geographical distribution of heterogeneity more accurately than either the radial distribution or the amplitude of structure. M84C, S12_WM13, and SH.10c.17 are highly correlated geographically (90% confidence level or higher) in the upper mantle and in the lowermost mantle below a depth of ~1800 km. MDLSH is generally more poorly correlated with the other models in the upper mantle and bottom one third of the lower mantle. Between 600 and 1800 km, in the region where the rms of each of the models is lowest, the average correlation between the models drops for individual degrees of structure and for the summation over all degrees. In particular, LO2.56 is uncorrelated with both S12_WM13 and SH.10c.17 in the top 700 km of the lower mantle at degree 2 and shows a lower correlation with the other models across all degrees in the top 500 km of the lower mantle. The discrepancy between LO2.56 and

TABLE 9. The χ^2 Measures of Misfit: Fifth Overtone Branch; $n = 5$; $s = 2$; $3 \leq l \leq 8$; $K = 6$ data points

Model	$\chi^2(c_2^0)$	$\chi^2(Re\ c_2^1)$	$\chi^2(Im\ c_2^1)$	$\chi^2(Re\ c_2^2)$	$\chi^2(Im\ c_2^2)$	$\Sigma\ \chi^2/5K^*$
2_WM13	7.1	21.3	14.5	63.5	42.7	5.0
ɔH.10c.17	58.9	72.1	7.7	36.6	68.6	8.1
M84C + LO2.56	5.3	6.1	19.8	14.3	35.4	2.7
MDLSH	20.1	5.8	13.0	23.7	25.1	2.9

*$\Sigma\ \chi^2$ is explained in the footnote to Table 4.

TABLE 10. The χ^2 Measures of Misfit: Fundamental Branch; $n = 0$; $2 \leq s \leq 8$; $20 \leq l \leq 35$; $K = 16$ data points

Model	$\chi^2(s = 2)$	$\chi^2(s = 4)$	$\chi^2(s = 6)$	$\chi^2(s = 8)$
S12_WM13	20.0	13.9	7.3	6.2
S12_WM13 + 660	15.9	11.2	6.7	6.3
SH.10c.17	4.1	3.9	2.5	1.4
SH.10c.17 + 660	8.0	5.3	2.4	1.4

the other models in the uppermost lower mantle also holds for the amplitude of the model, and we infer from this that LO2.56 is in error in this region, presumably as a result of poor sampling by P waves in the region. In fact, the biggest difference in the Harvard models S12_WM13 and M84C + LO2.56 after a decade of research lies in the top of the lower mantle.

These results point to the uppermost lower mantle

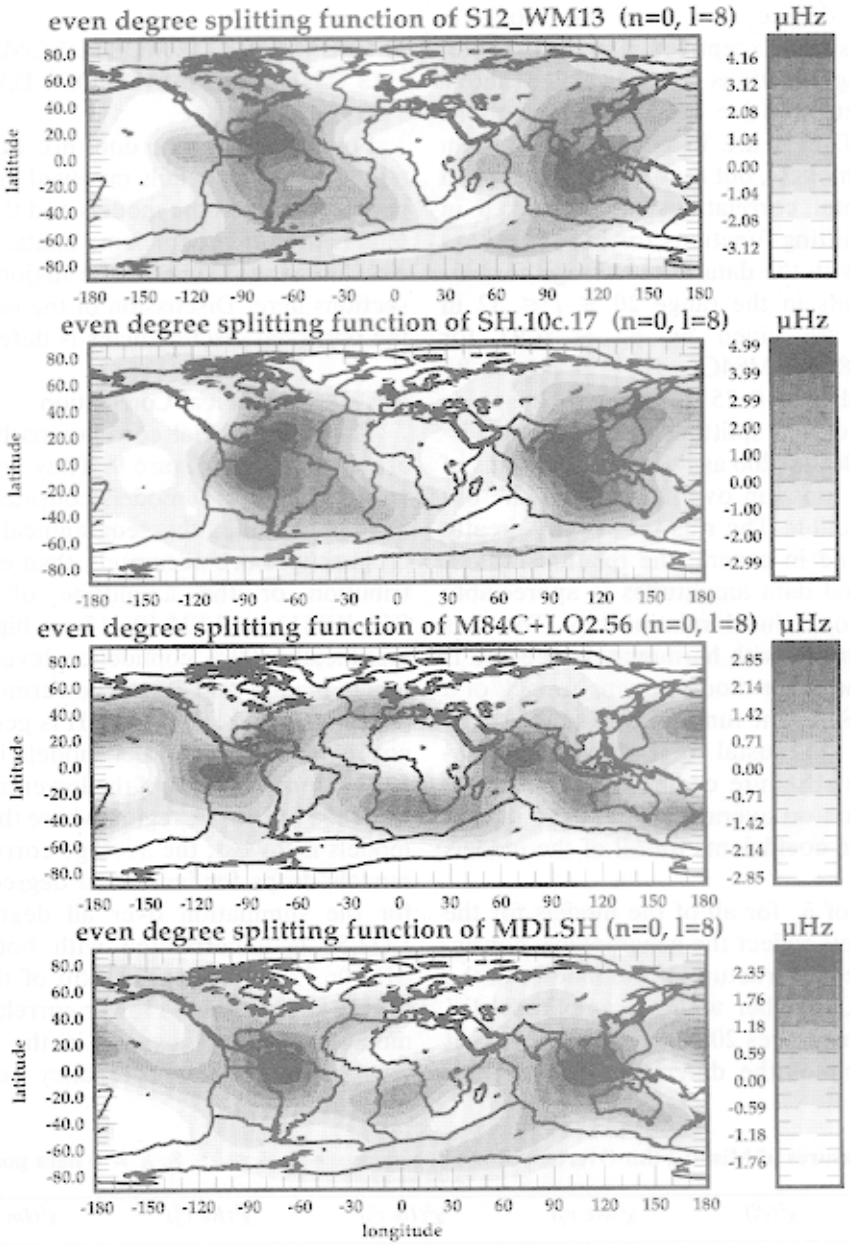

Figure 17a. Even degree 2–8 splitting functions (see equation (9)) for the multiplet ${}_0S_8$ computed from the models S12_WM13, SH.10c.17, M84C + LO2.56, and MDLSH with the Coriolis and appropriate crustal corrections. Units are in microhertz. Only even degrees are plotted to facilitate comparison with the observed splitting functions of Figure 18. Correlations between these splitting functions and the observed splitting function plotted in Figure 18 are 0.75, 0.63, 0.15, and 0.23, respectively.

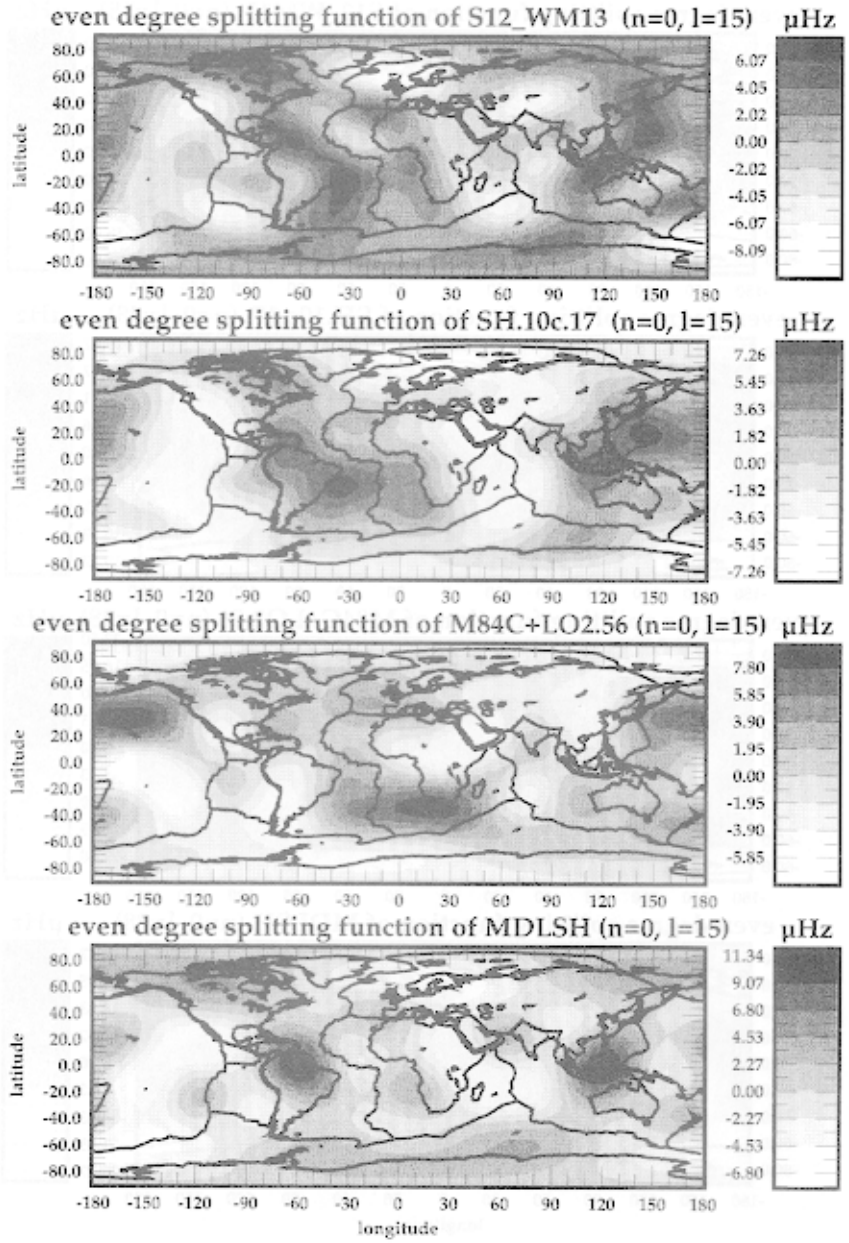

Figure 17b. Same as Figure 17a, but for the multiplet ${}_0S_{15}$. Correlations between these splitting functions and the observed splitting function plotted in Figure 18 are 0.61, 0.96, 0.40, and 0.47, respectively.

as a region deserving of focused future research. This is a problematic region, having relatively low rms structures while being relatively poorly sampled by globally propagating body waves. As is discussed in section 9.5, the use of long-period fundamental and overtone normal mode constraints is very important in resolving the structure in this region accurately.

6.2. Root-Mean-Square Characteristics

The rms amplitude distributions for each of the models, both as a function of radius and as a function of wavenumber, are displayed in Figures 6a, 6b, and 7. There is little variance in the degree spectrum of heterogeneity between the models. Consequently, there appears to be emerging agreement concerning both the distribution of heterogeneity with wavelength and the geographical distribution of heterogeneity. Heterogeneity tends to be peaked at certain characteristic wavelengths in boundary layers (degree 5 in the uppermost upper mantle; degree 2 in the Transition Zone and near the base of the mantle) and is approximately "white" in regions of bulk flow outside of these layers.

In contrast with the geographical correlation, the rms amplitude and the radial distribution of structure vary greatly between the models. For example, M84C (2.5% maximum) and S12_WM13 (1.3% maximum) possess the highest rms amplitudes in the uppermost mantle, where the rms amplitudes of SH.10c.17 (0.7% maximum) and MDLSH (0.95% maximum) are appreciably less. In addition, the choice of radial basis

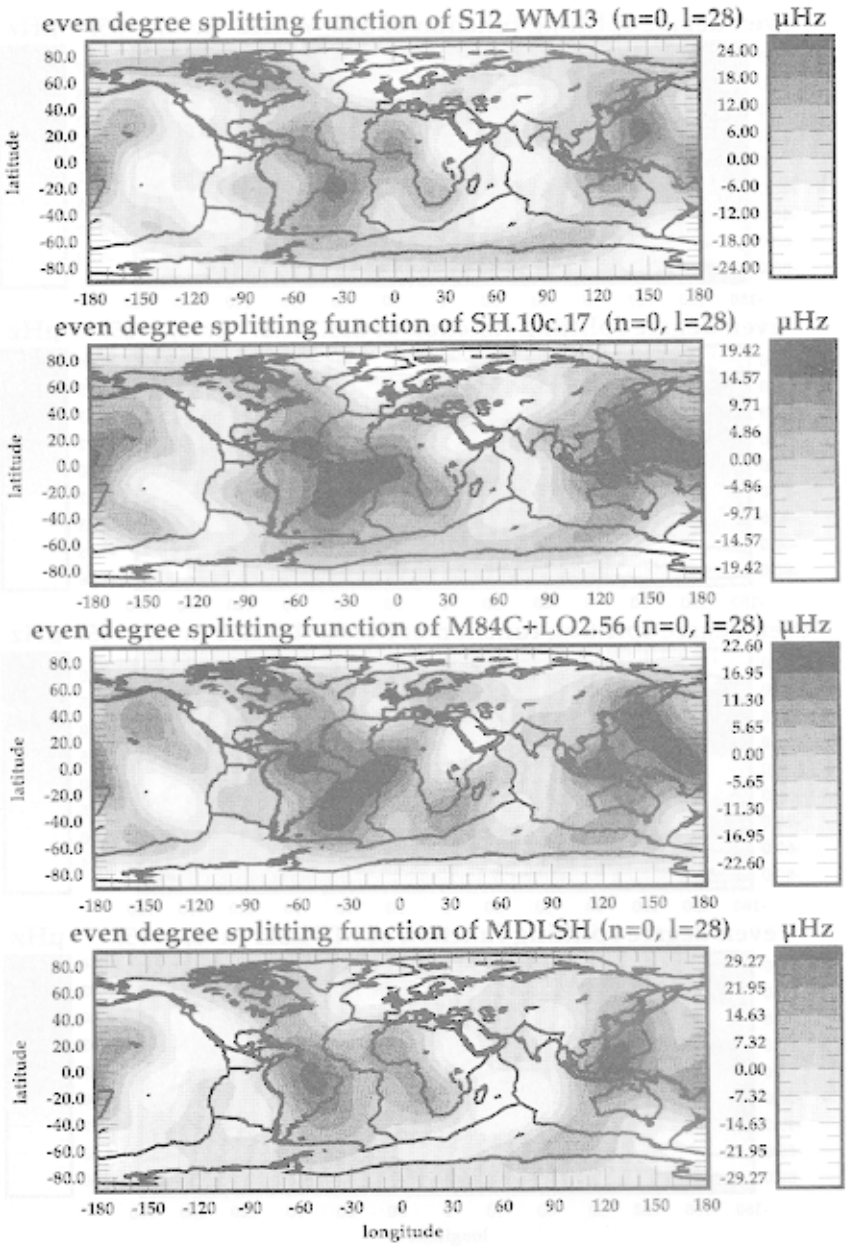

Figure 17c. Same as Figure 17a, but for the multiplet ${}_0S_{28}$. Correlations between these splitting functions and the observed splitting function plotted in Figure 18 are 0.88, 0.97, 0.85, and 0.80, respectively.

functions appears to affect the radial distribution of heterogeneity. The concentric shell radial basis functions of SH.10c.17 and MDLSH appear to smear heterogeneity more evenly across the upper mantle. As is discussed in section 7.1, approximately 50% of the amplitude discrepancy in the upper mantle is attributable to differences in the reference crustal models. The source of the other 50% discrepancy in rms is unclear; even the rms amplitudes of S12_WM13 and M84C differ by 50% through much of the Transition Zone, even though they employed the same crustal model.

The rms amplitudes of SH.10c.17 and MDLSH cross that of S12_WM13 near the base of the upper mantle, so that in contrast with the rms amplitudes in the upper mantle, near the top of the lower mantle the amplitudes of SH.10c.17 and MDLSH are greater than S12_WM13. LO2.56 concentrates heterogeneity near the boundaries of the lower mantle more than the other models, having a much higher rms amplitude than S12_WM13 at depths of 700 and 2800 km but a significantly lower amplitude near 2000-km depth in the center of the lower mantle. There is impressive similarity in the amplitudes of S12_WM13 and SH.10c.17 below 1800 km. Consistent with the geographical correlation results, the biggest difference in the Harvard models S12_WM13 and M84C + LO2.56 lies in the top of the lower mantle, where LO2.56 is 50% to 100% larger than S12_WM13.

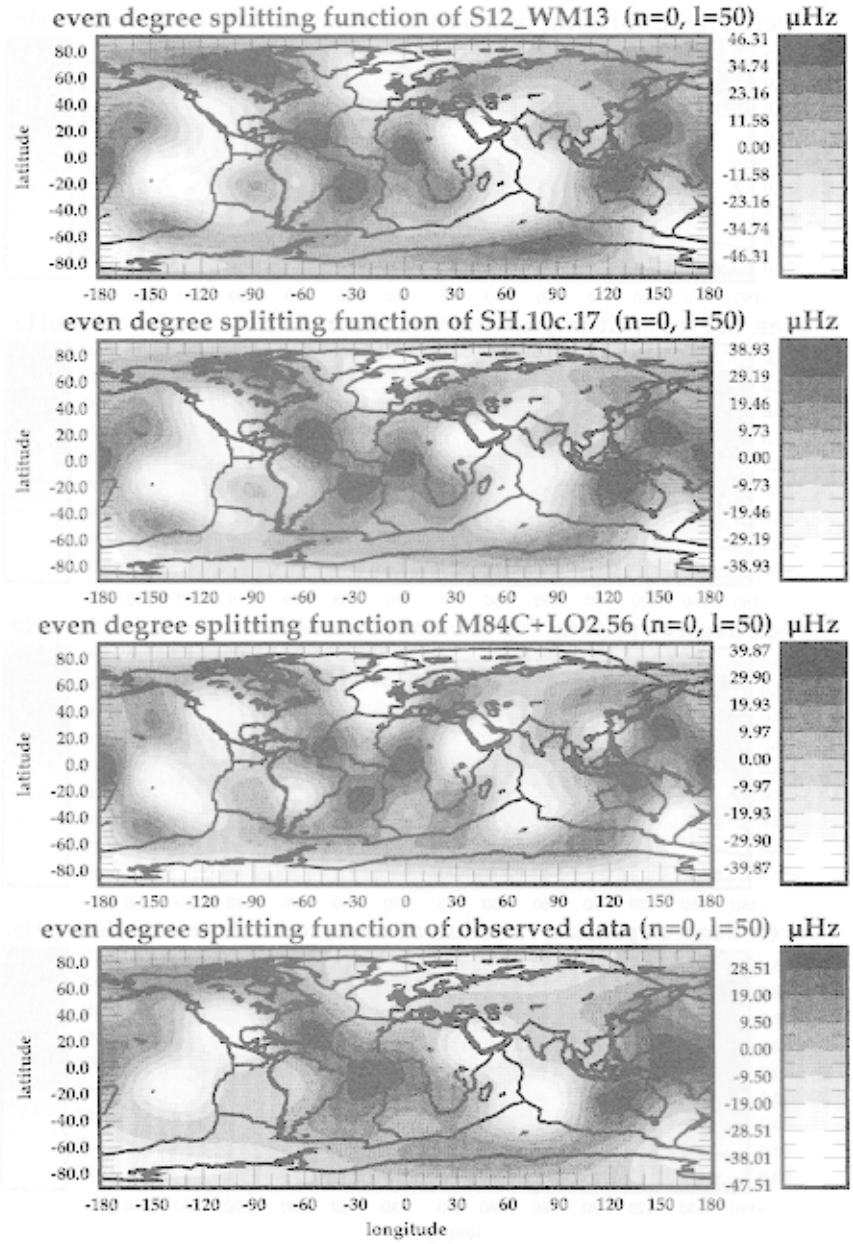

Figure 17d. Same as Figure 17a, but for the multiplet ${}_0S_{50}$. Correlations between these splitting functions and the observed splitting function plotted in Figure 18 are 0.88, 0.95, 0.87, and 0.73, respectively.

6.3. Radial Correlation

Radial correlation functions and correlation lengths for each of the models are displayed in Figures 10–12. Correlation lengths tend to increase with increasing depth for all of the models, from approximately 100–300 km in the upper mantle to 400–750 km near the base of the mantle. There is no evidence of a significant decorrelation across the 660-km boundary in S12_WM13 and SH.10c.17, and there is only weak evidence for MDLSH. Of course, there is an intrinsic discontinuity across this boundary for the combined model M84C + LO2.56. Each of the models except S12_WM13 appears to decorrelate across the radial level at approximately 1000-km depth. LO2.56 shows a significant local minimum in correlation length at approximately 2200-km depth. Further discussion of these observations and the problems involved with interpreting them is included in section 8.

6.4. Fit To Normal Mode Data

The fits of the predicted normal mode structure coefficients from each of the models to the observed fundamental and overtone structure coefficients (equation (7)) are shown in Figures 14–16, and χ^2 measures of misfit are tabulated in Tables 4–10. The χ^2 measures of misfit of model structure coefficients to the observed coefficients do not discriminate between errors in geographic pattern from errors in amplitude. Additional information is provided by considering normal

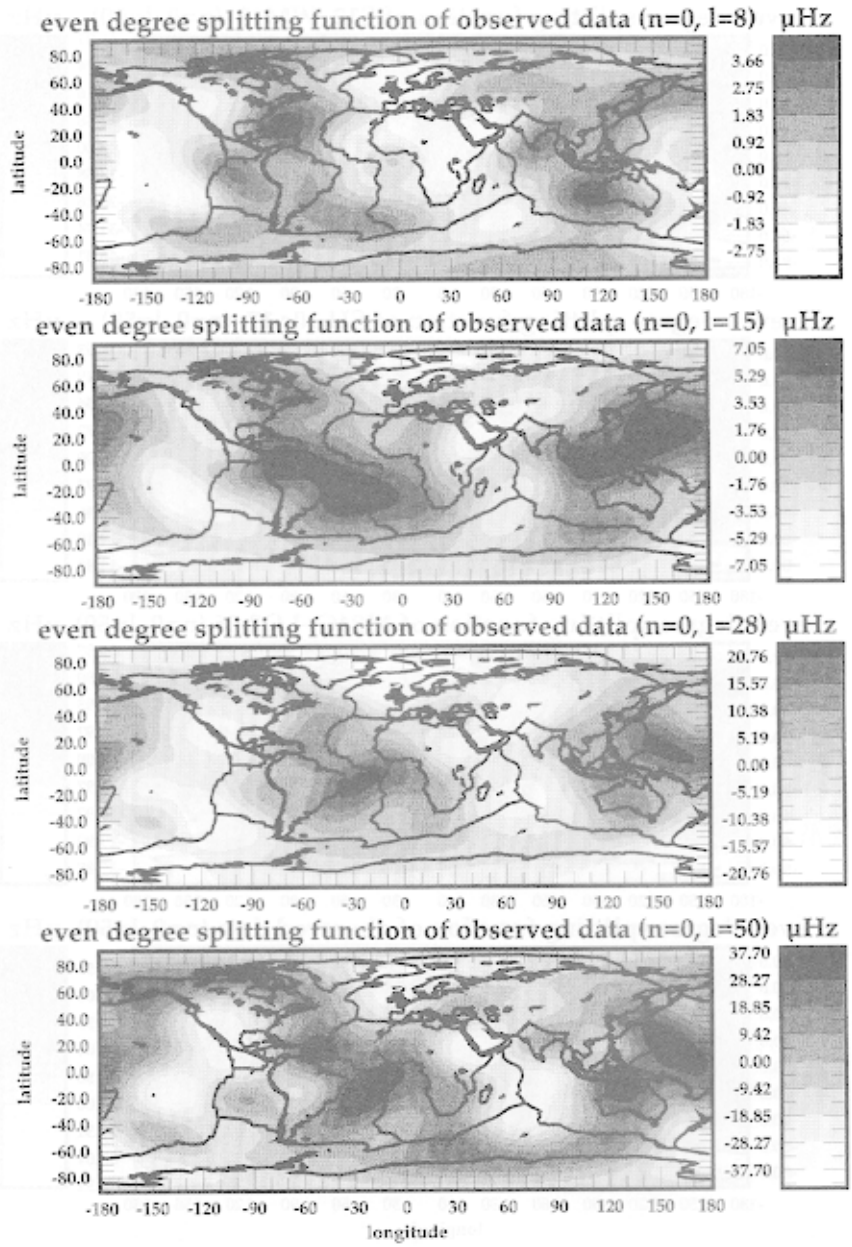

Figure 18. Observed splitting functions for ${}_0S_8$, ${}_0S_{15}$, ${}_0S_{28}$, and ${}_0S_{50}$ taken from *Smith and Masters* [1989]. (See equation (9).) Units are in microhertz.

mode splitting functions (equation (9)). Selected model splitting functions are plotted in Figures 17a to 17d and are compared with observed splitting functions in Figure 18. Correlations are shown in Figures 19a and 19b, and amplitudes are shown in Figure 20a and 20b.

As expected, SH.10c.17 fits the fundamental mode structure coefficients significantly better than the other models at all degrees of structure, but M84C + LO2.56 and S12_WM13 do fit these data quite well. An exception is the predicted c_2^0 coefficient of S12_WM13 which appears to be systematically different from the other models and from the observed fundamental mode structure coefficients sensitive to the upper mantle. This is probably not due to a normalization problem, since the overtone c_2^0 coefficients of S12_WM13 are not appreciably different from the other models'. Misfits of M84C + LO2.56 can be attributed to errors in LO2.56 near the top of the lower mantle.

M84C + LO2.56, S12_WM13, and MDLSH systematically misfit the fundamental mode structure coefficients with $9 < l < 21$, presumably because very low frequency Rayleigh or Love waves were not employed in their construction. These multiplets are highly sensitive to Transition Zone and lower mantle structures, as is discussed further in section 9.4. Both S12_WM13 and M84C + LO2.56 fit fundamental mode

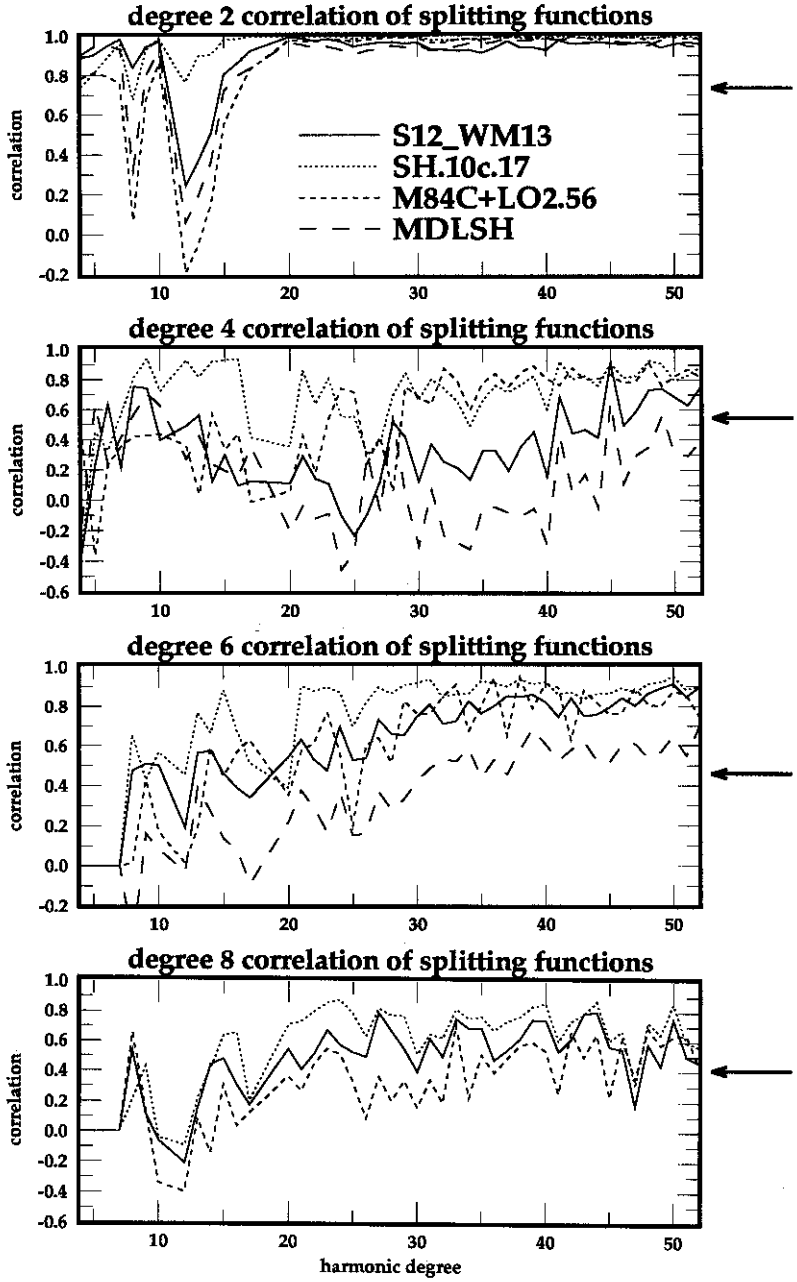

Figure 19a. Degree correlations between the observed splitting functions of *Smith and Masters* [1989] along the fundamental mode branch and splitting functions predicted from S12_WM13 (solid), SH.10c.17 (dotted), M84C + LO2.56 (short-dashed), and MDLSH (long-dashed) with the Coriolis and appropriate crustal corrections. The 90% confidence level is indicated with an arrow on the right of each panel.

data poorly in the range $20 \leq l \leq 30$ which overlaps the range of maximum modal sensitivity to the 660-km boundary. This is discussed further in section 7.3.

The models SH.10c.17 and S12_WM13 both fit the degree 2 overtone structure coefficients very well for $_1S$ and $_2S$ branches, but they misfit the degree 2 $_5S$ coefficients. The $_5S$ coefficients are much better fit by M84C + LO2.56. The significance of this is related to the assumed scaling between δv_s and δv_p structures and is discussed further in section 7.2. All four models fit the degree 4 structure coefficients well on each of the overtone branches ($n = 1$, 2, and 5), owing largely to the large relative uncertainties in these measurements.

The high cross-correlation values of the observed splitting functions with the predicted splitting functions of each of the models reveals the geographical consistency of the models and shows that a substantial fraction of the χ^2 misfit is due to amplitude differences, as Figures 19 and 20 demonstrate.

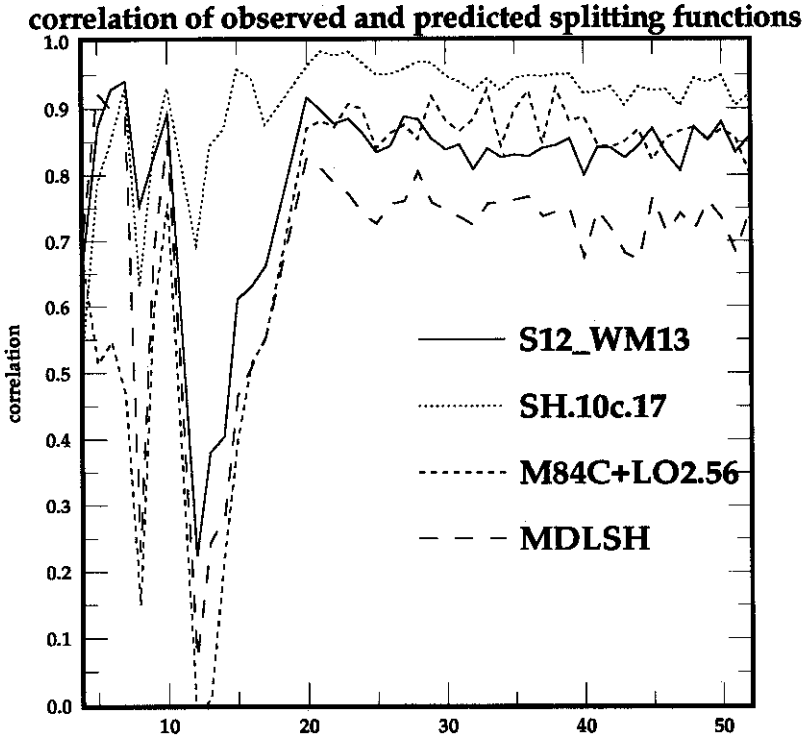

Figure 19b. Same as Figure 19a, but for the total correlation between the predicted and observed splitting functions taken over even degrees 2, 4, 6, and 8.

7. SOURCES OF DISCREPANCIES AND NEW INFERENCES

There are many possibilities for the differences among the models summarized in section 6; e.g., the data sets employed in the construction of each of the models differ, the relative weights given to the various data differ, and the models are parameterized differently. It is difficult for observers outside of the groups that have constructed each model to assess the absolute importance of each of these factors. However, we will discuss in section 7.1 one potential cause, errors in the a priori crustal models.

Two other potential causes of the differences between observed and model structure coefficients and splitting functions will also be discussed: the assumed linear scaling relationships between shear velocity and compressional velocity in the lower mantle and topography on mantle boundaries, in sections 7.2 and 7.3, respectively. Consideration of these factors leads to new arguments concerning the value of the scaling coefficient $dlnv_s/dlnv_p$ and speculations about the potential use of normal mode data to constrain mantle topography.

7.1. Effect of Crustal Corrections on Inferred Mantle Models

For certain multiplets the correction to the seismic structure coefficients due to the crustal models can be as large as the coefficients themselves. Thus it is important to assess the impact of the crustal correcti on the interpretation of mantle structure. *Woodhouse and Dziewonski* [1984] reported that the crustal correction they applied in M84C led to significant perturbations relative to M84A between 50 and 250-km depth. As Figure 21 shows, the rms of the total difference at even degrees (2–8) in $\delta v_s/v_s$ between M84C and M84A falls nearly linearly from ~0.85% at the top of the mantle to zero at the base of the Transition Zone. This effect does not extend into the lower mantle, since the M84 models were truncated at 670-km depth.

The nature of the change in mantle structure caused by the inclusion of a crustal model is a function of the method of inversion for mantle structure and of the data employed. One can alternatively assess the effect of unmodeled crustal structure on inferred mantle structure by inverting the crustal structure coefficients themselves for volumetric structure. Figure 21 also shows the result of inverting the fundamental mode structure coefficients, ${}_0S_8-{}_0S_{52}$, of the Harvard crustal model for perturbations to mantle structure $\delta v_s/v_s$ using the simple six-shell parameterization described by *Ritzwoller and Lavely* [1994]. With this simple parameterization, crustal structure, if left uncorrected, would bias volumetric models at the 0.60% rms level in the top 200 km of the mantle relative to PREM. T six-layer parameterization has a poorer radial resolution than the Legendre polynomials used by *Woodhouse and Dziewonski* [1984], and therefore the mantle structure has a lower peak rms value and is

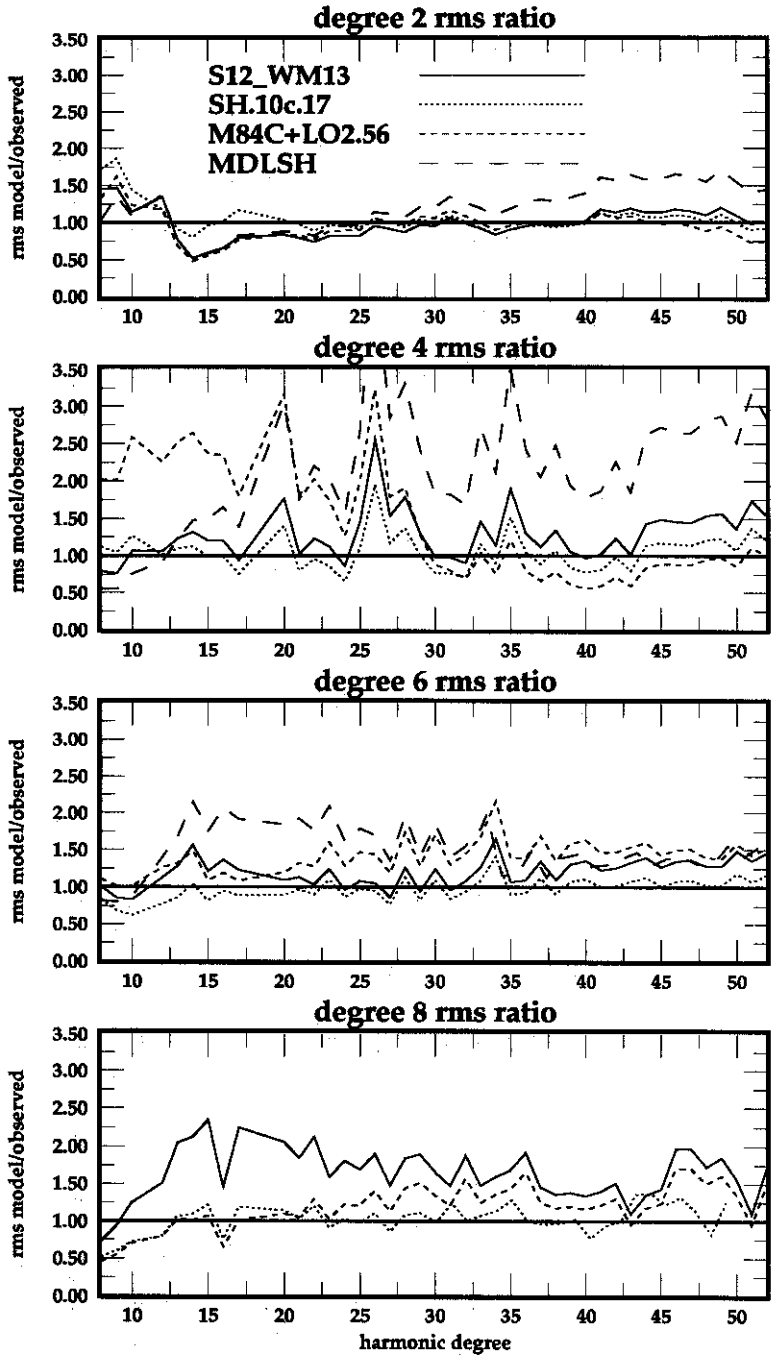

Figure 20a. Ratio of the rms of each predicted fundamental mode splitting function relative to the rms of the observed splitting function, plotted separately as a function of degree s of structure.

aliased farther away from the crust. This accounts for the difference in maximum magnitude of the aliased structure near the top of the upper mantle. In addition, we allow structure to leak into the lower mantle, which also lowers the upper mantle contribution somewhat. This is analogous to the observation that the spherical shell model SH.10c.17 has a lower rms amplitude in the uppermost mantle than S12_WM13, which is parameterized in terms of polynomials with depth.

As Figure 21 shows, the distribution of the rms amplitude of the crustal bias across the mantle is a function of the method of inversion and choice of data. The depth-averaged magnitude of the bias falls off from the surface through the upper mantle at approximately the same rate as the rms magnitude of the aspherical models themselves. The size of the rms bias relative to the rms of the aspherical models runs between 50 and 100%. Clearly, then, the use of a crustal model is necessary to infer upper mantle structure accurately. To estimate the nature of the expected errors in the current generation of crustal models and how they can affect inferred mantle structure, we take

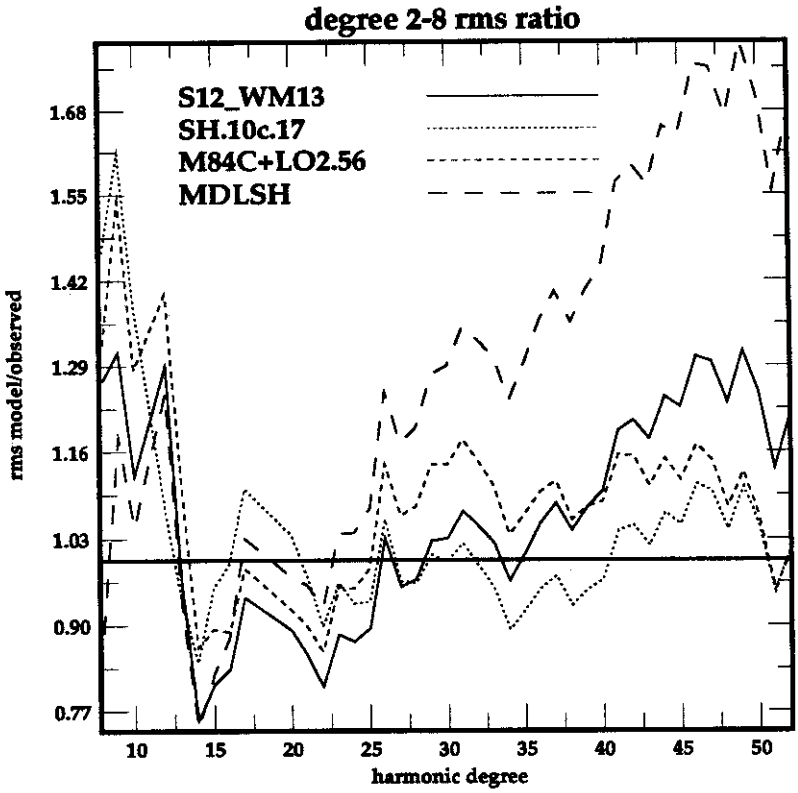

Figure 20b. Same as Figure 20a, but for the total rms taken over all even degrees of structure.

the difference between the structure coefficients computed with the Harvard and Scripps crustal models as an estimate of the error in the crustal models and invert them for mantle structure. The result of this inversion (again with ${}_0S_8$–${}_0S_{52}$ structure coefficients and a six-shell mantle model) is also shown in Figure 21. The rms of the volumetric bias attributed to errors in the crustal model runs between approximately 0.05 and 0.25% relative to PREM, or about 25% relative to the aspherical models themselves. With 25% errors in rms amplitude across the entire upper mantle expected from errors in the crustal model, efforts should be devoted in the future to improving confidence in the crustal models.

7.2. Constraints From New Mantle Models on the Scaling Between v_s and v_p

The numerical values of the scaling coefficients in equations (3) affect the amplitude of the integral kernel ${}_kK_s$ in the definition of the normal mode structure coefficients (equation (7)). If $\delta m_s^t = (\delta v_s)_s^t/v_s$, then

$$ {}_kK_s(r) = {}_kS_s(r) + \left(\frac{dlnv_p}{dlnv_s}\right)_k P_s(r) + \left(\frac{dln\rho}{dlnv_s}\right)_k R_s(r), \tag{12} $$

consistent with equation (A5) below. Uncertainties in the values of the scaling coefficients result in ambiguities in the amplitude of the inferred models and exacerbate comparison between free oscillation and body wave data and models. Problems with the estimation and use of scaling relationships have been discussed by *Ritzwoller et al.* [1988] and a much more complete discussion is presented by *Li et al.* [1991b]. Here we briefly summarize the salient points and reanalyze the problems in light of the new mantle models.

Discussion here will concentrate on the relationship between δv_s and δv_p. As can be seen in Figure 22, there is almost no sensitivity to perturbations in the density, except for very low harmonic degree multiplets ($l < 7$), if elastic structure is represented by δv_s and δv_p. Therefore errors in $dln\rho/dlnv_s$ do not appreciably affect the misfit for any of the multiplets considered here. (However, as will be shown in Figure 31 and discussed in section 9.5, sensitivity to density is improved in the κ, μ representation of elastic structure.) In addition, Figure 22 shows that for all but the low-degree multiplets on the higher-overtone branches, the sensitivity to perturbations in v_p is reduced by a factor of 2 or more relative to perturbations in v_s. The lower sensitivity to v_p relative to v_s implies that errors in estimates of $dlnv_p/dlnv_s$ are important only for the overtone multiplets, and these are the normal mode structure coefficients on which we will focus.

In principle, it is straightforward to constrain $dlnv_s$, $dlnv_p$ from shear and compressional travel time residuals (δt_s and δt_p), from independent models of δv_s and δv_p, and/or from normal mode data. Station correc-

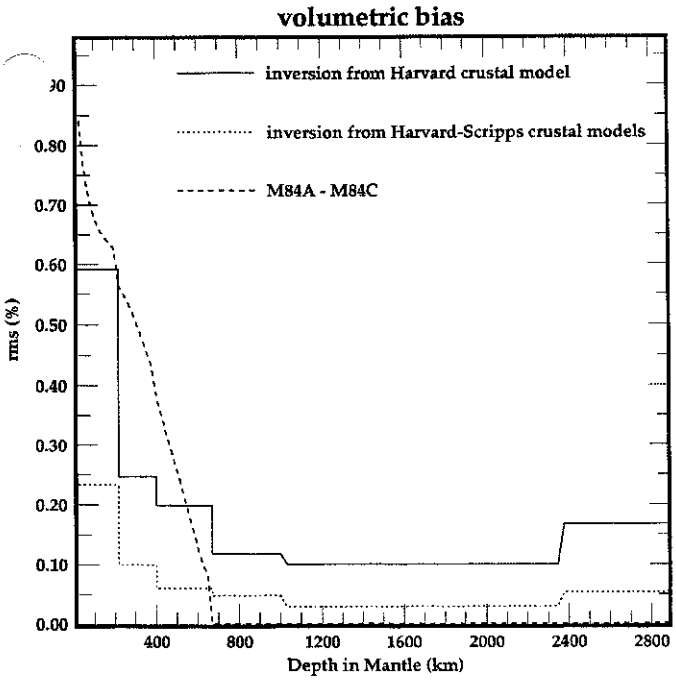

Figure 21. Result of inverting fundamental mode (${}_0S_8$–${}_0S_{52}$) structure coefficients computed from the Harvard crustal model as if they were due to mantle volumetric structure (solid line). The norm of volumetric structure on the vertical axis was computed using equation (4) and is expressed as a percent of spherically averaged v_s from PREM at each depth. Also shown are root-mean-square of the difference between M84C and M84A in the upper mantle (dashed line) and result of inverting the difference in the structure coefficients between the Harvard and Scripps crustal models as if they were due to mantle volumetric structure (dotted line).

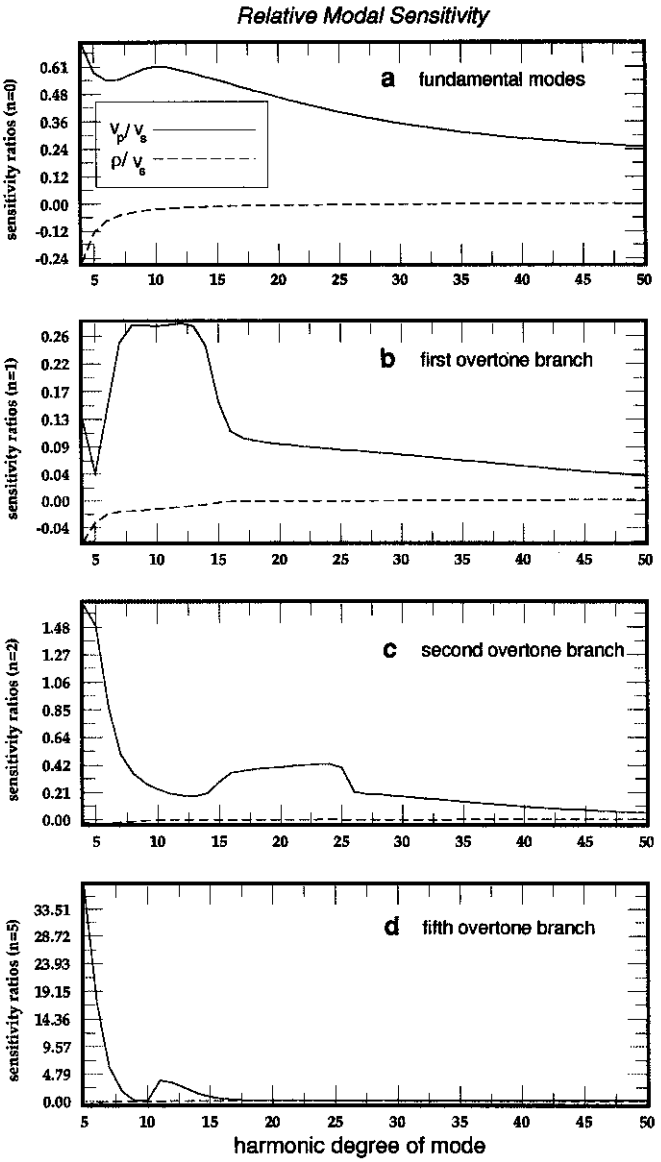

Figure 22. Normal mode sensitivity to v_p and ρ relative to sensitivity to v_s as a function of harmonic degree l, for the n = (a) 0, (b) 1, (c) 2, and (d) 5 branches. Solid and dotted lines represent the modal sensitivity of v_p and ρ, respectively, relative to v_s. (That is, $\int {}_kP_s(r)\,dr/\int {}_kS_s(r)\,dr$ and $\int {}_kR_s(r)\,dr/\int {}_kS_s(r)\,dr$, where ${}_kP_s(r)$, ${}_kS_s(r)$, and ${}_kR_s(r)$ denote the sensitivity kernels to perturbations in v_p, v_s, and ρ. See equations (A4)–(A6).) In the (δv_p, δv_s, $\delta\rho$) representation of 3-D structure, most normal modes are dominantly sensitive to perturbations in v_s, somewhat less sensitive to perturbations in v_p, and virtually insensitive to perturbations in ρ. Exceptions occur at lower l and higher n, where the v_p sensitivity is large. Only the degree s = 2 sensitivities are shown here, since sensitivities at higher degrees are similar.

tions are dominantly sensitive to the upper mantle and have been determined both on a global scale [e.g., *Hales and Doyle*, 1967; *Wichens and Buchbinder*, 1980; *Toy*, 1989] and regionally [e.g., *Romanowicz and Cara*, 1980; *Souriau and Woodhouse*, 1985] to estimate this ratio. The resulting values of $dlnv_s/dlnv_p$ vary widely (~1.3–2.4), and show strong lateral variations. Regional-scale studies of *ScS-S* and *PcP-P* differential travel times have suggested a higher value of this scaling coefficient than the laboratory studies (~2.0), and have been ascribed to heterogeneity in the lower mantle. Direct comparison of v_p and v_s models in the lower mantle also appears to indicate a value of $dlnv_s/dlnv_p > 2.0$ [*Dziewonski and Woodhouse*, 1987], although the correlation of δv_s and δv_p in the lower mantle has been questioned by *Masters et al.* [1992]. In a more complete study of normal mode splitting functions dominantly sensitive to the lower mantle, *Li et al.* [1991b] determine the bounds $1.65 < dlnv_s/dlnv_p < 2.5$, with a 75% confidence discriminating against the value of 1.25 normally used in global-scale studies.

7.2.1. Estimates of $dlnv_s/dlnv_p$ from normal mode data. As is discussed in section 5.1 and displayed in Figure 16a and Table 7, S12_WM13 fits the observed low-harmonic-degree structure coefficients along the ${}_1S$ branch remarkably well. Figure 22 shows that the ${}_1S$ multiplets are nearly insensitive to compressional velocity variations, and since S12_WM13 is a δv_s model, errors in the scaling coefficient $dlnv_s/dlnv_p$ will have only a minimal effect on the fit to the struc-

ture coefficients along this branch. In contrast, Figure 22 shows that ${}_5S$ multiplets possess the opposite sensitivity, being nearly insensitive to shear velocity variations. The χ^2 misfits listed in Table 9 indicate that S12_WM13 does not fit the ${}_5S$ multiplets nearly as well as it fits the ${}_1S$ multiplets. Figure 16c shows that S12_WM13 overpredicts the magnitude of the majority of the structure coefficients relative to the observations along the ${}_5S$ branch. Thus it is likely that the lower mantle δv_p model computed from S12_WM13, which dominates the fit to the ${}_5S$ multiplets, is too large in magnitude. A scaling coefficient $dlnv_s/dlnv_p \sim 2.0$ brings the predicted structure coefficients for S12_WM13 and for SH.10c.17 into much better agreement with the data, consistent with the conclusions of *Li et al.* [1991b]. This conclusion is not vitiated by the possibility of topography on the CMB potentially producing the misfit. The ${}_5S$ coefficients are quite insensitive to CMB topography.

A similar argument was made by *Giardini et al.* [1987, 1988] based on the relationship of misfit of the ${}_1S$ and ${}_5S$ multiplets computed from the model M84C + LO2.56. Comparison of Figures 16a and 16c and Table 7 indicates that the δv_p model LO2.56 fits the v_p sensitive ${}_5S$ multiplets better than S12_WM13, but it fits the v_s sensitive ${}_1S$ multiplets worse than S12_WM13. This pattern of misfit can also be resolved by using a scaling coefficient $dlnv_s/dlnv_p \sim 2.0$. The inference of this value is not as straightforward as the case in which the basis model is a δv_s model such as S12_WM13, since the ${}_1S$ multiplets are very sensitive to topography on the CMB. Thus the source of the misfit of M84C + LO2.56 to the ${}_1S$ multiplets could have been attributable to CMB topography as argued by *Ritzwoller et al.* [1988]. A clever recombination of data with differential sensitivity to volumetric and topographic structures by *Li et al.* [1991b] circumvented this problem, which allowed bounds to be placed on the scaling coefficient values irrespective of CMB topography.

7.2.2. Estimates of $dlnv_s/dlnv_p$ from ratios of mantle models. The scaling coefficient $dlnv_s/dlnv_p$ can also be estimated directly from the radius dependent ratio of the rms amplitudes of LO2.56, which is a δv_p model, and the other models considered here, which are all δv_s models. (This is similar to the procedure of *Dziewonski and Woodhouse* [1987].) Figure 23 displays the values of the ratio of the rms values of the models S12_WM13, SH.10c.17, and MDLSH divided by the rms of LO2.56, as a function of radius across the lower mantle for each of the even degrees, $2 \leq s \leq 6$, and combined across all degrees (even and odd) up to and including degree 6. Values of this ratio should be interpreted only when the geographical correlation between the compressional and shear velocity structures is high. Figure 23 displays only those values of $dlnv_s/dlnv_p$ at radii for which the given shear velocity model is correlated with LO2.56 above approximately the 75% confidence level.

There is considerable variation in $dlnv_s/dlnv_p$ between degrees for each model and between models at each degree. The ratios tend to decrease with degree, with the scaling coefficients estimated from S12_WM13 and SH.10c.17 agreeing quite well in the lower half of the lower mantle. However, since the rms amplitude of MDLSH is smaller than the other models in the lower mantle, the estimate of $dlnv_s/dlnv_p$ for MDLSH is generally lower. Considering the ratio of the models across all degrees $s \leq 6$ averaged across the entire mantle, the $dlnv_s/dlnv_p$ estimates for S12_WM13, SH.10c.17, and MDLSH are approximately equal to 2.8, 3.1, and 1.75, respectively. Since the parts of these models within approximately 500 km of the CMB are probably estimated most accurately, it may be better to use only the ratios in this region. The scaling coefficient for S12_WM13, SH.10c.17, and MDLSH averaged over the bottom 500 km of the lower mantle are approximately 2.0, 2.25, and 1.25, respectively. These values for S12_WM13 and SH.10c.17 are more closely in agreement with the normal mode results in section 7.2.1, since the normal mode data preferentially sample the lowermost lower mantle. However, this scaling ratio from MDLSH is in better agreement with traditional estimates of $dlnv_s/dlnv_p$ determined from laboratory measurements.

Because of this high variance between the models as well as the physically unrealistic size of the ratios from S12_WM13 and SH.10c.17 averaged over the entire mantle, the utility of estimating $dlnv_s/dlnv_p$ from model ratios is questionable at this time, especially considering that the lower-degree components of the model display even higher values of the scaling coefficient. Consequently, more recent v_p models should be used to investigate this issue further, and focused efforts need to be expended to constrain v_s structures accurately across the lower mantle.

7.3. Topography on the 660-km Boundary

In a pair of complementary studies, *Ritzwoller and Lavely* [1994] and *Rodgers and Wahr* [1994] estimated the effect of realistic models of boundary topography on the 220-, 400-, and 670-km boundaries on inversions for purely volumetric structure. The volumetric models that resulted from the inversion of the synthetic normal mode structure coefficients and S wave travel time residuals were therefore estimates of the topographic bias in inferred volumetric models from the individual data sets. Their synthetic experiments were similar to the crustal bias experiment discussed in section 7.1 and displayed qualitatively similar results: topographic structure aliases into volumetric structure in the vicinity of the boundaries, and the geographical dependence of the biased volumetric structure is strongly correlated with the geographical dependence of the boundary model. The rms size of the volumetric

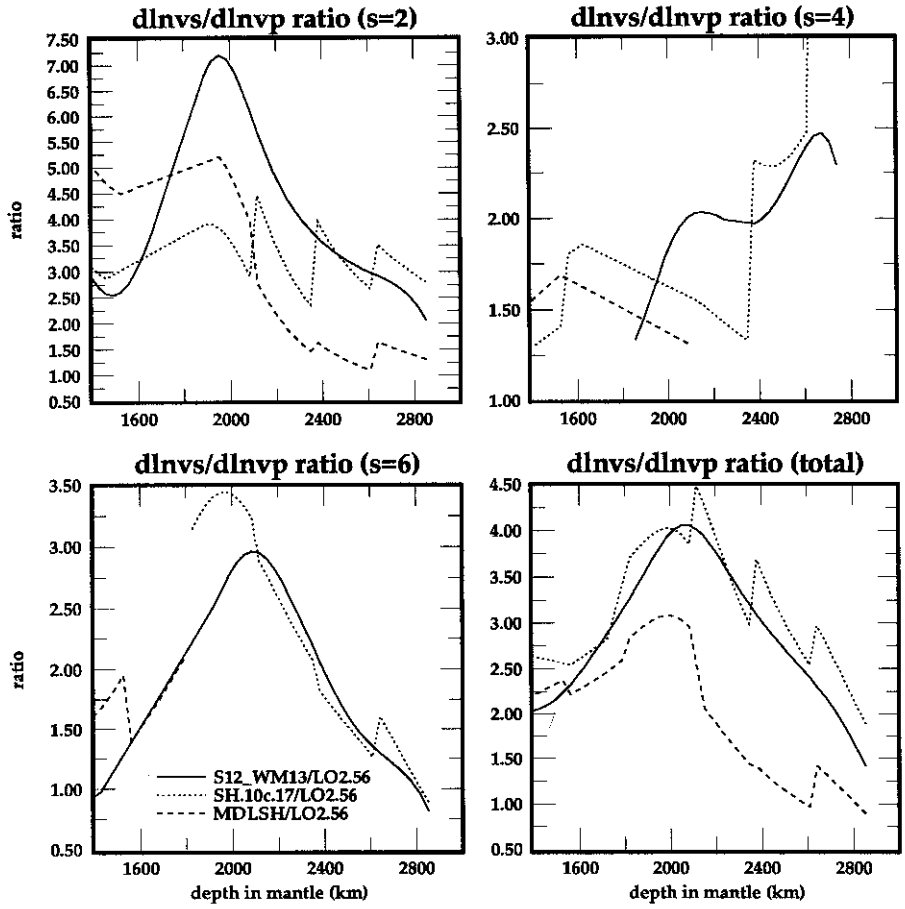

Figure 23. The rms ratios rms[S12_WM13]/rms[LO2.56] (solid), rms[SH.10c.17]/rms[LO2.56] (dotted), and rms[MDLSH]/rms[LO2.56] (dashed), plotted as a function of radius in the lower mantle at all points at which LO2.56 and the model in the numerator of each ratio are correlated with a confidence of 75% or higher. Ratios for each of the even degrees are shown as well as the combination over all even and odd degrees, $1 \leq s \leq 6$.

bias is a function of the amplitude of the topography, the model parameterization, the method of inversion, and, importantly, the data used.

Using the 660-km boundary model of *Shearer and Masters* [1992], ad hoc but realistic models of topography on the 220- and 400-km boundaries, synthetic normal mode data, and a simple six-shell mantle parameterization, *Ritzwoller and Lavely* [1994] found that inferred Transition Zone and uppermost lower mantle structure may contain a 30% bias relative to the magnitude of aspherical volumetric structure due to topographic aliasing. For *S* waves piercing the 670-km discontinuity and a radial model parameterized with Chebyshev polynomials with a higher resolution than this six-shell model, *Rodgers and Wahr* [1994] concluded that the level of biasing would be somewhat less than that from the normal mode experiments, perhaps 20% of that observed by Ritzwoller and Lavely for the same model of boundary topography. The amplitude of this bias is a strong function of how compressed the aliased volumetric structure is allowed to be near the boundary. Therefore topography on the 670-km discontinuity should be biased into the volumetric models considered here, but the degree of biasing would be a function of the relative weighting of the normal mode and body wave data used in each inversion as well as of the model parameterization and technique of inversion. In the following, we discuss whether this may account for some of the differences between the models S12_WM13 and SH.10c.17 in the Transition Zone and near the top of the upper mantle as well as for their differences in the fit to the normal mode structure coefficients.

The amplitude of the topographic models of *Shearer and Masters* [1992] and *Shearer* [1993] on the 400-km and 660-km discontinuities is sufficient to have a significant effect on the normal mode data and, in fact, should be observable in the normal mode structure coefficients. The nonaxisymmetric component of the degree 2 part of *Shearer and Masters'* [1992] 660-km model, which contributes a significant component of the observed topographic depressions beneath subducting regions near Japan and South America, is shown in Figure 24a. In the following we examine how

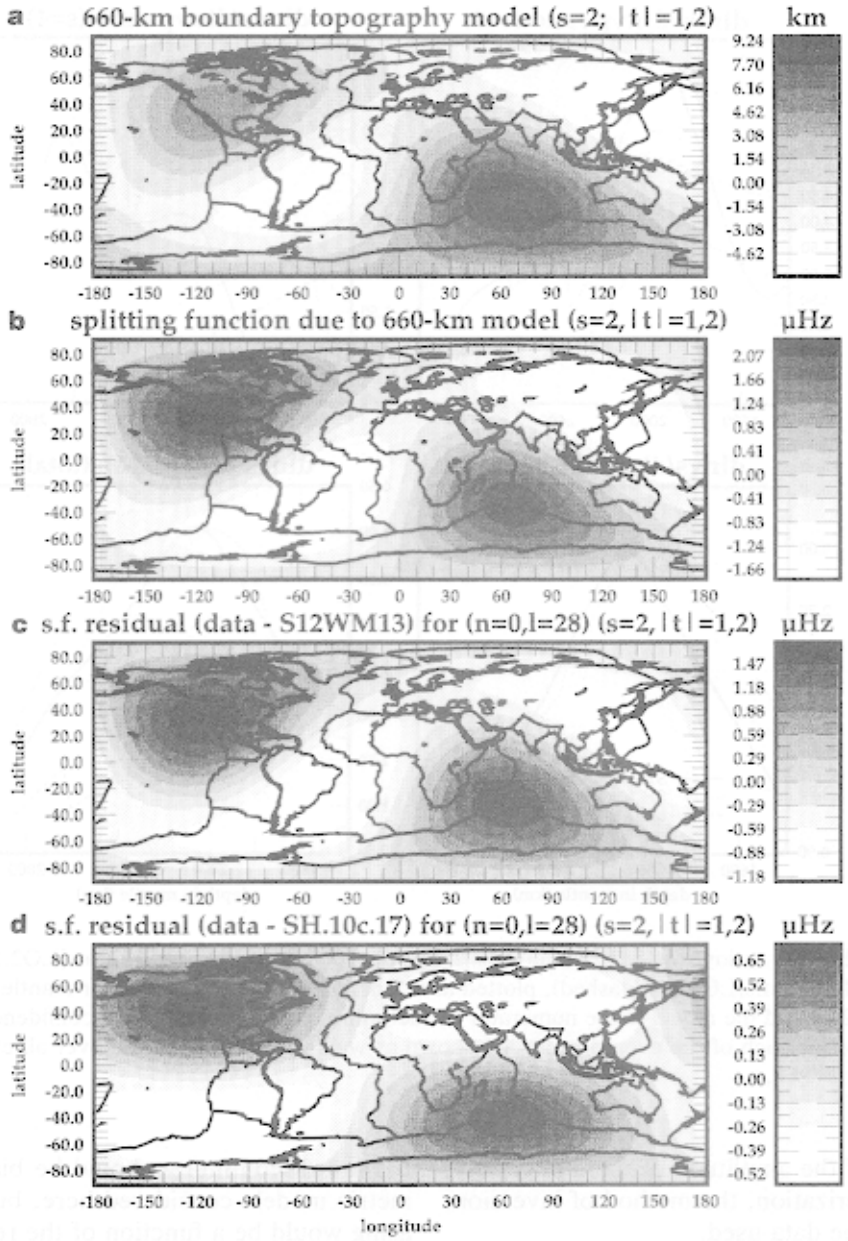

Figure 24. (a) The nonaxisymmetric degree 2 part of the 660-km topographic model of *Shearer and Masters* [1992]. (b) The splitting function for the multiplet ${}_0S_{28}$ computed for the nonaxisymmetric degree 2 part of Shearer and Masters' topographic model; ${}_0S_{28}$ has peak sensitivity to structure near the 660-km boundary. (c) The residual splitting function computed from the difference between the observed splitting function and that predicted from S12_WM13 for ${}_0S_{28}$. (d) The residual splitting function computed from the difference between the observed splitting function and that predicted from SH.10c.17 for ${}_0S_{28}$. Figures 24b and 24c are highly correlated (correlation of 0.96, 99.8% confidence level), suggesting that 660-km topography may be responsible for part of the discrepancy between the observations and predictions from S12_WM13.

the addition of topography on the 660-km boundary to the volumetric models S12_WM13 and SH.10c.17 affects the fit to normal mode structure coefficients sensitive to this boundary. Ignoring multiplets in the Coriolis coupling band ($10 < l < 20$), the effect should be greatest for the multiplets ${}_0S_{20}$–${}_0S_{35}$, as can be seen from the sensitivity kernels plotted in Figure 25.

The nonaxisymmetric component of the splitting function for ${}_0S_{28}$ computed from *Shearer and Masters*' [1992] 660-km boundary model is shown in Figure 24b. The axisymmetric part of the degree 2 splitting function is ignored here and below because of the uncha acteristically large misfit of S12_WM13 to this coeffi cient, as can be seen in Figure 14a and Table 4. To quantify the magnitude of the topographic effect on the splitting functions relative to the misfit of the structure

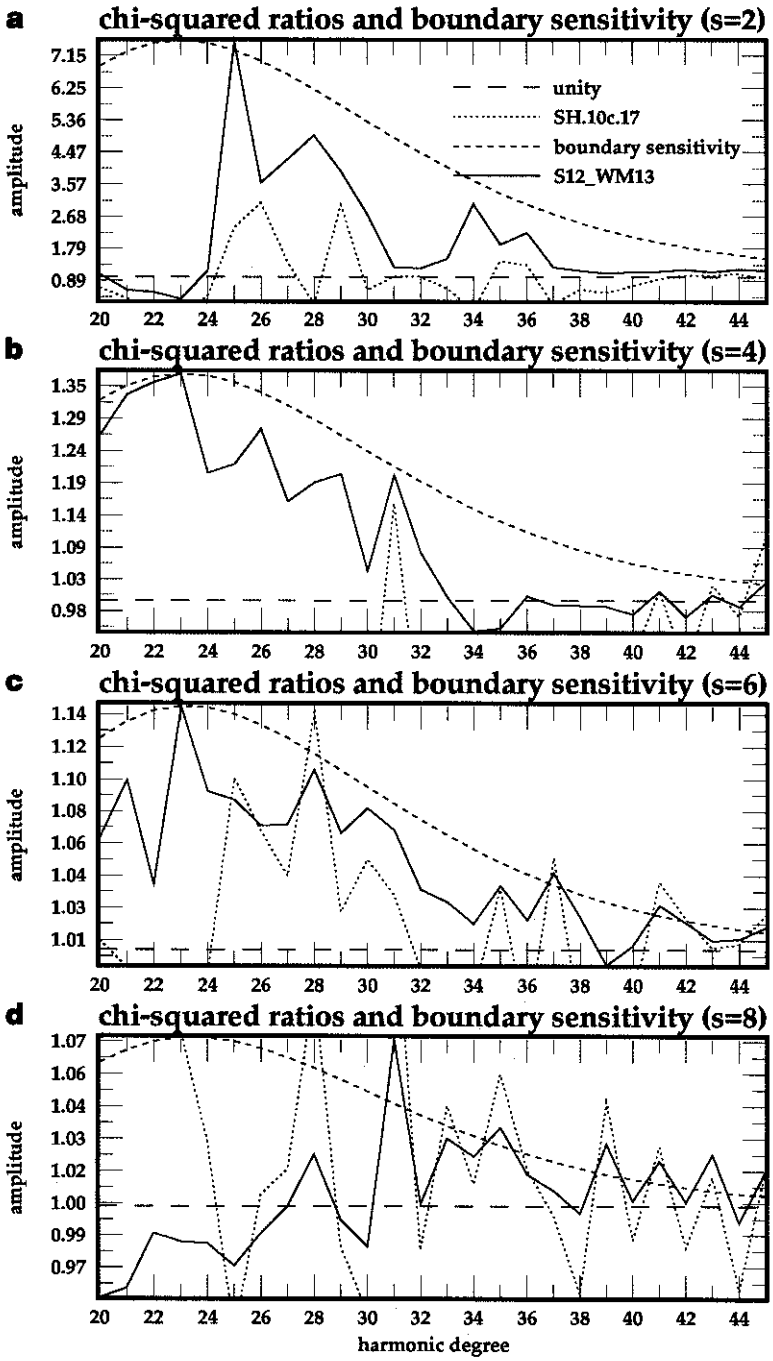

Figure 25. Misfit improvement to the observed structure coefficients with the addition of *Shearer and Masters'* [1992] 660-km topography model, for even degrees of structure (a) 2, (b) 4, (c) 6, and (d) 8. The solid line is the χ^2_{ratio} (equation (13)) computed using S12_WM13 (numerator) and the combined contribution of S12_WM13 and Shearer and Masters' 660-km boundary model (denominator) for modes along the fundamental branch in the range $20 \leq l \leq 45$, and the dotted line is similar but for the model SH.10c.17. The short-dashed line is the boundary sensitivity kernel ${}_kD_{ds}$ (equation (7)) for the 660-km boundary and peaks in the range $20 \leq l \leq 30$. Improved fits to the data are reflected by χ^2 ratios greater than unity (above the long-dashed line). The χ^2 ratios approach unity as the boundary sensitivity decreases.

coefficients computed from the volumetric models alone, it is useful to consider the residual splitting function. The residual splitting function is defined as the difference between two splitting functions: the first is computed using the observed structure coefficients (corrected for the crustal model and Coriolis coupling), and the second is the splitting function computed for the appropriate volumetric model. Figures

24c and 24d represent the nonaxisymmetric degree 2 residual splitting functions for ${}_0S_{28}$ of the models S12_WM13 and SH.10c.17, respectively.

Topography on the 660-km boundary may be a cause of the misfit represented by the residual splitting function if the geographic patterns and peak-to-peak amplitudes of the topographic and residual splitting functions are similar. Clearly, the residual splitting function computed with S12_WM13 bears a strong resemblance to the splitting function predicted by *Shearer and Masters'* [1992] 660-km boundary model, in terms both of magnitude and of pattern. The significance of correlation is at ~97% confidence level. The residual splitting function of SH.10c.17 compares less favorably with the topographic splitting function.

A useful measure of the influence of boundary topography on the misfit to a set of structure coefficients is the χ^2_{ratio}, the ratio at each degree of structure for each multiplet of the χ^2 value computed using a volumetric model alone and the χ^2 value for the combined volumetric + topographic model:

$$\chi^2_{\text{ratio}}(s, l) = \chi^2_{s,l}(\text{volume})/\chi^2_{s,l}(\text{volume + boundary}), \tag{13}$$

$$\chi^2_{\text{ratio}}(s, l) = \sum_{t=-s}^{s} \left[\frac{{}_l\bar{c}^t_s - {}_lc^t_s}{{}_l\sigma^t_s} \right]^2 \Bigg/ \sum_{t=-s}^{s} \left[\frac{({}_l\bar{c}^t_s + {}_l\hat{c}^t_s) - {}_lc^t_s}{{}_l\sigma^t_s} \right]^2, \tag{14}$$

where ${}_lc^t_s$ and ${}_l\sigma^t_s$ are the observed structure coefficient for the fundamental multiplet l and its uncertainty and, as defined in equation (7), ${}_l\bar{c}^t_s$ is the structure coefficient computed from volumetric structure alone and ${}_l\hat{c}^t_s$ is the coefficient computed from 660-km topography alone. An improved fit to the data for a given multiplet and degree of structure would be reflected by a χ^2_{ratio} greater than unity, i.e., $\chi^2_{\text{ratio}} > 1$. The solid line in Figure 25a is the $\chi^2_{\text{ratio}} = \chi^2(\text{S12\_WM13})/\chi^2(\text{S12\_WM13 + 660})$ computed using nonaxisymmetric degree 2 structure, and the dotted line is similar but for the model SH.10c.17. The short-dashed line is the square of the sensitivity kernel ${}_kD_{d2}$ of equation (7) for the 660-km boundary, and the long-dashed line demarcates the regions of improved and degraded data misfit, i.e., the regions above and below unity. The sensitivity kernels are plotted on a normalized vertical scale in which zero sensitivity corresponds to a value of unity for the χ^2_{ratio}. The boundary sensitivity for each degree of structure maximizes in the interval $20 \le l \le 30$. Figures 25b, 25c, and 25d are similar to Figure 25a but for degrees of structure 4, 6, and 8, respectively. The χ^2_{ratio} for each of the models and for each degree of structure approaches unity as the sensitivity of the multiplets to perturbations on the 660-km boundary decreases.

Considering first S12_WM13, the addition of the 660-km model improves the fit to nearly all of the multiplets displayed in Figure 25, and the improvement is greatest in the range of maximum boundai sensitivity. The l dependence of the χ^2_{ratio} mimics the t dependence of the 660-km boundary sensitivity and approaches unity as the sensitivity to perturbations on the 660-km boundary decreases. The χ^2_{ratio} for degree 2 structure is the largest, which might be expected because this degree is the dominant signal in Shearer and Masters' boundary model and because the degree 2 observed structure coefficients have the smallest relative errors. The χ^2_{ratio} reduces monotonically with degree of structure, until the results for $s = 8$ appear to be in the noise.

Figure 26 is similar to Figure 14a and displays the misfit of the fundamental mode structure coefficients most sensitive to the 670-km boundary (${}_0S_{20}$–${}_0S_{35}$) computed from S12_WM13 both with and without *Shearer and Masters'* [1992] 660-km topographic model. For most azimuthal orders, the fit to the observed coefficients is appreciably improved. The χ^2 measurements of misfit for these multiplets at each of the degrees $s = 2, 4, 6, 8$ are listed in Table 10. These statistics display an improvement in fit at degrees $s = 2$ and 4 of structure when the 660-km topographic model is added to S12_WM13 but a degradation of fit when it is added to the model SH.10c.17. The addition of 660-km topography to S12_WM13 reduces the misf relative to the misfit for SH.10c.17 by about 25% at degrees $s = 2$ and 4. However, even with the addition of the topographic model, S12_WM13 does not fit the normal mode data as well as SH.10c.17.

In conclusion, Figures 24–26 support the hypothesis that topography on the 660-km boundary may be a significant source of the misfit for multiplets sensitive to the Transition Zone and top of the lower mantle and may explain part of the difference between S12_WM13 and SH.10c.17 in this region. This possibility is investigated further by *Lavely et al.* [1994]. Figures 24–26 also suggest the possibility that the combination of the data types, relative weighting, and the quantity of data used by *Su et al.* [1994] in the construction of S12_WM13 may have avoided some of the volumetric biasing produced by topographic boundaries in inversions that use more limited data sets. This holds out the hope for using normal mode data to infer topography on internal mantle boundaries. This has been attempted before by *Ritzwoller et al.* [1988] and *Smith and Masters* [1989a], but owing to the tradeoff between volumetric and boundary structures for the normal mode data they employed in their inversions, the models of boundary topography were dismissed. *Woodward and Masters* [1991a] came to the sam conclusion for a purely body wave study. The curren prospects for the use of normal mode data to infer boundary topography are brighter now only if the use of body wave data in the construction of the latest

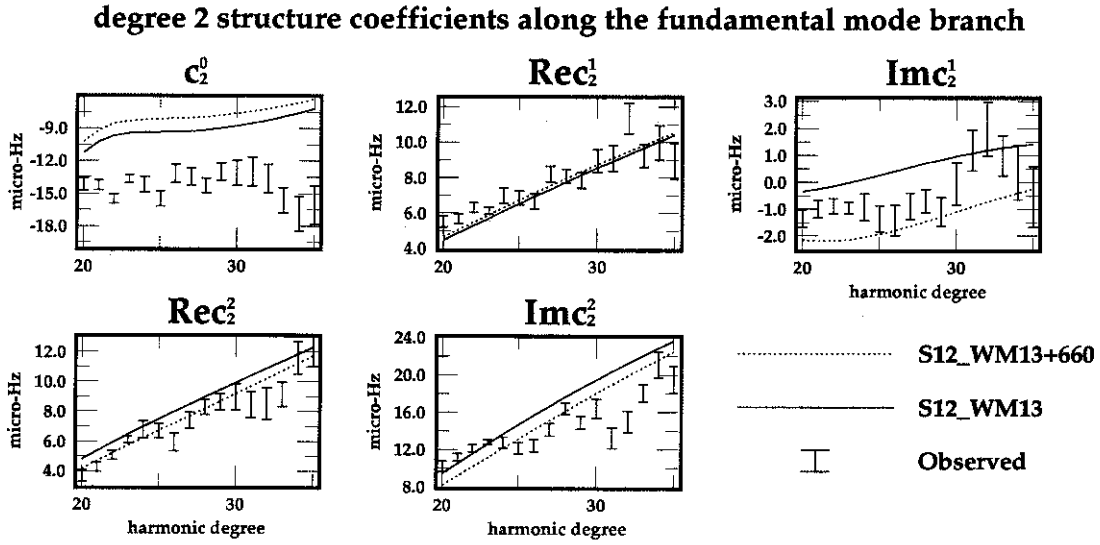

Figure 26. The degree 2 structure coefficients (in units of microhertz) for the multiplets most sensitive to 670-km boundary topography ($_0S_{20}$–$_0S_{35}$) and estimated errors from *Smith and Masters* [1989a] and those computed for the volumetric models S12_WM13 (solid line) and S12_WM13 together with the 660-km topographic model of *Shearer and Masters* [1992] (dotted line). On average the addition of topography on the 660-km boundary to model S12_WM13 improves the fit to the observed normal mode structure coefficients.

mantle models has desensitized the volumetric component of the models to topographic bias.

8. THE USE OF RADIAL CORRELATION FUNCTIONS AS CONSTRAINTS ON MANTLE CONVECTION

A number of key issues in the study of the dynamics of the Earth's deep interior hinge on an understanding of the degree to which flow is stratified by phase transitions or changes in bulk chemistry in the Transition Zone and across the 660-km boundary. Resolution of this problem is likely to rely on a combination of geodynamical, geochemical, and seismological constraints. A new step in this direction was taken by *Jordan et al.* [1993], who argued that the observed radial correlation lengths l_c of seismic Earth models can be used to discriminate among competing mantle convection models. The use of radial coherence as a diagnostic is motivated by the finding that the imposition of either a strong chemical change or an endothermic phase transition at an internal boundary in a numerical simulation of mantle convection significantly reduces the characteristic radial correlation length of convective structures in the vicinity of the boundary. This finding suggests that comparison of the radial correlation lengths of seismic Earth models with those calculated for a suite of mantle convection models may be able to be used to constrain the character of phase or chemical changes near the 660-km boundary. In general, correlation lengths are expected to maximize (or radial correlation functions swell) in the near-adiabatic interior of convecting layers and to minimize (or radial correlation functions pinch) in the vicinity of boundary layers.

Jordan et al. [1993] display the radial correlation functions of the numerical convection model described by *Tackley et al.* [1993] and of the seismic models SH.10c.17 and S12_WM13. To make the radial correlation plots directly comparable with one another, *Jordan et al.* [1993] adopted the degree 13 Chebyshev expansion of S12_WM13 as the reference parameterization. Thus they truncated the radial Chebyshev expansion of the convection model at degree 13 and fitted the constant layer representation of SH.10c.17 to Chebyshev polynomials up to degree 13. The resulting $R(r, r')$ plots revealed that there is a local minimum in l_c near the 660-km boundary in the convection model but not in the seismic models. Thus *Jordan et al.* [1993] argued that any stratification induced by phase or chemical changes across the midmantle Transition Zone has a relatively small effect on whole mantle convection.

The dynamical interpretation of $R(r, r')$ may be compromised by several factors, including (1) the parameterization of the seismic models, (2) continuity or smoothness constraints imposed on the inverted seismic models across major phase or chemical boundaries, (3) the types of seismic data used in the construction of the seismic models, and (4) the intrinsic resolution of numerical convection models compared with that of seismic models.

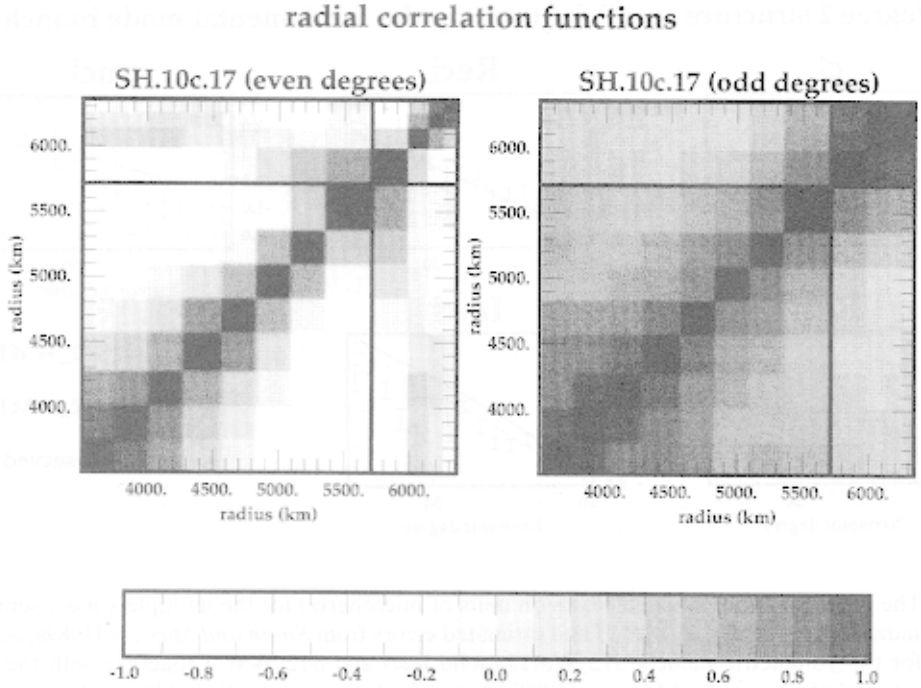

Figure 27. (left) Even and (right) odd degree radial correlation functions for SH.10c.17.

8.1. Ambiguities of Interpretation Caused by Model Parameterization and Smoothness Constraints

The choice of model parameterization and use of explicit radial smoothing constraints can yield models with dramatically different correlation lengths at various points in the mantle, in particular near the 660-km boundary. An example of the dependence of correlation length on model parameterization is provided by the hybrid model M84C + LO2.56, whose upper and lower mantle parts were estimated separately using distinct data sets. The discontinuity in $R(r, r')$ observed at 660-km depth for M84C + LO2.56 is not present in the radial correlation function computed for the model S12_WM13. Another example is the seismic Earth model SH8/U4L8 of *Dziewonski and Woodward* [1992], which was inverted from a data set similar to that of S12_WM13. As *Jordan et al.* [1993] point out, in contrast with S12_WM13, SH8/U4L8 displays a sharp decrease in the radial correlation length near the 660-km boundary. The upper mantle and lower mantle parts of SH8/U4L8 were parameterized separately, and smoothness constraints across the 660-km boundary were not imposed. The fact that a model that is continuous across the 660-km discontinuity can fit the data is interesting, but as the following discussion suggests, it is not straightforward to infer from this fact that the variation in Earth structure across the boundary is actually smooth.

8.2. Ambiguities of Interpretation Caused by the Data Themselves

Another problem in the dynamical interpretation of radial correlation functions is that the type and quantity of data used in the construction of a given seismic Earth model may lead to correlation features that are characteristic of the data themselves and which obscure potential dynamical features in plots of $R(r, r')$. For example, the parameterizations of SH.10c.17 and MDLSH are identical at depths greater than 200 km, but MDLSH displays a greater decorrelation across the 660-km boundary than SH.10c.17 and smaller correlations across adjacent layers throughout the lower mantle than SH.10c.17. As is argued in the following, this is probably due to the fact that Rayleigh wave (i.e., normal mode) data were used in the construction of SH.10c.17, but only Love waves (confined to the upper mantle) and *SH* body waves (turning in the lower mantle) were used in the construction of MDLSH. Normal mode data tend to constrain structures across the entire mantle, effectively applying a fairly coarse radial smoothing filter to the models. The radial smoothing applied by the use of absolute body wave travel times is probably less severe than normal mode smoothing.

The use of differential *ScS*-*S* and *SS*-*S* travel times, as opposed to absolute travel times, applies even more smoothing in the upper mantle than normal modes. The variation of radial smoothing characteristics between differential body wave and normal mode data can be seen in SH.10c.17 alone, since normal mode constraints were applied only at even degrees of the structures in this model. The odd degree and even degree radial correlation functions for SH.10c.17 are shown in Figure 27. The odd degree components of SH.10c.17 are constrained by body wave data alone, and the even degree components are constrained by

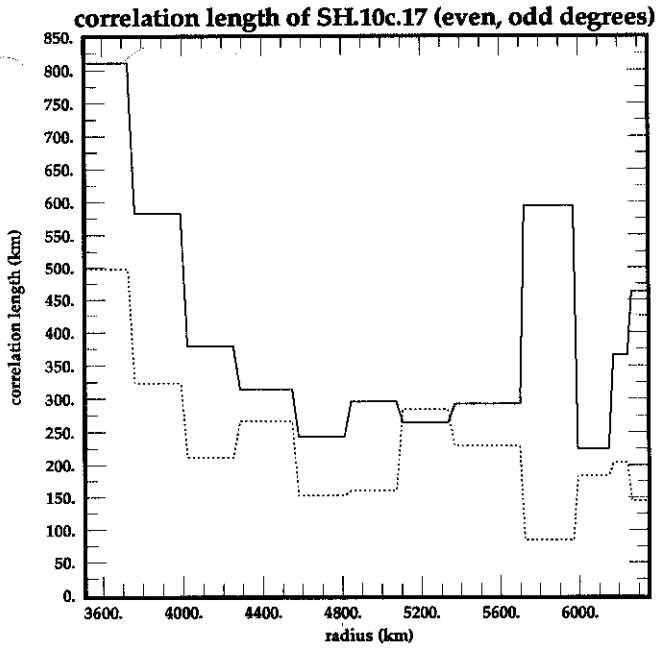

Figure 28. Even (dotted) and odd (solid) degree correlation lengths l_c for SH.10c.17, plotted as a function of radius across the entire mantle.

body wave data and by long-period Rayleigh waves that have sensitivity to depths extending into the lower mantle. The even degree radial correlation functions of SH.10c.17 display greater decorrelation across layers than their odd degree analogues. The difference between the correlation lengths l_c plotted separately for the even and odd degrees of SH.10c.17 across the entire mantle is shown in Figure 28. In the lowermost mantle the odd degree part of SH.10c.17 has a correlation length nearly twice as large as the even degree part of the models. This disparity decreases across the middle of the lower mantle but grows again in the upper mantle. This suggests that the use of long-period Rayleigh waves in SH.10c.17 improved radial resolution in the upper mantle and the use of differential travel times at odd degrees enforced a radial smoothing of structure that led to smoother structures both in the upper and in the lower mantle relative to MDLSH.

Therefore in the interpretation of $R(r, r')$ it is important to factor in the intrinsic smoothing characteristics of the types of waves present in each data set, which may differ from model to model. Otherwise, the dynamical interpretation of observations of decorrelation or lack of decorrelation at certain radii may be spurious, since the observations may reflect data sampling and resolution effects rather than dynamical effects associated with a chemical change or a phase transition.

8.3. Ambiguities of Interpretation Caused by Differences in Radial Resolution Between the Convective and Seismic Models

The radial resolution of numerical convection models relative to the intrinsic radial resolution of the seismic models clearly bears on the interpretation of the computed radial correlation functions. The determination of the radial resolution of the seismic models is not unequivocal. For example, the fact that the radial variation of structure of S12_WM13 is parameterized to Chebyshev degree 13 does not imply that structure in this model is resolved to this degree. Therefore it is possible that a decorrelation of structure near the 660-km boundary would not be observable in S12_WM13 if the intrinsic radial resolution of this model were lower, perhaps only Chebyshev degree 4 or 5.

Jordan et al. [1993] recognized potential problems with the resolving power of seismic Earth models and cited experiments by the Harvard group that attempted to show that radial structure could be resolved at least to Chebyshev degree 8 in the vicinity of the 660-km boundary. *Jordan et al.* [1993] pointed out that a radial resolution of degree 8 should be adequate to resolve a correlation length minimum near this boundary, since this minimum in the convection models continues to remain expressed, displaying only a 50% reduction in amplitude even when the convection model is truncated to Chebyshev degree 6. This resolution estimate was obtained by inverting synthetic seismic data computed for input structure specified by a single expansion coefficient of the model ($l = 11$, $m = 6$, and $n = 8$). The Harvard group showed that the input structure matched the inverted structure relatively well throughout the upper mantle and middle mantle. However, since this synthetic experiment (as described by *Su et al.* [1994]) ignores the effects of noise in the data, uncertainties in source locations and moment tensors, errors in the theoretical prescription used in the construction of the synthetic seismograms, and covariance between model components, the Chebyshev degree 8 estimate of resolution may not be sufficiently conservative. In fact, *Su et al.* [1994] point out that smearing, as they call it, is more significant in the radial than in the horizontal direction even for a Chebyshev degree 5 model.

A more realistic estimate of the extent to which structure is resolved by the seismic models would be obtained if synthetic seismic data, with the addition of realistic errors, computed from the *Tackley et al.* [1993] convection model were inverted. The resulting model would have been passed through a seismic filter and would therefore be directly comparable to seismic models inverted from actual data. Any deviation of the radial correlations between the convective and seismic models could then be attributable to the models themselves.

8.4. Conclusions

Caveats aside, the correlation plots for S12_WM13 and SH.10c.17 appear to be consistent with the interpretation that a phase or chemical change across the 660-km boundary does not significantly impede mantle convection. However, the consistency of MDLSH, SH8/U4L8, and M84C + LO2.56 with this conclusion is less convincing because of problems associated with data type, model resolution, and model parameterization.

As was discussed in section 3.3, the models SH.10c.17, M84C + LO2.56, and MDLSH display significant decorrelation across the radial level at approximately 1000-km depth. The dynamical interpretation of the decorrelation is not clear but warrants further examination. Is the observed decorrelation at 1000-km depth real, or is it an artifact of the data and parameterizations employed? If it is real, is it diagnostic of dynamical contrasts at or near this depth?

9. RESOLVING DISCREPANCIES AND FUTURE DIRECTIONS

At the outset of this review, we stated that global 3-D seismic models have three main purposes: (1) they are concentrated summaries of huge volumes of seismic data, (2) they can be used to provide data corrections to constrain other types of structures and source parameters, and (3) they can be interpreted to provide information about the composition and dynamics of the Earth. It is worthwhile to consider how the models discussed here have succeeded in fulfilling these goals.

The results of the comparison between the three-dimensional models presented here are encouraging in that the models agree well in the geographical distribution of heterogeneity and, with a few notable exceptions, do a relatively good job in fitting at least the geographical pattern defined by the normal mode structure coefficients. The gross characteristics of all the models are similar. However, there remains significant disagreement among the models in the radial distribution of heterogeneity and in the absolute amplitude of the boundary layer heterogeneity near the top of the upper mantle and of the heterogeneity in what may be a boundary layer near the top of the lower mantle, directly below the Transition Zone. In particular, there is a difference of nearly a factor of 2 in amplitude between SH.10c.17 and S12_WM13 and more than a factor of 3 in amplitude between SH.10c.17 and M84C + LO2.56 near the top of the upper mantle. After more than a decade of research, the largest change in the Harvard models (M84C + LO2.56 → S12_WM13) lies in the top of the lower mantle, where M84C + LO2.56 is uncorrelated with any of the later models.

We conclude therefore that although these models fulfill purpose 1 admirably, since the amplitude discrepancies among the models make their use in correcting data dangerous (as *Garnero and Helmberger* [1993] and *Romanowicz* [1990] have argued), they need to be applied with discrimination for purpose 2.

There are many fundamental questions concerning the composition and dynamics of the mantle to which global seismic models, combined with results from high-pressure experiments, geochemistry, and geodynamical computations, are relevant. We list a very incomplete subset here, divided into questions related to the mantle's composition and to its dynamics.

Compositional questions include the following: (1) What percentage of the observed seismic velocity variations results from lateral compositional variations? (2) How deep do compositional variations extend? Are they largely limited to the boundary layers surrounding the mantle? Is the body of the mantle well mixed? (3) How deep do the continents extend? (4) Are the compositional variations related to distinct chemical reservoirs? If so, how are such reservoirs related to variations in the geochemistry of lavas extruded at the surface? (5) Is there mixing across the core-mantle boundary?

Dynamical questions include the following: (1) What percentage of the observed seismic velocity variations result from lateral temperature changes? (2) Are surface observables, such as topography and the geoid, well predicted? (3) What is the driving mechanism of plate tectonics? How are the plates themselves and their motions related to deep-seated convective processes? (4) What is the large-scale structure of convection? Is the mantle dynamically stratified, is it a single system, or is it some combination of these end-members? What is the Earth's viscosity profile? (5) Are convective flows continuous across the transition from the upper to the lower mantle? What is the depth extent of oceanic ridges? What is the geometry of the conduits of upwelling material? Do rising thermal plumes exist in the lower mantle? If so, do they pierce the 660-km discontinuity? If so, how are they related to emerging observations of topography on internal mantle boundaries and to surface "hotspots"?

The resolution to some of these questions is relatively insensitive to the radial distribution of heterogeneity and to uncertainties at the factor of 2 level in amplitude. However, other applications are less robust, for example, estimating lateral temperature gradients in the neighborhood of boundaries or determining if plumes pierce certain boundaries (more below), and one should be aware of discrepancies and uncertainties among the models before inferences are made.

Therefore fulfilling purposes 2 and 3 and answering most of the questions listed directly above will await the resolution of the discrepancies among the models. (Of course, seismic models alone cannot address these questions; answers for many questions will also await advances in other areas of geophysics.) This suggests that although the current state of the models is very encouraging, the resolution of the remaining discrep-

ancies may provide a more significant scientific reward than is offered by the existing models. In order to resolve the differences among the models, however, we will need to address their causes.

The causes of the discrepancies can be categorized as due to "intrinsic" (or procedural) and "extrinsic" (or structural) effects. Intrinsic effects result from choices that are inherent to any inversion, such as relative data weighting, matrix damping, model parameterization, theoretical approximations, or data coverage. What is considered to be optimal in this context is subject to genuine dispute, and model uncertainties due to intrinsic effects are not easily overcome. Therefore intrinsic effects should be considered to represent a baseline uncertainty in a model which would be difficult to overcome. The nature of this baseline requires investigation and publicization. The magnitude of intrinsic effects can be uncovered with synthetic experiments but all too often is ignored. For this reason it is difficult to assess the culpability of intrinsic effects in producing the discrepancies among the global models considered here.

Extrinsic effects are caused by unmodeled or difficult to model features, such as the crust, subducted lithospheric slabs, other higher-order elastic structures, boundary topography, anelasticity, anisotropy, or source complexity. Since we do not necessarily possess accurate a priori models of each of these features, the assessment of the impact of extrinsic effects is tricky. However, since these features have a measurable seismic signature they can, in principle, be modeled, and we can ultimately move beyond the problems created by them.

To overcome the differences among the existing models and to produce more accurate models in the next generation, the impacts of these intrinsic and extrinsic effects will have to be more carefully studied and publicized. This review will end with a brief discussion of the following subjects: (1) reporting detailed misfit and model norm information with the models, (2) regular production and publication of summary data, (3) construction and use of a priori reference models of the crust and lithospheric slabs, (4) joint volumetric and internal boundary topography inversion, (5) focusing models to shorter wavelengths and incorporating regional models, data, and constraints, and (6) expanded role for normal mode data.

The first two subjects, matrix damping and the production of summary data, concern procedural issues. We feel that the recommendations made concerning these subjects will have to be adhered to in order to guarantee that future models can be held to the public scrutiny and testing that recognized improvement and advancement requires. We will also discuss each of the extrinsic effects listed: crust and lithosphere, internal boundary topography, short wavelength structures, anelasticity, and anisotropy.

9.1. Misfit Versus Model Norm

The largest discrepancies among the models are in amplitude and in the radial distribution of structure. This discrepancy undoubtedly results from a number of the intrinsic and extrinsic effects mentioned above. A leading cause, not yet discussed in this review, may be due to the fact that the researchers have used different means of matrix damping in constructing their models. This possibility is well recognized by global seismologists and has been discussed, for example, by *Park* [1989].

The importance of this effect relative to other impacts on model amplitudes would be easy to assess if when models are published, data misfit versus model norm tradeoff statistics (e.g., amplitude, roughness, etc.) would be regularly published as well. This can be partially excused, since the model builders have been chiefly concerned with addressing the distribution rather than the amplitude of heterogeneity. In the construction of the next generation of models, researchers should attempt to get amplitudes right, and the publication of data misfit versus model norm tradeoff statistics should become standard operating procedure. It would be a sad indictment of global seismology if 5 years hence we were still debating model amplitudes without the raw materials published to adjudicate the debate.

9.2. Construction of a Priori Reference Models

Approximately 50% of the difference between the models SH.10c.17 and S12_WM13 in the upper mantle is attributable to a difference in the a priori crustal corrections applied to each. This results in about a 25% rms variation between these aspherical models across the upper mantle. When this is added to the potential bias caused by topography on internal upper mantle boundaries (perhaps another 25%), a significant error results in the radial and geographical distribution of heterogeneity which could be avoided through the use of better a priori reference models. Consequently, it should become a priority within the global seismological community to construct a reference crustal model, and perhaps a lithospheric slab model, in the same way that collaborations have been forged to construct reference spherical models over the past decades. In addition, as models of topography on internal mantle boundaries continue to improve from studies of precursory phase conversions [e.g., *Shearer and Masters*, 1992; *Shearer*, 1993], internal topographic "corrections" similar to the crustal correction should be considered.

9.3. Summary Data

Current global seismic models have been produced by competing groups at a few institutions largely independent of collaboration with researchers at other institutions. In a sense, this independence and parallelism has made the comparisons performed in this

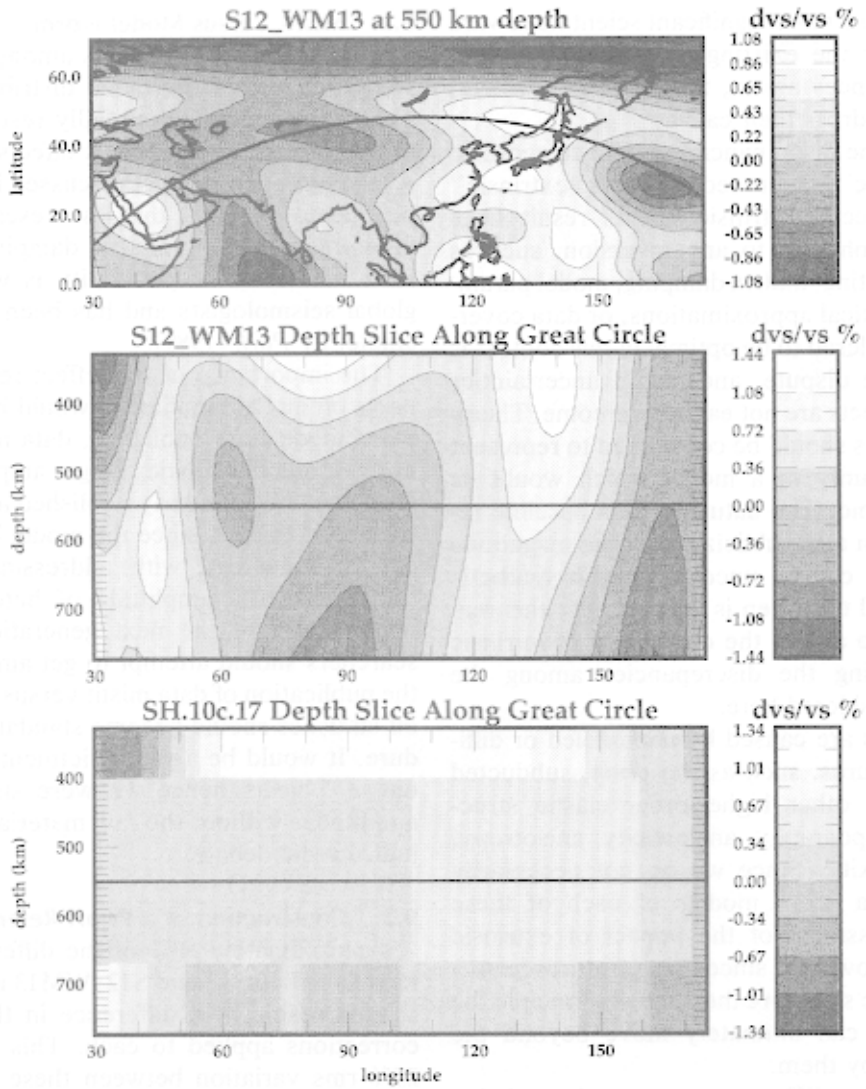

Figure 29. (top) S12_WM13 at 550-km depth beneath Eurasia. (middle) Cross section of S12_WM13 under the great circle plotted in the top panel. (bottom) Cross section of SH.10c.17 under the great circle plotted in the top panel.

review article meaningful. However, it makes simulation and testing of the models difficult to perform, both because the forward and inverse modeling algorithms are not generally available and also because the large waveform stores at these institutions are difficult to accumulate.

As long as seismic data are observed on the Earth's surface, they provide at each frequency (normal modes) or range (body waves) constraints only on (approximately) two of the Earth's three dimensions. The inherent two dimensionality of seismic data is evidenced by the splitting functions, which themselves are two-dimensional functions. The three-dimensional models are made possible by combining data from different frequencies and/or ranges to estimate the third dimension. Since the models agree better in the geographical than in the radial distribution of heterogeneity, the radial differences among the models have originated in attempts to infer the third dimension. A consequence of this is that the models themselves are historical entities unlike the data, which, if carefully observed and reduced, are essentially timeless. Therefore in the long run, what may be more interesting than the models themselves are clever summaries of the data, such as normal mode structure coefficients, with which future models can be constrained and with which they can be compared.

The difficulty in assessing existing mantle models by testing their fit to the data has been partially mitigated by the continuing policy of the Scripps group to publish the normal mode structure coefficients along with the models that fit the coefficients. Without these "summary data" the determination of the fit of each of these models to any class of data would have taken the years that it took these groups to individually compile the waveform data sets they employed in their inver-

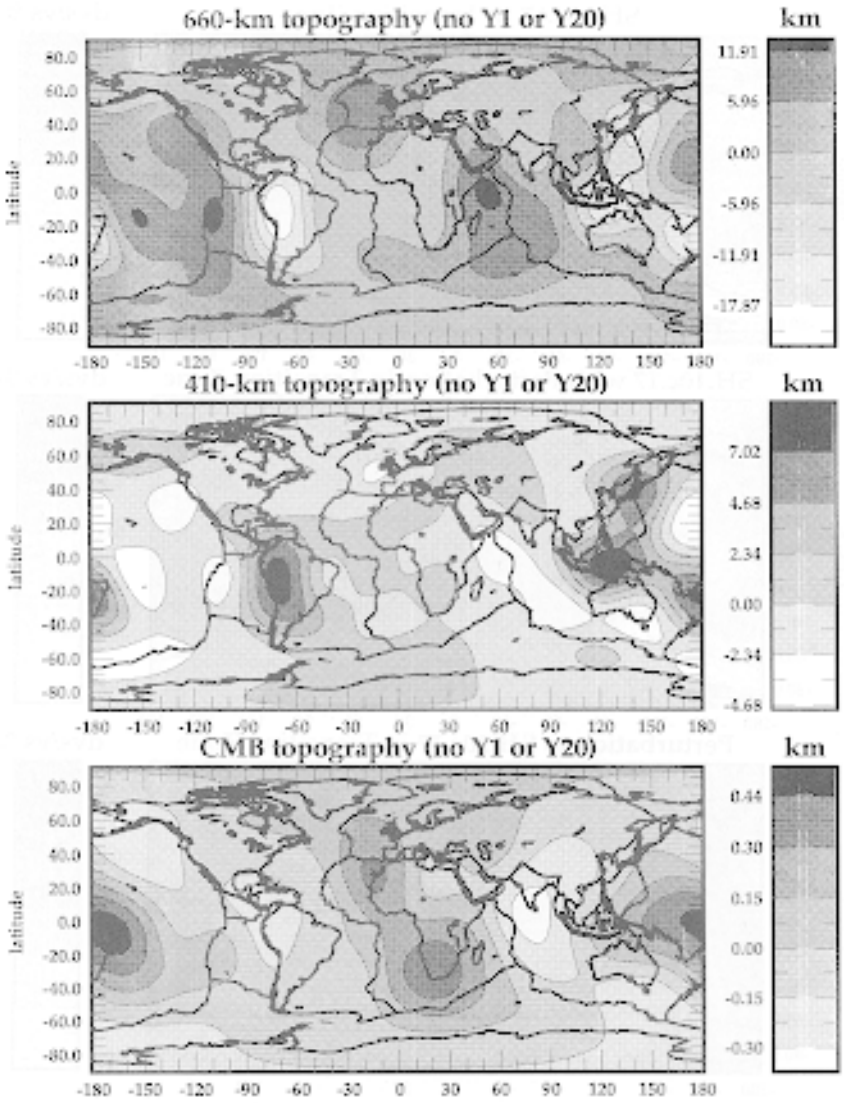

Figure 30a. Topography on three internal mantle discontinuities estimated by a "geodynamically consistent inversion" for boundary topography and volumetric structure [*Ritzwoller and Wahr*, 1994]. Units are kilometers. Positive topography is radially outward.

sions. Therefore models such as those discussed here could not as easily be held up to public scrutiny (e.g., this manuscript), and the significance of the differences among the models could not have been ascertained. In addition, the published coefficients have made possible the inferences concerning 660-km boundary topography in section 7.3 here and those of *Lavely et al.* [1994]. In a recent study, *Su et al.* [1992] found a way of summarizing differential body wave travel time data in a manner similar to structure coefficients.

For these reasons and others the continued publication of both improved elastic and anelastic normal mode structure coefficients and other summary data should be an increasing priority for global seismologists.

9.4. Joint Boundary-Volumetric Inversions and Geodynamical Consistency

We have discussed here and elsewhere [*Ritzwoller and Lavely*, 1994; *Lavely et al.*, 1994] how topography on internal boundaries can bias estimates of volumetric structure in the neighborhood of those boundaries. This observation is important for two principal reasons. First, the existence and nature of boundary layer structures hold a key to questions concerning the interaction of convection cells with the boundaries; in particular, they have implications concerning the large-scale dynamics and chemical stratification of the mantle. Second, in the neighborhood of certain (at least potential) boundary layers, such as the 660-km discontinuity, the models tend to disagree. Let us consider two examples of why structural estimates in

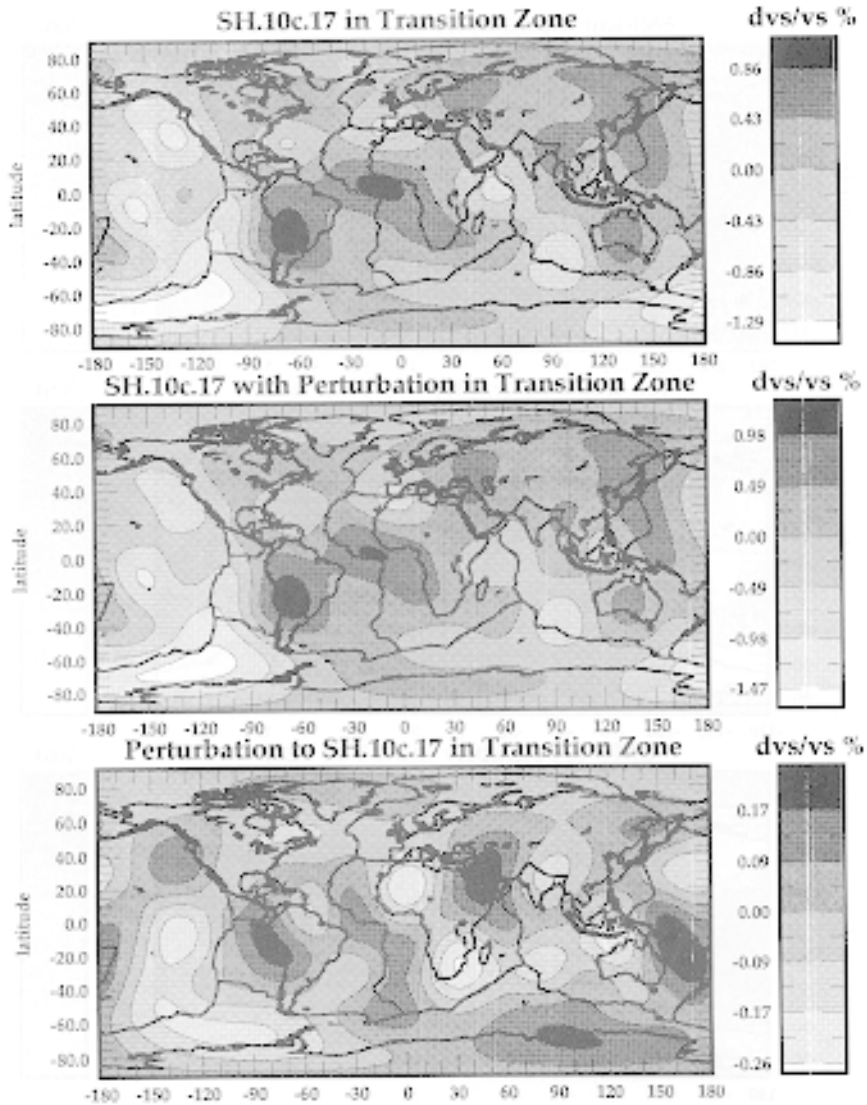

Figure 30b. (top) Transition Zone structure from SH.10c.17. (middle) New model of structure in the Transition Zone estimated by the geodynamically consistent inversion. (bottom) Perturbation to SH.10c.17 represented by the middle panel. Units are $\delta v_s/v_s$ in percent.

the neighborhood of the 660-km boundary are interesting and are worthy of future concentration.

First, Figure 29 displays a depth slice in and around the Transition Zone for the models S12_WM13 and SH.10c.17. The models display both qualitative and quantitative similarity in this slice, although the spherically layered parameterization of SH.10c.17 gives this model a blocky appearance. Nevertheless, the models differ in an important sense. Under central Asia, there is a low-velocity, plumelike feature in S12_WM13 that appears to ascend from the lower mantle and pierce the 660-km discontinuity. At shallower depths this feature does not exist, but as depth increases it appears and merges with lower velocities associated with the Indian Ridge farther to the south. Therefore S12_WM13 seems to predict in this region that low-velocity features, presumably plumes, pierce the 660-km boundary. However, SH.10c.17 is largely silent on this matter. Lower velocities exist in SH.10c.17 below the 660-km boundary, but it is not clear whether they pierce or turn at the boundary. This interpretative discrepancy and undoubtedly many others in other regions of the world are worth further detailed study.

Second, a new step in understanding the degree to which flows are stratified by phase transitions or changes in bulk chemistry in the Transition Zone and across the 660-km boundary has been taken by *Jordan et al.* [1993], who have introduced the use of the radial coherence of seismic Earth models to discriminate among competing mantle convection models. As was discussed in section 8, the geodynamical interpretatio of the radial correlation functions is nontrivial ano deserves further work. In particular, methods to estimate the intrinsic correlation length of 3-D models, taking into account the effects of model parameteriza-

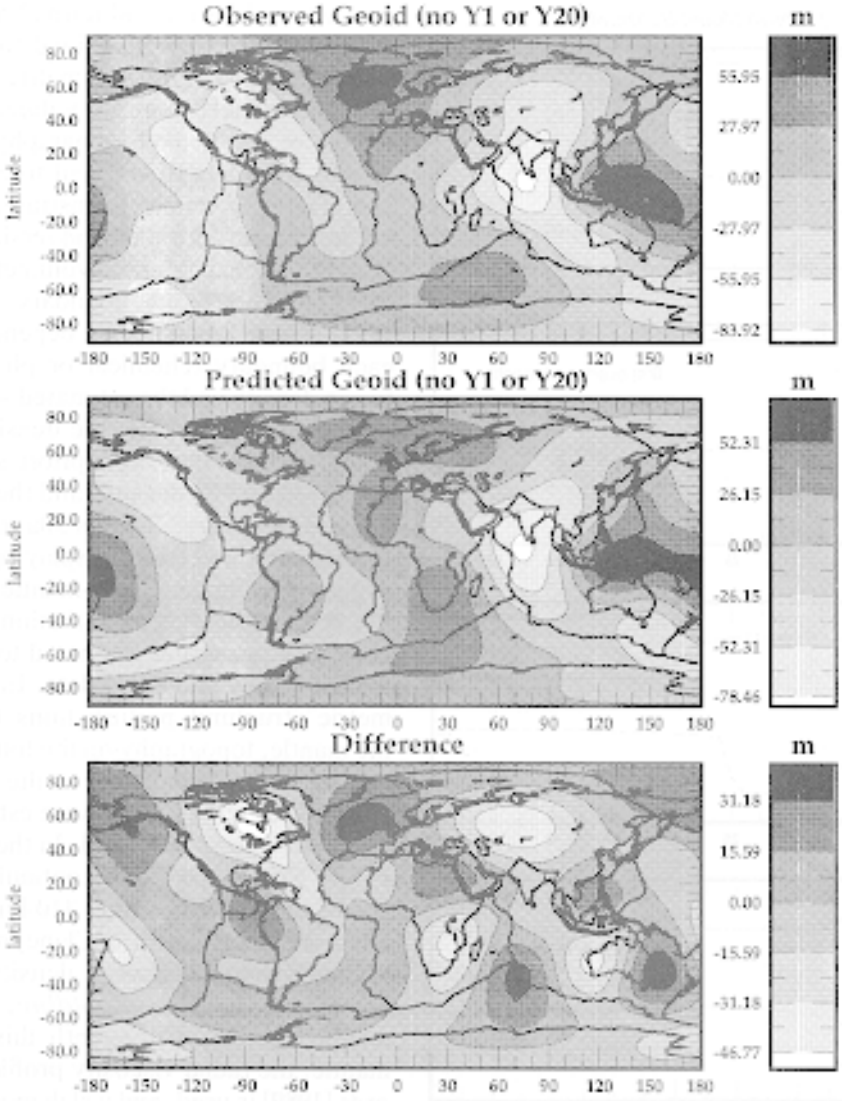

Figure 30c. (top) Observed geoid at degrees 2–8. The Y_2^0 term has not been included. (middle) Predicted geoid from the model estimated by the geodynamically consistent inversion. (bottom) Geoid residual, the difference between the observed and predicted geoids in the top and middle panel. Units are in meters.

tion, data type, and so forth, need to be developed. In addition, the dynamical interpretation of the decorrelation in three of the four models considered here across 1000-km depth warrants further examination. Are such decorrelations real, or might they be artifacts of the data and parameterizations employed? If they are real, are they diagnostic of dynamical contrasts at or near these depths, or are they merely structural variations unrelated to large-scale processes?

To overcome the bias caused by ignoring boundary topography in estimating volumetric structure, inversions for volumetric and boundary structures need to be performed simultaneously. The relevant seismic data include body waves that turn directly above the boundary, long-period, normal mode structure coefficients sensitive to the boundary, and body wave topside or bottomside reflections and reverberations. These are all difficult data to deal with accurately. Body waves that turn in and directly below the Transition Zone are characterized by a complicated triplication that makes the association of a measured travel time with a ray path difficult. This is presumably the reason why data for body waves that turn near the 660-km discontinuity are usually culled from data sets used in global inversions. Most of the fundamental spheroidal normal mode data that possess significant sensitivity to the 660-km boundary ($_0S_{10}$–$_0S_{25}$) are strongly coupled to nearby toroidal modes, and these data have not been used in constructing any of the global models considered here except SH.10c.17. Many overtone multiplets are also sensitive to these boundaries, but relatively few observations have been made to date because these modes are excited well only by the rare, large deep earthquake. Finally, waves reflected from the Transition Zone boundaries have low amplitudes, and stacking procedures are re-

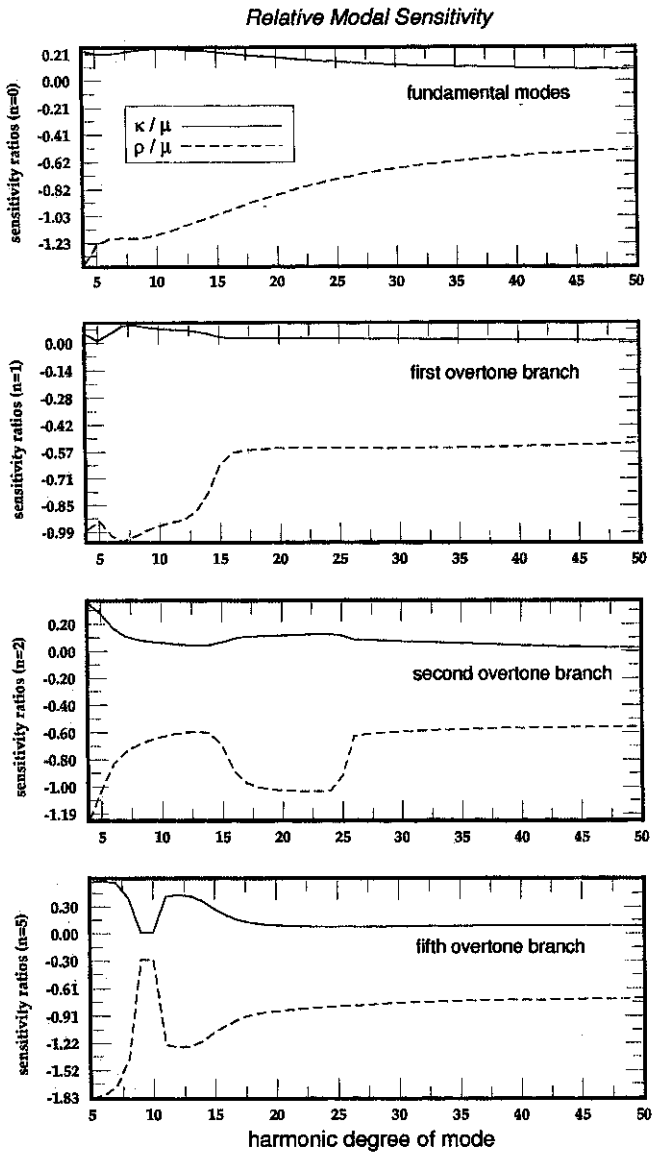

Figure 31. Same as Figure 22, but for structural perturbations in κ (solid) and ρ (dotted) relative to perturbations in μ. In the (δμ, δκ, δρ) representation, normal modes are dominantly sensitive to perturbations in μ, somewhat less sensitive to perturbations in ρ, and virtually insensitive to perturbations in κ (with the exception of lower-l and higher-n modes).

quired to pull the signals from the noise. The technical means for overcoming these complications exist.

Other data can be brought to bear on the problem of estimating volumetric and topographic structures simultaneously: e.g., geoid data, gravity data, plate motions, etc. Studies aimed at utilizing all of these data have been performed, for example, by *Forte et al.* [1993]. A more recent development is that geodynamical estimates of boundary topography are being performed simultaneously with seismic structural inversions [*Forte et al.*, 1994; *Ritzwoller and Wahr*, 1994].

Ritzwoller and Wahr [1994] inverted geoid and long-period mantle wave and normal mode data for mantle models which are constrained to lie in the neighborhood of an existing volumetric mantle model. Th resultant models comprise volumetric structure across the entire mantle and topography on four boundaries (CMB, 660 km, 410 km, and free surface). The application of geodynamical constraints to estimate boundary topography during the inversion is based on partial derivatives that relate a volumetric heterogeneity to topography on each boundary [*Dehant and Wahr*, 1991]. These functions are dependent on the nature of each boundary (chemical or phase), the scaling between density and the estimated seismic velocities, the radial viscosity profile, the density jump across each boundary, whether an a priori slab model has been employed and its density, and the Clapeyron slope for a phase boundary. Figures 30a to 30c show the result of one such inversion, displaying topography on the 400-km, 660-km, and core-mantle boundaries, the fit to the geoid, and the perturbation to Transition Zone volumetric structure estimated to improve the joint fit to the seismic and geoid data. In this inversion, volumetric structural perturbations to SH.10c.17 across the mantle, topography on the four mantle boundaries, and the radial dependence of the scaling between density and seismic velocity were estimated, but the other free parameters were fixed. In the realization shown in Figure 30, the 660-km discontinuity is assumed to be chemical boundary, the 410-km discontinuity is a phase boundary with a Clapeyron slope of 2.5, the scaling relations between density and shear velocity are estimated to be $d\ln\rho/d\ln v_s \approx 0.4$ in the upper mantle and about one-tenth this value in the lower mantle, the radial viscosity profile of *Hager and Richards* [1989] is used, and a slab model has been added in the upper mantle with a maximum density contrast of about 0.2 g cm^{-3}. The slab model is added to the density model derived from 3-D seismic models. *Ritzwoller and Wahr* [1994] also report on results of inversions in which the 660-km discontinuity is a phase boundary. Confidence in topographic models such as these will ultimately depend on improved confidence in the fixed parameters. *Ricard et al.* [1993] appear to have made a significant advance by constructing a new slab model which incorporates information about the time history of the plate tectonics.

9.5. Long-Period Data

The sensitivity to topography on internal mantle boundaries is only one of the reasons for the continued use and emphasis of interpretation on long-period seismic data in the construction of future three-dimensional mantle models. Long-period data are complementary to body wave data in a number of way including a higher signal-to-noise ratio on average, a relative insensitivity to short-wavelength structures, a sensitivity to density at the lowest frequencies, the ease with which the data can be summarized into

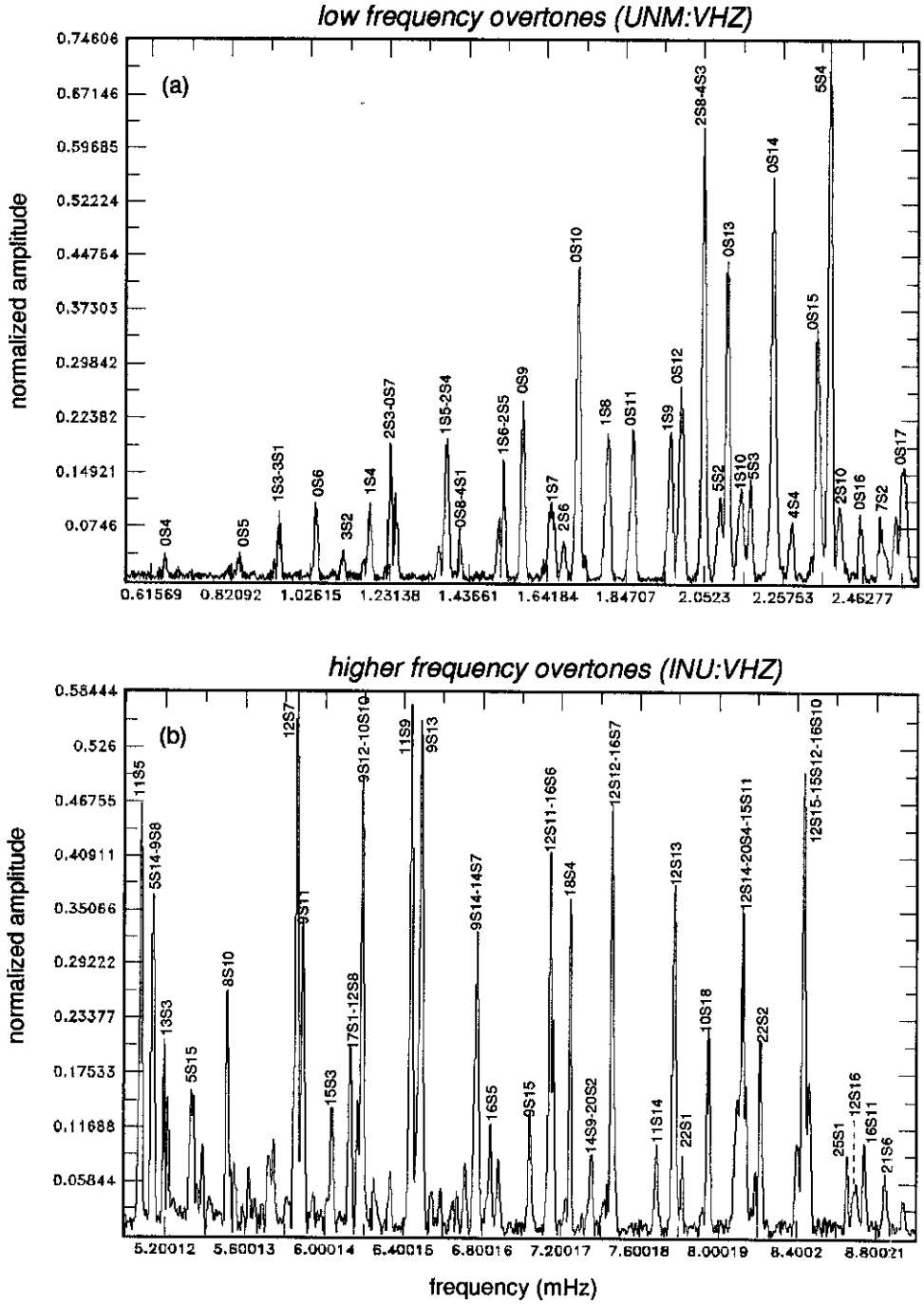

Figure 32. Normal mode spectra from the large, deep event in northern Bolivia on June 9, 1994 (0033:13 UT, 13.7°N, 67.4°W, 600 km, m_b = 7.8, M_s = 7.8, M_0 = 3.0 × 10^{28}). (a) Hann tapered spectrum for a time series recorded on the very long period vertical channel at the Geoscope station at the Universidad Nacional Autónoma de México, Mexico City. The time series starts 10 hours after the event, is 100 hours long, and displays many overtones sensitive to the lower mantle. (b) Same as Figure 32a, but the time series is recorded at Inuyama, Japan, is only 45 hours in duration, and displays higher frequency overtones, many of which possess considerable sensitivity to the very deep mantle and core. A number of these modes have never been observed on digital recordings prior to this event.

ıodel constraints (e.g., normal mode structure coefficients), their straightforward sensitivity to anelasticity, and (perhaps chiefly) their strong sensitivity to middle and lower mantle structures.

Many multiplets possess significant sensitivity to the Transition Zone and the several hundred kilometers directly below the Transition Zone where the models considered here differ most appreciably. It was only in the construction of SH.10c.17 that fundamental normal mode data with harmonic degrees $l < 20$ were

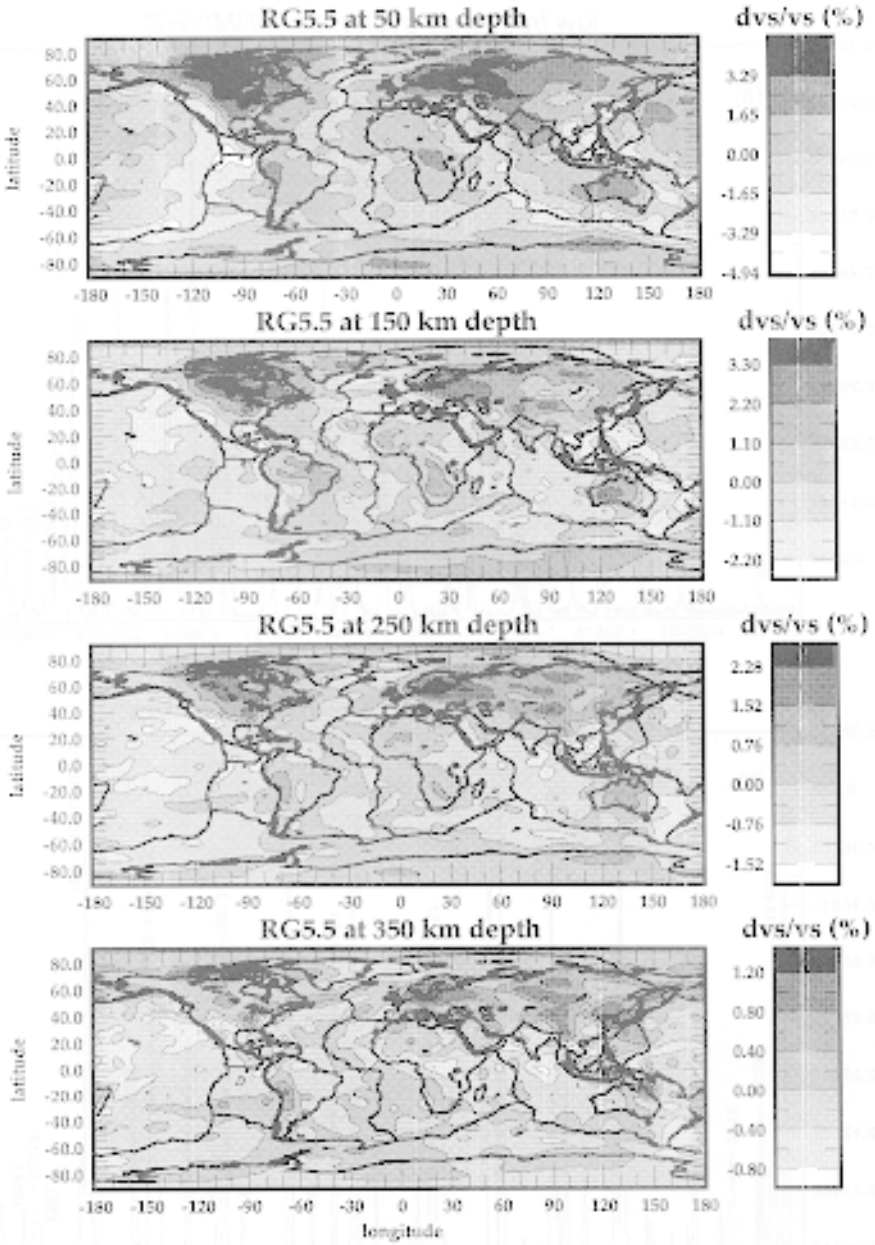

Figure 33. Depth slices from the model RG5.5 of *Zhang and Tanimoto* [1993]. This model is represented identically to slices of other models shown in Figures 4a to 4h but contains considerably shorter wavelength features up to spherical harmonic degree and order 36.

employed, presumably owing to the complexity of the normal mode signal at lower frequencies due to Coriolis coupling between spheroidal and toroidal modes. Constraints from these multiplets and those from the overtone normal modes sensitive to the lower mantle should receive more general use in the future.

Some long-period normal mode data also differ from body waves in their sensitivity to density. As is shown in Figure 31, most multiplets possess dominant sensitivity to perturbations in shear modulus, very small sensitivity to bulk modulus, and significant sensitivity to perturbations in density. This suggests that if it were possible to break the scaling between two of the three parameters to which seismic data are sensitive, then a natural pair would be the shear modulus and density, and that it may be possible to constrain $\delta\rho$ in addition to $\delta\mu$. The combination of these models, constructed with a reference slab model and geoid constraints, could provide information that would be of great geodynamical interest.

The addition of long-period data to body wave data also improves radial resolution across the mantle. Th fact can be seen in Figure 27. Only body wave differential travel times were used in the construction of the odd degree components of SH.10c.17. Long-period Rayleigh and Love waves and normal mode data were

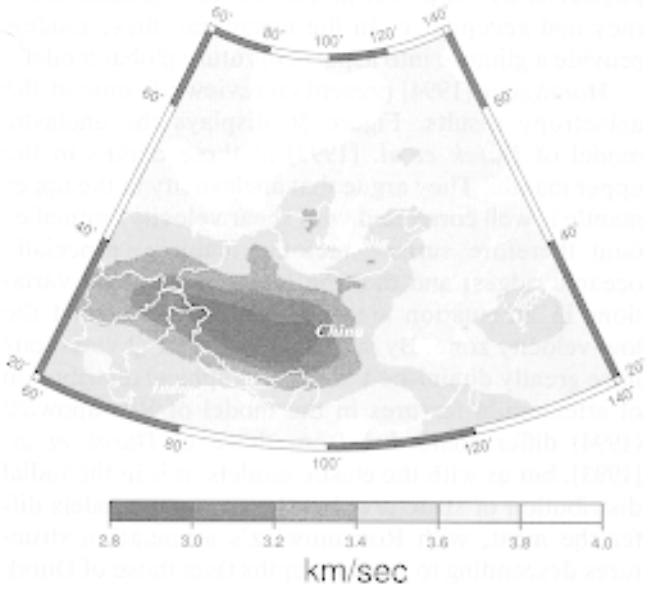

Figure 34. Regional group velocity map at 50-s period from *Wu and Levshin* [1994].

added in the construction of the even degree parts of the model. This is the reason that the radial resolution is so much better at even degrees than at odd degrees.

The utility of normal mode data to estimating lower mantle structure has been improved recently by the large, deep earthquake that occurred on June 9, 1994, at about 600-km depth beneath northern Bolivia. Figure 32 shows long-period spectra from two vertical component recordings. Many of the overtone modes seen in Figure 32b have never been observed before on single digital recordings. This opens an exciting new window on deep Earth structure.

To improve both volumetric and topographic models in and around the Transition Zone and in the lower mantle and core, long-period normal mode data deserve renewed concentration.

9.6. Shorter-Wavelength Structures, Regional Data, and Models

The fact that early global models have been restricted to long wavelengths has made good sense; the Earth's spectrum of heterogeneity is enriched at the longer wavelengths, and data fits can be greatly improved with relatively few structural parameters. Nevertheless, future generations of seismic models should be focused to shorter wavelengths, both to provide improved fits to seismic data (in particular surface wave amplitudes) and to produce information about smaller-scale features of tectonic relevance. Global upper mantle models have begun to move in this direction. *Zhang and Tanimoto* [1993, 1994] have produced a global upper mantle model, RG5.5, expanded to degree and order 36. Figure 33 presents some depth slices of RG5.5. Although some features of this model are contentious (e.g., *Su et al.* [1992]), it marks the beginning of a useful trend.

To improve confidence in future models, global models need to be compared with and to incorporate the results of more detailed studies of complex regions such as subduction zones and continental deformation regions. In particular, summary data sets, such as group velocity maps from regional studies, should be utilized, as should measurements of polarization anomalies. Figure 34 displays a group velocity map at 50-s period from the study of *Wu and Levshin* [1994] produced from a seismic study of China. Because of shorter path lengths and the use of historical data, this study does a much better job of resolving features in western China than global studies do. This focused picture of structure under Tibet differs appreciably from the global models, as a comparison with Figure 4a reveals.

Polarization measurements possess sensitivity to shorter-wavelength features near the Earth's surface than the phase information that has been used to construct the current generation of global 3-D models. Figure 35 displays polarization measurements made for a path across central Asia. Measurements such as these are not well fit by global mantle models and can be used to help focus the long-wavelength models to shorter wavelengths [e.g., *Levshin et al.*, 1992, 1994; *Politz and Hennet*, 1993], and are now beginning to be incorporated in global model construction [*Laske and Masters*, 1993].

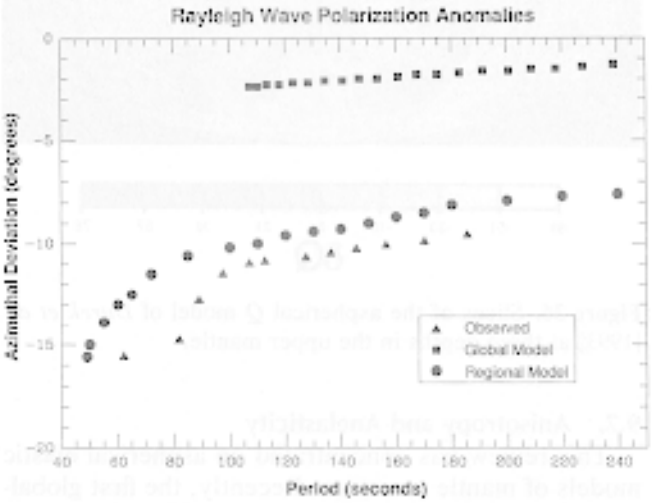

Figure 35. Observed and predicted Rayleigh wave polarization anomalies at Kislovodsk, Russia, for an event in the Kuril Islands. M84C predicts the right sign for the polarization anomalies but does not predict the correct magnitude. The addition of a regional model containing a model of the Caspian sedimentary depression and a regional north-south gradient in lithospheric shear velocity allows the polarization anomalies to be fit approximately.

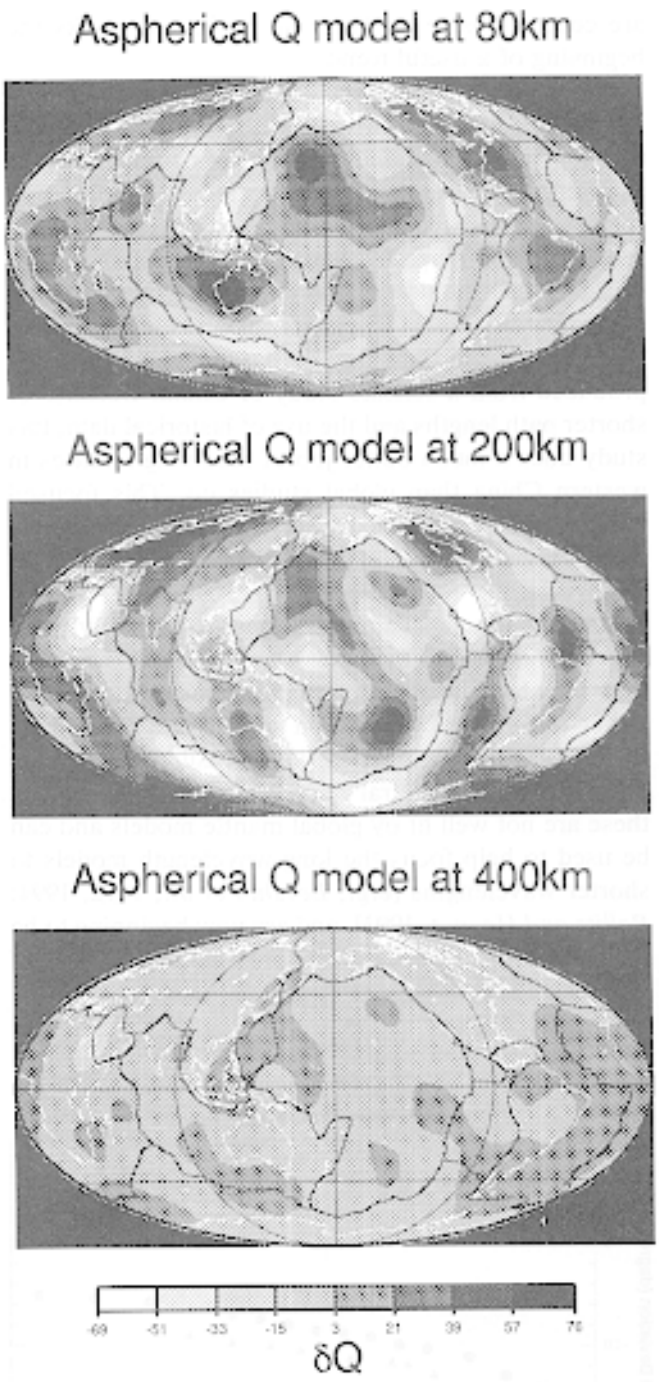

Figure 36. Slices of the aspherical Q model of *Durek et al.* [1993] at three depths in the upper mantle.

9.7. Anisotropy and Anelasticity

This review has concentrated on aspherical elastic models of mantle structure. Recently, the first global-scale images of anisotropy [*Montagner and Tanimoto*, 1990, 1991] and anelasticity [*Romanowicz*, 1990; *Durek et al.*, 1993; B. A. Romanowicz, A global tomographic model of shear attenuation in the upper mantle, submitted to *Journal of Geophysical Research*, 1994, hereinafter referred to as Romanowicz (1994)] in the upper mantle have emerged. Both structures should become increasingly interesting to geophysicists as the global models achieve greater accuracy and acceptance. In the meantime, these models provide a glimpse into aspects of future global model

Montagner [1994] presents a review of some of the anisotropy results. Figure 36 displays the anelastic model of *Durek et al.* [1993] at three depths in the upper mantle. They argue that anelasticity in the upper mantle is well correlated with shear velocity anomalies (and therefore surface tectonic features, especially oceanic ridges) and that the largest magnitude variations in attenuation are centered in and around the low-velocity zone. By 400-km depth their Q variations have greatly diminished. The geographical distribution of attenuation features in the model of Romanowicz (1994) differ somewhat from those of *Durek et al.* [1993], but as with the elastic models, it is in the radial distribution of structure that the anelastic models differ the most, with Romanowicz's attenuation structures descending to greater depths than those of Durek et al. The implications of these differences among the first round of anelastic models are great, and the construction of increasingly sophisticated and improved anelastic models should be a high priority. Further discussion must await another review article.

APPENDIX A: NORMAL MODE AND SURFACE WAVE NOTATION AND TERMINOLOGY

In this section, the normal mode notation and terminology used throughout the paper is defined. A seismic mode of oscillation of any Earth model is defined to be a characteristic spatial displacement pattern that oscillates with a single frequency. A mode of a spherically symmetric reference Earth model such as PREM [*Dziewonski and Anderson*, 1981] is typically identified by the trio of quantum numbers (n, l, m), where n, l, and m denote the radial order, spherical harmonic degree, and azimuthal order of the mode, respectively. The geographic dependence of the displacement pattern is defined by the spherical harmonics $Y_l^m(\theta, \phi)(-l \leq m \leq l)$, and the radial dependence is defined by the radial eigenfunctions of the modes. Because of the complete rotational symmetry of the spherically symmetric model, the modes of oscillation are $2l + 1$ degenerate. That is, the frequencies of the $2l + 1$ modes with different m values but with the same n and l values are identical. These modes are said to form a multiplet, which is commonly denoted by ${}_nS_l$ for spheroidal modes and by ${}_nT_l$ for toroidal modes. Multiplets for which $n = 0$ are called fundamental modes; if $n > 0$, the multiplet is an overtone. Spheroidal fundamental multiplets are called Rayleigh waves, and toroidal fundamental multiplets are Love waves. Very long period Rayleigh and Love waves (periods $> 100s$) are sometimes referred to as mantle waves, since they are not confined to the region near

the Earth's surface. The identification $k = (n, l)$ is often made.

The spheroidal modes of the spherically symmetric reference Earth model may be written in the form

$$\mathbf{s}_k(\mathbf{r}, t) = [{}_nU_l(r)Y_l^m(\theta, \phi)\hat{\mathbf{r}} + {}_nV_l(r)\nabla_1 Y_l^m(\theta, \phi)]e^{i\omega_k t}, \quad \text{(A1)}$$

where ${}_nU_l(r)$ and ${}_nV_l(r)$ are the scalar radial eigenfunctions for harmonic degree l and radial order n which denotes the number of zero crossings of the normal component of the radial eigenfunction with depth. The coordinates (r, θ, ϕ) are spherical polar coordinates (where θ is colatitude), $\hat{\mathbf{r}}$ is the radial unit vector, and ∇_1 denotes the surface gradient operator. The toroidal modes of the reference model may be written in the form

$$\mathbf{s}_k(\mathbf{r}, t) = -\hat{\mathbf{r}} \times \nabla_1 {}_nW_l(r)Y_l^m(\theta, \phi)e^{i\omega_k t}, \quad \text{(A2)}$$

where ${}_nW_l(r)$ is the toroidal radial eigenfunction.

Of course, the real Earth is not spherically symmetric. Any symmetry-breaking agent such as rotation or volumetric or topographic perturbations will lift the $(2l + 1)$ degeneracy and split the frequencies of the modes or singlets composing the multiplet. In normal mode seismology, perturbation theory [*Woodhouse and Dahlen*, 1978; *Woodhouse*, 1980] is usually employed to calculate the modal eigenfrequencies and eigenfunctions of a perturbed model. The modes (k, m) and (k', m') of a spherically symmetric Earth model satisfy an orthogonality condition, but the inner product of these modes in a perturbed model is nonzero. This is referred to as modal coupling.

Concentration in this paper is on results from degenerate perturbation theory, which is used to model coupling between two modes of the reference model that share the same n and l values, i.e., that have the same degenerate frequency. Discussion of the more general case of quasi-degenerate perturbation theory $(k' \neq k)$ is given by *Woodhouse* [1980]. Under degenerate perturbation theory the strength of coupling between modes (k, m) and (k, m') is expressed in terms of the (m', m) component of the splitting or general matrix $\mathbf{H}_{kk}$ and can be written

$$H_{kk}^{m'm} = \int \mathbf{s}_k^{m'*} \cdot \delta\mathcal{L}(\mathbf{s}_k^m)\, d^3\mathbf{r} + \sum_d M_d(\mathbf{s}_k^{m'*}, \mathbf{s}_k^m), \quad \text{(A3)}$$

where $\delta\mathcal{L}$ is a perturbation operator that describes aspherical volumetric perturbations, and M_d accounts for topography on the free surface and internal boundaries d. Typically, the perturbation is expanded in terms of spherical harmonics with harmonic degree s and azimuthal order t. This leads to an expression for $H_{kk}^{m'm}$ (equation (6)) given by the product of a radial integral, denoted by ${}_kc_s^t$ (equation (7)), and the result of an angular integration of three spherical harmonics over the unit sphere, denoted by $\gamma_s^{m'm}$; $\gamma_s^{m'm}$ can be expressed in terms of the well-known Wigner 3-j symbols. Each structure or interaction coefficient ${}_kc_s^t$ represents an integral of the radially dependent (s, t) component of seismic (elastic and anelastic) Earth structure weighted by the modal eigenfunctions and a sum over boundary contributions, as shown in (7). The volumetric component of the structure coefficient can be written

$${}_k\tilde{c}_s^t = \int_0^a \left[{}_kM_s(r)\frac{\delta\mu_s^t(r)}{\mu(r)} + {}_kK_s(r)\frac{\delta\kappa_s^t(r)}{\kappa(r)} + {}_kD_s(r)\frac{\delta\rho_s^t(r)}{\rho(r)} \right] dr, \quad \text{(A4)}$$

where ${}_kM_s(r)$, ${}_kK_s(r)$, and ${}_kD_s(r)$ denote the sensitivity kernels for relative perturbations to the shear modulus μ, the adiabatic bulk modulus κ, and the density ρ given by *Woodhouse and Dahlen* [1978], respectively. The structure coefficient can also be expressed in terms of perturbations to the seismic velocities:

$${}_k\tilde{c}_s^t = \int_0^a \left[{}_kS_s(r)\frac{(\delta v_s(r))_s^t}{v_s(r)} + {}_kP_s(r)\frac{(\delta v_p(r))_s^t}{v_s(r)} + {}_kR_s(r)\frac{\delta\rho_s^t(r)}{\rho(r)} \right] dr, \quad \text{(A5)}$$

where ${}_kS_s(r)$, ${}_kP_s(r)$, and ${}_kR_s(r)$ denote the sensitivity kernels for relative perturbations to the shear velocity, the compressional velocity, and the density, respectively. In terms of the fundamental kernels in (A4), these kernels can be written as

$$\begin{aligned} {}_kS_s(r) &= 2\mu_k\tilde{M}_s(r) - 8/3\mu_k\tilde{K}_s(r), \\ {}_kP_s(r) &= (2\kappa + 8/3\mu)_k\tilde{K}_s(r), \\ {}_kR_s(r) &= \rho_k\tilde{D}_s(r) + \mu_k\tilde{M}_s(r) + \kappa_k\tilde{K}_s(r), \end{aligned} \quad \text{(A6)}$$

where $\tilde{M} = M/\mu$, $\tilde{K} = K/\kappa$, and $\tilde{D} = D/\rho$. The structure coefficients are gross Earth data which are radially averaged measures of Earth structure, much like geoid coefficients or seismic travel times. Since these coefficients are linearly related to the Earth structure causing the observed normal mode splitting and coupling, they are the data we wish to estimate to constrain aspherical structure from normal mode data.

The modes of oscillation of the aspherical Earth model are represented as linear combinations of the modes of the spherical reference model. The expansion coefficients are the components of the eigenvectors of the splitting matrix, and the frequencies of the modes are defined by the eigenvalues of the splitting matrix. The degree of coupling between modes of the reference model is a function of a number of factors, among which are the strength of the asphericity pro-

ducing the coupling as represented by ${}_kc_s^t$, the proximity of the eigenfrequencies of the coupled modes (which is important in quasi-degenerate coupling), and the relation between the geometries of the perturbation and the oscillations, which is encoded in a set of analytical angular selection rules and expressed in $\gamma_s^{m'm}$.

Theoretical, computational, and review papers on normal mode and long-period surface wave seismology, with a concentration on recent studies, that the reader may find useful include those of *Takeuchi and Saito* [1972], *Gilbert and Dziewonski* [1975], *Jordan* [1978], *Woodhouse and Dahlen* [1978], *Dahlen* [1980, 1987], *Woodhouse* [1980], *Woodhouse and Girnius* [1982], *Dahlen and Henson* [1985], *Lay and Kanamori* [1985], *Henson and Dahlen* [1986], *Park and Gilbert* [1986], *Romanowicz and Roult* [1986], *Woodhouse and Wong* [1986], *Masters and Ritzwoller* [1988], *Park* [1987], *Romanowicz* [1987], *Snieder and Nolet* [1987], *Snieder and Romanowicz* [1988], *Masters* [1989], *Woodhouse and Dziewonski* [1989], *Tanimoto* [1990b], *Lognonne and Romanowicz* [1990], *Lognonne* [1991], *Um and Dahlen* [1991, 1992], *Pollitz* [1992], *Tromp and Dahlen* [1992a, b], *Lavely and Ritzwoller* [1993], *Li and Tanimoto* [1993], *Resovsky and Ritzwoller* [1994], *Geller and Hara* [1993], *Geller and Ohminato* [1994], and *Cummins et al.* [1994].

APPENDIX B: THE CORIOLIS COUPLING CORRECTION

Masters et al. [1983] showed that Coriolis coupling between spheroidal multiplets ${}_0S_l$ and toroidal multiplets ${}_0T_{l+1}$ can significantly perturb the diagonal components of the splitting matrix of certain multiplets, which are manifested as perturbations to the ${}_kc_0^0$ and ${}_kc_2^0$ seismic structure coefficients. These coefficients constrain spherically symmetric and degree 2 axisymmetric Earth structure. The structure coefficients that are strongly contaminated by Coriolis coupling are very sensitive to structure in the Transition Zone and lower mantle.

Smith and Masters [1989b] showed that the Coriolis coupling perturbation to the splitting matrix can be modeled using the subspace projection formalism of *Park* [1987]. By equating like powers of the azimuthal order m between equation (5) of *Smith and Masters* [1989b] and the splitting matrix (our equation (6)), it follows that the Coriolis perturbation to the structure coefficients ${}_kc_0^0$ and ${}_kc_2^0$ for the spheroidal multiplet ${}_0S_l$ are given, respectively, by

$$\delta_k c_0^0 = -\frac{2\omega_S}{\omega_T^2 - \omega_S^2}\left(\frac{4\pi}{9}\right)^{1/2}\frac{l}{(2l+1)}\Omega^2 \cdot\left[\int_0^a \rho(r)C_k^+(r)r^2\,dr\right]^2, \tag{A7}$$

$$\delta_k c_2^0 = -\frac{2\omega_S}{\omega_T^2 - \omega_S^2}\left(\frac{4\pi}{45}\right)^{1/2}\frac{2l+3}{(2l+1)}\Omega^2 \cdot\left[\int_0^a \rho(r)C_k^+(r)r^2\,dr\right]^2, \tag{A8}$$

where a is the radius of the Earth, Ω is the Earth's rotation rate, $C_k^+(r)$ is the Coriolis coupling kernel of *Woodhouse* [1980] and can be computed from spherically symmetric quantities alone, and ω_T and ω_S denote the toroidal and spheroidal angular frequencies, respectively. These corrections assume that the normalization integral defined by *Woodhouse* [1980] is equal to $1/2\omega$ rather than unity as Woodhouse assumes, and that the spherical harmonics are normalized following *Edmonds* [1960]. Equations (A7) and (A8) should be multiplied by $4\omega_{\text{ref}}^2$ to be consistent with the normalization convention of *Woodhouse* [1980], where ω_{ref} is the reference frequency $(\omega_S + \omega_T)/2$. The shift to the degenerate frequency is given by $\delta_k c_0^0/(4\pi)^{1/2}$.

Equations (A7) and (A8) break down for profoundly coupled multiplet pairs such as ${}_0S_{11}$–${}_0T_{12}$, and ${}_0S_{19}$–${}_0T_{20}$. For these multiplet pairs the fully coupled problem must be solved exactly following *Woodhouse* [1980], and the corrections $\delta_k c_0^0$ and $\delta_k c_2^0$ are obtained by numerically fitting the perturbed frequencies. Equations (A7) and (A8) show that ${}_kc_0^0$ and ${}_kc_2^0$ a[illegible] depressed by Coriolis coupling if ω_T is greater than $\omega_[illegible]$ and are shifted positively if ω_T is less than ω_S, and that the correction is strongly dependent on the nearness to degeneracy of the modes.

ACKNOWLEDGMENTS. We thank Wei-jia Su for sending a manuscript prior to publication and for supplying the model coefficients of S12_WM13, Guy Masters for providing the coefficients of SH.10c.17, and Harold Bolton for providing the coefficients of the Scripps crustal model. We would also like to thank the Scripps group, under the direction of Guy Masters, for their continuing policy of publishing normal mode structure coefficients and other summary data, which enabled the data comparison parts of this paper to be performed. Larry Ruff and Jeff Park provided insightful reviews of the manuscript, and the criticism of the students of Physics 6650 helped us to identify particularly turgid sections of the paper. Two anonymous referees and Thorne Lay also contributed helpful comments and criticisms. We are also grateful to John Wahr for many valuable conversations and to Anatoli Levshin, Joseph Resovsky, and Artie Rodgers for help in constructing some of the figures. E.M.L. was supported by a Ford Foundation Postdoctoral Fellowship and a CIRES Visiting Fellowship.

REFERENCES

Anderson, D. L., A seismic equation of state, II, Shear properties and thermodynamics of the lower mantle, *Phys. Earth Planet. Inter.*, *45*, 307–323, 1987.

Anderson, O. L., E. Schreiber, R. C. Lieberman, and M. Soga, Some elastic constant data on minerals relevant to geophysics, *Rev. Geophys.*, *6*, 491–524, 1968.

Anung, D. H., Elasticity and equations of state of olivines in the Mg_2SiO_4-$FeSiO_4$ system, *Geophys. J. R. Astron. Soc.*, *25*, 511–538, 1971.

Clayton, R., and R. Comer, A tomographic analysis of mantle heterogeneities from body wave travel time data (abstract), *Eos Trans. AGU*, *64*, 776, 1983.

Creager, K. C., and T. H. Jordan, Aspherical structure of the core-mantle boundary from PKP travel times, *Geophys. Res. Lett.*, *13*, 1497–1500, 1986.

Cummins, P. R., R. J. Geller, T. Hatori, and N. Takeuchi, DSM complete synthetic seismograms: SH, spherically symmetric, case, *Geophys. Res. Lett.*, *21*, 533–536, 1994.

Dahlen, F. A., Splitting of the free oscillations of the Earth, in Physics of the Earth's Interior, edited by A. M. Dziewonski and E. Boschi, *Proc. Enrico Fermi Int. Sch. Phys.*, *78*, 82–126, 1980.

Dahlen, F. A., Multiplet coupling and the calculation of synthetic long-period seismograms, *Geophys. J. R. Astron. Soc.*, *91*, 241–254, 1987.

Dahlen, F. A., and I. H. Henson, Asymptotic normal modes of a laterally heterogeneous Earth, *J. Geophys. Res.*, *90*, 12,653–12,681, 1985.

Davis, J. P., Local eigenfrequency and its uncertainty inferred from spheroidal mode frequency shifts, *Geophys. J. R. Astron. Soc.*, *88*, 693–722, 1987.

Dehant, V., and J. Wahr, The response of a compressible, nonhomogeneous Earth to internal loading: Theory, *J. Geomagn. Geoelectr.*, *43*, 157–175, 1991.

Doornbos, D. J., and T. Hilton, Models of the core-mantle boundary and the travel times of internally reflected core phases, *J. Geophys. Res.*, *94*, 15,741–15,751, 1989.

Durek, J., M. H. Ritzwoller, and J. H. Woodhouse, Constraining upper mantle anelasticity using surface wave amplitude anomalies, *Geophys. J. Int.*, *114*, 249–272, 1993.

Dziewonski, A. M., Mapping the lower mantle: Determination of lateral heterogeneity in *P* velocity up to degree and order 6, *J. Geophys. Res.*, *89*, 5929–5952, 1984.

Dziewonski, A. M., and D. L. Anderson, Preliminary reference Earth model, *Phys. Earth Planet. Inter.*, *25*, 297–356, 1981.

Dziewonski, A. M., and J. H. Woodhouse, Global images of the Earth's interior, *Science*, *236*, 37–48, 1987.

Dziewonski, A. M., and R. L. Woodward, Acoustical imaging at the planetary scale, *Acoust. Imaging*, *19*, 785–797, 1992.

Dziewonski, A. M., A. L. Hales, and E. R. Lapwood, Parametrically simple Earth models consistent with geophysical data, *Phys. Earth Planet. Inter.*, *10*, 12–48, 1975.

Dziewonski, A. M., B. H. Hager and R. J. O'Connell, Large scale heterogeneity in the lower mantle, *J. Geophys. Res.*, *82*, 239–255, 1977.

Dziewonski, A. M., A. M. Forte, W.-J. Su, and R. L. Woodward, Seismic tomography and geodynamics, in *Relating Geophysical Structures and Processes*, *Geophys. Monogr. Ser.*, vol. 76, edited by K. Aki and R. Dmowska, pp. 67–105, AGU, Washington, D. C., 1993.

Eckhardt, D. H., Correlations between global features of terrestrial fields, *Math. Geol.*, *16*, 155–171, 1984.

Edmonds, A. R., *Angular Momentum in Quantum Mechanics*, Princeton University Press, Princeton, N. J., 1960.

Forsyth, D. W., Geophysical constraints on mantle flow and melt generation beneath mid-ocean ridges, in *Mantle Flow and Melt Generation at Mid-Ocean Ridges*, *Geophys. Monogr. Ser.*, vol. 71, edited by J. Phipps Morgan, D. K. Blackman, and J. M. Sinton, pp. 1–67, AGU, Washington, D. C., 1992.

Forte, A. M., and R. Peltier, Viscous flow models of global geophysical observables, 1, Forward problems, *J. Geophys. Res.*, *96*, 20,131–20,159, 1991.

Forte, A. M., A. M. Dziewonski, and R. L. Woodward, Aspherical structure of the mantle, tectonic plate motions, nonhydrostatic geoid, and topography of the core-mantle-boundary, in *Dynamics of Earth's Deep Interior and Earth Rotation*, *Geophys. Monogr. Ser.*, vol. 72, edited by J.-L. Mouel, D. E. Smylie, and T. Herring, pp. 135–136, AGU, Washington, D. C., 1993.

Forte, A. M., R. L. Woodward, and A. M. Dziewonski, Joint seismic and geodynamic inferences of 3-D mantle structure, paper presented at symposium, Int. Assoc. Seismol. Phys. Earth's Inter., Wellington, New Zealand, 1994.

Garnero, E. J., and D. V. Helmberger, Travel times of *S* and *SKS*: Implications for three-dimensional lower mantle structure beneath the central Pacific, *J. Geophys. Res.*, *98*, 8225–8241, 1993.

Geller, R. J., and T. Hara, Two efficient algorithms for iterative inversion of seismic waveform data, *Geophys. J. Int.*, *115*, 699–710, 1993.

Geller, R. J., and T. Ohminato, Computation of synthetic seismograms and their partial derivatives for heterogeneous media with arbitrary natural boundary conditions using the direct solution method, *Geophys. J. Int.*, *116*, 421–446, 1994.

Giardini, D., X. Li, and J. H. Woodhouse, Three dimensional structure of the Earth from splitting in free oscillation spectra, *Nature*, *325*, 405–411, 1987.

Giardini, D., X.-D. Li, and J. H. Woodhouse, The splitting functions of long period normal modes of the Earth, *J. Geophys. Res.*, *93*, 13,716–13,742, 1988.

Gilbert, F., and A. M. Dziewonski, An application of normal mode theory to the retrieval of structural parameters and source mechanisms from seismic spectra, *Philos. Trans. R. Soc. London A*, *278*, 187–269, 1975.

Gogna, M. L., H. Jeffreys, and M. Shimshoni, Seismic travel times from central Asian epicentres, *Geophys. J. R. Astron. Soc.*, *63*, 577–599, 1980.

Gudmunsson, O., R. W. Clayton, and D. L. Anderson, Stochastic analysis of global travel time data: Mantle heterogeneity and random errors in the ISC data, *Geophys. J. Int.*, *102*, 25–43, 1990.

Hager, B. H., Subducted slabs and the geoid: Constraints on mantle rheology and flow, *J. Geophys. Res.*, *89*, 6003–6015, 1984.

Hager, B. H., and R. W. Clayton, Constraints on the structure of mantle convection using seismic observations, flow models, and the geoid, in *Mantle Convection: Plate Tectonics and Global Dynamics*, edited by W. R. Peltier, pp. 657–764, Gordon and Breach, New York, 1989.

Hager, B. H., and M. A. Richards, Long-wavelength variations in the Earth's geoid: Physical models and dynamical implications, *Philos. Trans. R. Soc. London A*, *328*, 309–327, 1989.

Hager, B. H., R. W. Clayton, M. A. Richards, R. P. Comer, and A. M. Dziewonski, Lower mantle heterogeneity, dynamic topography, and the geoid, *Nature*, *313*, 541–545, 1985.

Hales, A. L., and H. A. Doyle, *P* and *S* travel time anomalies and their interpretation, *Geophys. J. R. Astron. Soc.*, *13*, 403–415, 1967.

Hales, A. L., and J. L. Roberts, The travel times of *S* and *SKS*, *Bull. Seismol. Soc. Am.*, *60*, 461–489, 1970.

Hara, T., S. Tsuboi, and R. J. Geller, Inversion for laterally heterogeneous upper mantle *S*-wave velocity structure

using iterative waveform inversion, *Geophys. J. Int.*, *115*, 667–698, 1993.

Henson, I. H., and F. A. Dahlen, Asymptotic normal modes of a laterally heterogeneous Earth, 2, Further results, *J. Geophys. Res.*, *91*, 12,467–12,481, 1986.

Herrin, E., Introduction to '1968 Seismological Tables for *P*-phases', *Bull. Seismol. Soc. Am.*, *58*, 1193–1195, 1968.

Inoue, H., Y. Fukao, K. Tanabe, and Y. Ogata, Whole mantle *P*-wave travel time tomography, *Phys. Earth Planet. Inter.*, *59*, 294–328, 1990.

Jarvis, G. T., and W. R. Peltier, Lateral heterogeneity in the convecting mantle, *J. Geophys. Res.*, *91*, 435–451, 1986.

Jeffreys, H., and K. E. Bullen, *Seismological Tables*, British Association for the Advancement of Science, London, 1940.

Jordan, T. H., A procedure for estimating lateral variations from low-frequency eigenspectra data, *Geophys. J. R. Astron. Soc.*, *52*, 441–455, 1978.

Jordan, T. H., A. L. Lerner-Lam, and K. C. Creager, Seismic imaging of boundary layers and deep mantle convection, in *Mantle Convection: Plate Tectonics and Global Dynamics*, edited by W. R. Peltier, pp. 98–201, Gordon and Breach, New York, 1989.

Jordan, T. H., P. Puster, G. A. Glatzmaier, and P. J. Tackley, Comparisons between seismic Earth structures and mantle flow models based on radial correlation functions, *Science*, *261*, 1427–1431, 1993.

Kennett, B. L. N., and E. R. Engdahl, Travel times for global earthquake location and phase identification, *Geophys. J. Int.*, *105*, 429–465, 1993.

Laske, G., and G. Masters, Polarization measurements of long period surface waves and global phase-velocity maps (abstract), *Eos Trans. AGU*, *74*(43), Fall Meeting suppl., 438, 1993.

Lavely, E. M., and M. H. Ritzwoller, The effect of global-scale, steady-state convection on helioseismic frequencies and line-widths, *Astrophys. J.*, *403*, 810–832, 1993.

Lavely, E. M., A. Rodgers, and M. H. Ritzwoller, Can the differential sensitivity of body wave, mantle wave, and normal mode data resolve the trade-off between transition zone structure and boundary topography?, *Phys. Earth Planet. Inter.*, *86*, 117–146, 1994.

Lay, T., and H. Kanamori, Geometric effects of global lateral heterogeneity on long-period surface wave propagation, *J. Geophys. Res.*, *90*, 605–621, 1985.

Leveque, J., and M. Cara, Long-period Love wave overtone data in North America and the Pacific Ocean: New evidence for upper mantle anisotropy, *Phys. Earth Planet. Inter.*, *33*, 164–179, 1983.

Leveque, J., and M. Cara, Inversion of multimode surface wave data: Evidence for sublithospheric anisotropy, *Geophys. J. Int.*, *83*, 753–773, 1985.

Levshin, A. L., L. I. Ratnikova, and J. Berger, Peculiarities of surface wave propagation across the central Eurasia, *Bull. Seismol. Soc. Am.*, *82*, 2464–2493, 1992.

Levshin, A. L., M. H. Ritzwoller, and L. I. Ratnikova, Long-period surface wave polarization anomalies observed at Kislovodsk and Obninsk, Russia, *Geophys. J. Int.*, *117*, 577–590, 1994.

Li, X. D., and T. Tanimoto, Waveforms of long-period body waves in a slightly aspherical Earth model, *Geophys. J. Int.*, *112*, 92–102, 1993.

Li, X.-D., D. Giardini, and J. H. Woodhouse, Large-scale three-dimensional even-degree structure of the Earth from splitting of long-period normal modes, *J. Geophys. Res.*, *91*, 551–577, 1991a.

Li, X. D., D. Giardini, and J. H. Woodhouse, The relative amplitudes of mantle heterogeneity in *P* velocity, *S* velocity, and density from free-oscillation data, *Geophys. J. Int.*, *105*, 649–657, 1991b.

Lognonne, P., Normal modes and seismograms in an anelastic rotating Earth, *J. Geophys. Res.*, *96*, 20,309–29,31 1991.

Lognonne, P., and B. Romanowicz, Fully coupled Earth's vibrations: The spectral method, *Geophys. J. Int.*, *102*, 365–395, 1990.

Masters, G., Seismic modelling of the Earth's large-scale three-dimensional structure, *Philos. Trans. R. Soc. London A*, *328*, 329–349, 1989.

Masters, G., and F. Gilbert, Attenuation in the Earth at low frequencies, *Philos. Trans. R. Soc. London A*, *308*, 479–522, 1983.

Masters, G., and M. H. Ritzwoller, Low frequency seismology and three dimensional structure: Observational aspects, in *Mathematical Geophysics*, edited by N. J. Vlaar, G. Nolet, M. J. R. Wortel, and S. A. P. L. Cloetingh, pp. 1–30, D. Reidel, Norwell, Mass., 1988.

Masters, G., T. H. Jordan, P. G. Silver, and F. Gilbert, Aspherical Earth structure from fundamental spheroidal mode data, *Nature*, *298*, 609–613, 1982.

Masters, G., J. Park, and F. Gilbert, Observations of coupled spheroidal and toroidal modes, *J. Geophys. Res.*, *88*, 10,285–10,298, 1983.

Masters, G., H. Bolton, and P. Shearer, Large-scale 3-dimensional structure of the mantle (abstract), *Eos Trans. AGU*, *73*(43), Fall Meeting suppl., 201, 1992.

Montagner, J.-P., Can seismology tell us anything about convection in the mantle?, *Rev. Geophys.*, *32*, 115–138, 1994.

Montagner, J.-P., and T. Tanimoto, Global anisotropy in the upper mantle inferred from the regionalization of phase velocities, *J. Geophys. Res.*, *95*, 4,797–4,819, 1990.

Montagner, J.-P., and T. Tanimoto, Global upper mantle tomography of seismic velocities and anisotropics, *J. Geophys. Res.*, *96*, 20,337–20,351, 1991.

Morelli, A., and A. M. Dziewonski, Topography of the core-mantle boundary and lateral homogeneity of the liquid core, *Nature*, *325*, 678–683, 1987.

Morelli, A., A. M. Dziewonski, and J. H. Woodhouse, Anisotropy of the inner core inferred from *PKIKP* travel times, *Geophys. Res. Lett.*, *13*, 1545–1548, 1986.

Nakanishi, I., and D. L. Anderson, Worldwide distribution of group velocity of mantle Rayleigh waves as determined by spherical harmonic inversion, *Bull. Seismol. Soc. Am.*, *72*, 1185–1194, 1982.

Nakanishi, I., and D. L. Anderson, Measurement of mantle wave velocities and inversion for lateral heterogeneity and anisotropy, I, Analysis of great circle phase velocities, *J. Geophys. Res.*, *88*, 10,267–10,283, 1983.

Nakanishi, I., and D. L. Anderson, Measurement of mantle wave velocities and inversion for lateral heterogeneity and anisotropy, II, Analysis by the single station method, *Geophys. J. R. Astron. Soc.*, *78*, 573–618, 1984.

Nataf, H.-C., I. Nakanishi, and D. L. Anderson, Anisotropy and shear velocity heterogeneities in the upper mantle, *Geophys. Res. Lett.*, *11*, 109–112, 1984.

Nataf, H.-C., I. Nakanishi, and D. L. Anderson, Measurement of mantle wave velocities and inversion for lateral heterogeneity and anisotropy, III, Inversion, *J. Geophys. Res.*, *91*, 7261–7307, 1986.

Neele, F., and R. Snieder, Topography of the 400 km discontinuity from observations of long-period P_{40} phases, *Geophys. J. Int.*, *109*, 670–682, 1992.

Nishimura, C., and D. Forsyth, The anisotropic structure of the upper mantle in the Pacific, *Geophys. J. R. Astron. Soc.*, *96*, 203–229, 1989.

Olson, P., P. G. Silver, and R. W. Carlson, The large-scale

structure of convection in the Earth's mantle, *Nature*, *344*, 209–215, 1990.

ark, J., Asymptotic coupled-mode expressions for multiplet amplitude anomalies and frequency shifts on an aspherical Earth, *Geophys. J. R. Astron. Soc.*, *90*, 129–169, 1987.

Park, J., Roughness constraints on surface wave tomography, *Geophys. Res. Lett.*, *16*, 1329–1332, 1989.

Park, J., and F. Gilbert, Coupled free oscillations of an aspherical, dissipative, rotating Earth: Galerkin theory, *J. Geophys. Res.*, *91*, 7241–7260, 1986.

Park, J., and Y. Yu, Anisotropy and coupled free oscillations: Simplified models and surface wave observations, *Geophys. J. Int.*, *110*, 401–420, 1992.

Peltier, W. R., and L. P. Solheim, Mantle phase transitions and layered chaotic convection, *Geophys. Res. Lett.*, *19*, 321–324, 1992.

Pollitz, F. F., Propagation of surface waves on a laterally heterogeneous Earth: Asymptotic solution of the two-dimensional wave equation, *Geophys. J. Int.*, *111*, 67–78, 1992.

Pollitz, F. F., and C. G. Hennet, Analysis of Rayleigh wave refraction from three-component seismic spectra, *Geophys. J. Int.*, *113*, 629–650, 1993.

Pulliam, R. J., D. W. Vasco, and L. R. Johnson, Tomographic inversions for mantle *P* wave velocity structure based on the minimization of l^2 and l^1 norms of International Seismological Centre travel time residuals, *J. Geophys. Res.*, *98*, 699–734, 1993.

Randall, M. J., A revised travel-time table for *S*, *Geophys. J. R. Astron. Soc.*, *22*, 229–234, 1971.

Resovsky, J. S., and M. H. Ritzwoller, The long-period seismic effects of long-wavelength elastic and anelastic models, *Geophys. J. Int.*, *117*, 365–393, 1994.

Revenaugh, J., and T. H. Jordan, A study of mantle layering beneath the western Pacific, *J. Geophys. Res.*, *94*, 5787–5813, 1989.

Revenaugh, J., and T. H. Jordan, Mantle layering from *ScS* reverberations, 2, The Transition Zone, *J. Geophys. Res.*, *96*, 19,763–19,780, 1991a.

Revenaugh, J., and T. H. Jordan, Mantle layering from *ScS* reverberations, 3, The upper mantle, *J. Geophys. Res.*, *96*, 19,781–19,780, 1991b.

Ricard, Y., M. Richards, C. Lithgow-Bertelloni, and Y. Le Stunff, A geodynamic model of mantle density heterogeneity, *J. Geophys. Res.*, *98*, 21,895–21,909, 1993.

Ritzwoller, M. H., and E. M. Lavely, Long period surface waves and mantle boundary undulations, *Geophys. J. Int.*, *116*, 205–216, 1994.

Ritzwoller, M. H., and J. Wahr, Geodynamically consistent seismic inversion for mantle structure and internal boundary topography (abstract), *Eos Trans. AGU*, *75*(44), Fall Meeting suppl., 663, 1994.

Ritzwoller, M., G. Masters, and F. Gilbert, Observations of anomalous splitting and their interpretation in terms of aspherical structure, *J. Geophys. Res.*, *91*, 10,203–10,228, 1986.

Ritzwoller, M. H., G. Masters, and F. Gilbert, Constraining aspherical structure with low harmonic degree interaction coefficients: Application to uncoupled multiplets, *J. Geophys. Res.*, *93*, 6269–6396, 1988.

Rodgers, A., and J. Wahr, Inference of core-mantle boundary topography from ISC *PcP* and *PKP* travel times, *Geophys. J. Int.*, *115*, 991–1011, 1993.

odgers, A., and J. Wahr, The trade-off between volumetric and topographic structure for seismic travel times: 660-km topography and mantle structure, *Geophys. J. Int.*, *117*, 19–32, 1994.

Romanowicz, B., Multiplet-multiplet coupling due to lateral heterogeneity: Asymptotic effects on the amplitude and frequency of the Earth's normal modes, *Geophys. J. R. Astron. Soc.*, *90*, 75–100, 1987.

Romanowicz, B. A., The upper mantle degree 2: Constraints and inferences from global mantle wave attenuation measurements, *J. Geophys. Res.*, *95*, 11,051–11,071, 1990.

Romanowicz, B. A., Seismic tomography of the Earth's mantle, *Annu. Rev. Earth Planet. Sci.*, *19*, 77–79, 1991.

Romanowicz, B. A., and M. Cara, Reconsideration of the relations between *S* and *P* station anomalies in North America, *Geophys. Res. Lett.*, *7*, 417–420, 1980.

Romanowicz, B., and G. Roult, First-order asymptotics for the eigenfrequencies of the Earth and application to the retrieval of large-scale lateral variations of structure, *Geophys. J. R. Astron. Soc.*, *87*, 209–239, 1986.

Roult, G., B. Romanowicz, and J. P. Montagner, 3D upper mantle shear velocity and attenuation from fundamental mode free oscillation data, *Geophys. J. R. Astron. Soc.*, *101*, 61–80, 1990.

Shearer, P. M., Constraints on upper mantle discontinuities from observations of long-period reflected and converted phases, *J. Geophys. Res.*, *96*, 18,147–18,182, 1991a.

Shearer, P. M., Imaging global body wave phases by stacking long-period seismograms, *J. Geophys. Res.*, *96*, 20,353–20,364, 1991b.

Shearer, P. M., Global mapping of upper mantle reflectors from long-period SS precursors, *Geophys. J. Int.*, *115*, 878–904, 1993.

Shearer, P. M., and T. G. Masters, Global mapping of topography on the 660-km discontinuity, *Nature*, *355*, 791–796, 1992.

Silver, P. G., R. W. Carlson, and P. Olson, Deep slabs, geochemical heterogeneity, and the large-scale structure of mantle convection: Investigation of an enduring paradox, *Annu. Rev. Earth Planet. Sci.*, *16*, 477–541, 1988.

Smith, M. F., and G. Masters, Aspherical structure constraints from free oscillation frequency and attenuation measurements, *J. Geophys. Res.*, *94*, 1953–1976, 1989a.

Smith, M. F., and G. Masters, The effect of Coriolis coupling of free oscillation multiplets on the determination of aspherical Earth structure, *Geophys. Res. Lett.*, *16*, 263–266, 1989b.

Snieder, R., Large-scale waveform inversions of surface waves for lateral heterogeneity, 2, Application to surface waves in Europe and the Mediterranean, *J. Geophys. Res.*, *93*, 12,067–12,080, 1988.

Snieder, R., and G. Nolet, Linearized scattering of surface waves on a spherical Earth, *J. Geophys.*, *61*, 55–63, 1987.

Snieder, R., and B. Romanowicz, A new formalism for the effect of lateral heterogeneity on normal modes and surface waves, I, Isotropic perturbations, perturbations of interfaces and gravitational perturbations, *Geophys. J. R. Astron. Soc.*, *92*, 207–221, 1988.

Souriau, A., and J. H. Woodhouse, A worldwide comparison of predicted *S*-wave delays from a three-dimensional upper mantle model with *P*-wave station corrections, *Phys. Earth Planet. Inter.*, *39*, 75–88, 1985.

Spakman, W., M. J. R. Wortel, and N. J. Vlaar, The Hellenic subduction zone: A tomographic image and its geodynamic implications, *Geophys. Res. Lett.*, *15*, 60–63, 1988.

Stark, P. B., and N. W. Hengartner, Reproducing Earth's kernel: Uncertainty of the shape of the core-mantle boundary from *PKP* and *PcP* travel-times, *J. Geophys. Res.*, *98*, 1957–1972, 1993.

Stewart, C. A., Thermal convection in the Earth's mantle: Mode coupling induced by temperature dependent viscosity in a three-dimensional shell, *Geophys. Res. Lett.*, *19*, 337–340, 1992.

Su, W., and A. M. Dziewonski, Predominance of long-wavelength heterogeneity in the mantle, *Nature*, *352*, 121–126, 1991.

Su, W., R. L. Woodward, and A. M. Dziewonski, Deep origin of mid-ocean-ridge seismic velocity anomalies, *Nature*, *360*, 149–152, 1992.

Su, W., R. L. Woodward, and A. M. Dziewonski, Degree 12 model of shear velocity heterogeneity in the mantle, *J. Geophys. Res.*, *99*, 6945–6980, 1994.

Tackley, P. J., D. J. Stevenson, G. A. Glatzmaier, and G. Schubert, Effects of an endothermic phase transition at 670 km depth in a spherical model of convection in the Earth's mantle, *Nature*, *361*, 699–704, 1993.

Takeuchi, H., and M. Saito, Seismic surface waves, *Methods Comput. Phys.*, *11*, 217–295, 1972.

Tanimoto, T., Long-wavelength *S*-wave velocity structure throughout the mantle, *Geophys. J. Int.*, *100*, 327–336, 1990a.

Tanimoto, T., Modeling curved surface wave paths: Membrane surface wave synthetics, *Geophys. J. Int.*, *102*, 89–100, 1990b.

Tanimoto, T., Predominance of large-scale heterogeneity and the shift of velocity anomalies between the upper and lower mantle, *J. Phys. Earth*, *38*, 493–509, 1990c.

Tanimoto, T., and D. L. Anderson, Mapping convection in the mantle, *Geophys. Res. Lett.*, *11*, 287–290, 1984.

Tanimoto, T., and D. L. Anderson, Lateral heterogeneity and azimuthal anisotropy of the upper mantle: Love and Rayleigh waves 100–250s, *J. Geophys. Res.*, *90*, 1842–1858, 1985.

Toy, K., Tomographic analysis of ISC travel time data for Earth structure, Ph.D. thesis, Univ. of Calif., San Diego, 1989.

Tromp, J., and F. A. Dahlen, Variational principles for surface wave propagation on a laterally heterogeneous Earth, I, Time-domain JWKB theory, *Geophys. J. Int.*, *109*, 581–598, 1992a.

Tromp, J., and F. A. Dahlen, Variational principles for surface wave propagation on a laterally heterogeneous Earth, II, Frequency-domain JWKB theory, *Geophys. J. Int.*, *109*, 599–619, 1992b.

Um, J., and F. A. Dahlen, Normal mode multiplet coupling along a dispersion branch, *Geophys. J. Int.*, *106*, 11–35, 1991.

Um, J., and F. A. Dahlen, Normal mode multiplet coupling on an aspherical, anelastic Earth, *Geophys. J. Int.*, *111*, 11–31, 1992.

Urhammer, R., *S*-wave travel times for a spherically averaged Earth, *Geophys. J. R. Astron. Soc.*, *55*, 283–309, 1978.

Vasco, D. W., R. J. Pulliam, and L. R. Johnson, Formal inversion of ISC arrival times for mantle *P*-wave structure, *Geophys. J. Int.*, *113*, 586–606, 1993.

Vidale, J. E., and H. M. Benz, Upper-mantle seismic discontinuities and the thermal structure of subduction zones, *Nature*, *356*, 678–683, 1992.

Wichens, A. J., and G. G. R. Buchbinder, *S*-wave residuals in Canada, *Bull. Seismol. Soc. Am.*, *70*, 809–822, 1980.

Wicks, C. W., Jr., and M. A. Richards, A detailed map of the 660-km discontinuity beneath the Izu-Bonin subduction zone, *Science*, *261*, 1424–1427, 1993.

Widmer, R., and G. Masters, Observably split multiplets: Data analysis and interpretation in terms of large-scale aspherical structure, *Geophys. J. Int.*, *111*, 559–576, 1992.

Widmer, R., G. Masters, and F. Gilbert, Spherically symmetric attenuation within the Earth from normal mode data, *Geophys. J. Int.*, *104*, 541–553, 1992.

Wong, Y. K., Upper mantle heterogeneity from phase and amplitude data of mantle waves, Ph.D. thesis, Harvard Univ., Cambridge, Mass., 1989.

Woodhouse, J. H., The coupling and attenuation of nearly resonant multiplets in the Earth's free oscillation spectrum, *Geophys. J. R. Astron. Soc.*, *61*, 261–283, 1980.

Woodhouse, J. H., and F. A. Dahlen, The effect of a general aspherical perturbation on the free oscillations of the Earth, *Geophys. J. R. Astron. Soc.*, *53*, 335–354, 1978.

Woodhouse, J. H., and A. M. Dziewonski, Mapping the upper mantle: Three-dimensional modelling of Earth structure by inversion of seismic waveforms, *J. Geophys. Res.*, *89*, 5953–5986, 1984.

Woodhouse, J. H., and A. M. Dziewonski, Seismic modelling of the Earth's large-scale three-dimensional structure, *Philos. Trans. R. Soc. London A*, *328*, 291–308, 1989.

Woodhouse, J. H., and T. P. Girnius, Surface waves and free oscillations in a regionalized Earth model, *Geophys. J. R. Astron. Soc.*, *68*, 653–673, 1982.

Woodhouse, J. H., and Y. K. Wong, Amplitude, phase and path anomalies of mantle waves, *Geophys. J. R. Astron. Soc.*, *87*, 753–773, 1986.

Woodhouse, J. H., D. Giardini, and X. D. Li, Evidence for inner core anisotropy from free oscillations, *Geophys. Res. Lett.*, *13*, 1549–1552, 1986.

Woodward, R. L., and G. Masters, Upper mantle structure from long-period differential travel times and free oscillation data, *Geophys. J. Int.*, *109*, 275–293, 1991a.

Woodward, R. L., and G. Masters, Lower-mantle structure from *ScS-S* differential travel times, *Nature*, *352*, 231–233, 1991b.

Wu, F., and A. Levshin, Surface wave tomography of China using surface waves at CDSN, *Phys. Earth Planet. Inter.*, *84*, 59–78, 1994.

Yeganch-Hacri, A., D. J. Weidner, and E. Ito, Elasticity of $MgSiO_3$ in the perovskite structure, *Science*, *243*, 786–789, 1989.

Yu, Y., and J. Park, Upper mantle anisotropy and coupled-mode long-period surface waves, *Geophys. J. Int.*, *114*, 473–489, 1993.

Zhang, Y.-S., and T. Tanimoto, Ridges, hotspots, and their interpretation as observed in seismic velocity maps, *Nature*, *355*, 45–49, 1992.

Zhang, Y.-S., and T. Tanimoto, High-resolution global upper mantle structure and plate tectonics, *J. Geophys. Res.*, *98*, 9793–9823, 1993.

Zhang, Y.-S., T. Tanimoto, and E. Stolper, *S*-wave velocity, basalt chemistry and bathymetry along the Mid-Atlantic Ridge, *Phys. Earth Planet. Inter.*, *84*, 79–93, 1994.

E. M. Lavely and M. H. Ritzwoller, Department of Physics, Campus Box 390, University of Colorado, Boulder, CO 80309-0390. (e-mail: ritzwoller@lemond.colorado.edu)